Angle-resolved photoemission study of $BaFe_2S_3$: possibility of excitonic instability

T. Mizokawa[a], S. Iwasaki[a], K. Yamamoto[a], N. L. Saini[b],
T. Aoyama[c], K. Hashizume[c], K. Ohgushi[c],
M. Arita[d], H. Namatame[d], M. Taniguchi[d,e]

[a] Department of Applied Physics, Waseda University, Shinjuku-ku, Tokyo 169-8555, Japan
[b] Department of Physics, University of Roma "La Sapienza", Piazzale Aldo Moro 2, 00185 Roma, Italy
[c] Department of Physics, Tohoku University, Sendai, Miyagi 980-8578, Japan
[d] HiSOR, Hiroshima University, Higashihiroshima, Hiroshima 739-0046, Japan
[e] Graduate School of Science, Hiroshima University, Higashihiroshima, Hiroshima 739-8526, Japan

Although parent compounds of the cuprate superconductors and the Fe-based superconductors are commonly antiferromagnetic, those of the Fe-based superconductors are usually metallic whereas those of the cuprates are Mott insulators. However, the antiferromagnetic insulating phase of $K_xFe_{2-y}Se_2$ has been identified as $K_2Fe_4Se_5$ with Fe vacancy order and is considered as a Mott insulator due to bandwidth reduction by the Fe vacancy [1-3]. The charge-transfer energy from Se $4p$ to Fe $3d$ is estimated to be ~ 2 eV for $K_2Fe_4Se_5$ which is smaller than the Fe $3d$-$3d$ repulsive Coulomb interaction ~ 3.5 eV. [4] Therefore, the insulating $K_2Fe_4Se_5$ phase with high-spin Fe^{2+} can be regarded as a Mott insulating state of charge-transfer type similar to the parent materials of cuprate superconductors. In this context, it is very interesting and important to study antiferromagnetic insulating phases of Fe chalcogenides in a systematic way. Recently, another insulating Fe chalcogenide $BaFe_2S_3$ has been attracting great interest especially due to the discovery of pressure-induced superconductivity in $BaFe_2S_3$ [5,6]. The crystal structure of $BaFe_2S_3$ is characterized by the two-leg ladder structure of Fe sites. The Fe spins are antiferromagnetically ordered along the ladder [7,8] In order to understand the nature of the antiferromagnetic insulating state, we have performed angle-resolved photoemission spectroscopy on $BaFe_2S_3$ at BL-9A, HiSOR.

Figure 1 shows the ARPES data along the ladder direction. Here, k_x is the wave number along the ladder, and k_y is the wave number perpendicular to it. The intense and weak spectral features are observed around -0.8 eV and -0.2 eV, respectively. If the ground state is a Mott insulating state with high spin Fe^{2+} ($e_{g\uparrow}^2 t_{2g\uparrow}^3 e_{g\downarrow}^1$), the first and second ionization states are obtained by excitations of the $e_{g\downarrow}$ electron and of the $t_{2g\uparrow}$ electron respectively. In the Mott insulator picture, the flat and intense band around -0.8 eV corresponds to the removal of the Fe $3d$ $t_{2g\uparrow}$ electron that should be heavily mixed with the S $3p$ orbitals. On the other hand, the weak band around -0.2 eV can be assigned to the removal of the Fe $3d$ $e_{g\downarrow}$ electron that is less hybridized with the S $3p$ orbitals than t_{2g}. In the ARPES result, the $t_{2g\uparrow}$ band around -0.8 eV depends on both k_x and k_y. This would be consistent with the hybridization between the neighboring ladders due to the inter-ladder S $3p$-S $3p$ transfer integrals. In contrast, the $e_{g\downarrow}$ band around -0.2 eV hardly depends on k_y, consistent with the expectation that the inter-ladder Fe $3d$-Fe $3d$ transfer integrals are very small.

The $e_{g\downarrow}$ band around -0.2 eV exhibits some dispersion along k_x, and the band width may represent the strength of superexchange interaction J along the ladder just like the band dispersion in the parent compounds of cuprate superconductors. The difference between the present system and the cuprate is Hund coupling between t_{2g} and e_g spins. In future, the ARPES result should be analyzed using a realistic multi-band Hubbard model considering the Hund coupling in future. Another possible interpretation is that the spin triplet excitons between the e_g electron and t_{2g} hole are formed and condensate at the wave number of $\pi/2a$, where $2a$ is the periodicity of the Fe $3d$ spin in the antiferromagnetic state. Such excitonic picture (which is usually valid for semimetals or semiconductors) would be more appropriate than the Mott insulator picture.
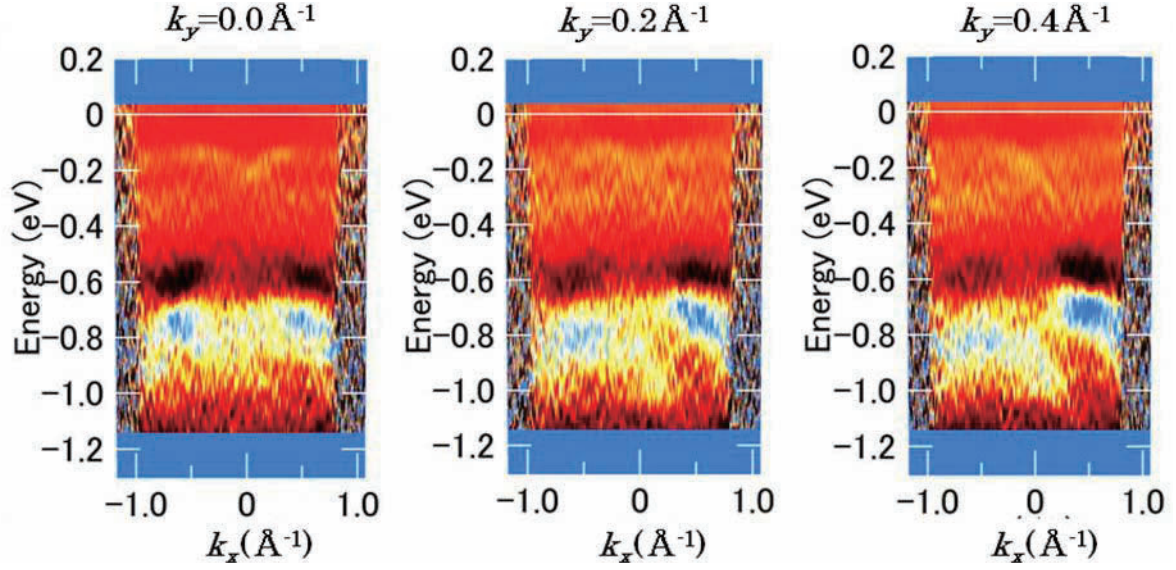
FIGURE 1. Band dispersion along the ladder direction taken at 80 K (antiferromagnetic state). The flat band around -0.8 eV corresponds to the lower Hubbard band. k_x and k_y represent the wave numbers parallel and perpendicular to the ladder, respectively.

REFERENCES

1. J. Guo, S. Jin, G. Wang, S. Wang, K. Zhu, T. Zhou, M. He, and X. Chen, Phys. Rev. B **82**, 180520 (2010).
2. Z. Shermadini, A. Krzton-Maziopa, M. Bendele, R. Khasanov, H. Luetkens, K. Conder, E. Pomjakushina, S. Weyeneth, V. Pomjakushin, O. Bossen, and A. Amato, Phys. Rev. Lett. **106**, 117602 (2011).
3. F. Ye, S. Chi, W. Bao, X. F. Wang, J. J. Ying, X. H. Chen, H. D. Wang, C. H. Dong, and M. Fang, Phys. Rev. Lett. **107**, 137003 (2011).
4. M. Oiwake, D. Ootsuki, T. Noji, T. Hatakeda, Y. Koike, M. Horio, A. Fujimori, N. L. Saini, and T. Mizokawa, Phys. Rev. B **88**, 224517 (2013).
5. H. Takahashi, A. Sugimoto, Y. Nambu, T. Yamauchi, Y. Hirata, T. Kawakami, M. Avdeev, K. Matsubayashi, F. Du, C. Kawashima, H. Soeda, S. Nakano, Y. Uwatoko, Y. Ueda, T. J. Sato, and K. Ohgushi, Nat. Mater. **14**, 1008 (2015).
6. T. Yamauchi, Y. Hirata, Y. Ueda, and K. Ohgushi, Phys. Rev. Lett. **115**, 246402 (2015).
7. Y. Nambu, K. Ohgushi, S. Suzuki, F. Du, M. Avdeev, Y. Uwatoko, K. Munakata, H. Fukazawa, S. Chi, Y. Ueda, and T. J. Sato, Phys. Rev. B **85**, 064413(2012).
8. F. Du, K. Ohgushi, Y. Nambu, T. Kawakami, M. Avdeev, Y. Hirata, Y. Watanabe, T. J. Sato, and Y. Ueda, Phys. Rev. B **85**, 214436 (2012).

Electronic structure of K-doped iron-selenide superconductor studied by polarization-dependent angle-resolved photoemission spectroscopy

M. Sunagawa[a], K. Terashima[a], T. Hamada[a], H. Fujiwara[a], M. Tanaka[b],
H. Takeya[b], Y. Takano[b], M. Arita[c], K. Shimada[c], H. Namatame[c], M. Taniguchi[c],
K. Suzuki[d], H. Usui[e], K. Kuroki[e], T. Wakita[a], Y. Muraoka[a], T. Yokoya[a]

[a]*The Graduate School of Natural Science and Technology, Okayama University, Japan*

[b]*MANA, National Institute for Material Science, Japan*

[c]*Hiroshima Synchrotron Radiation Center, Hiroshima University, Japan*

[d]*Research Organization of Science and Technology, Ritsumeikan University, Japan*

[e]*Department of Physics, Osaka University, Japan.*

Keywords: ARPES, iron-based superconductor

For describing the high-T_c superconductivity in iron-based superconductors, the Fermi-surface-nesting scenario has been proposed, in which the nesting between the hole- and electron-like FSs induces spin fluctuation-mediated superconductivity [1,2]. However, absence of hole-like FS in $K_xFe_{2-y}Se_2$ superconductor has been reported by several ARPES studies [3,4], which prohibits the FS nesting scenario. Although the novel theoretical models have been proposed to explain the superconductivity, these models face difficulties to explain the experimental results [5-7], such as the presence of spin-resonance mode [8] and the nodeless superconducting gap structure [3,4]. In order to resolve this issue, revisiting the electronic structure of superconducting AFS is necessary.

$K_xFe_{2-y}Se_2$ also exhibits the phase separation, which induces the unique surface morphology that consists of the minority superconducting phase (~10%) embedded in the majority insulating phase (~90%) [9]. Due to the smaller superconducting region in the sample surface, previous ARPES measurements were possible to elude an intrinsic electronic structure of superconducting phase. Very recently, an improvement of sample preparation allows us to obtain high-quality $K_{0.62}Fe_{1.7}Se_2$ single crystal, which has an increased area of the superconducting phase (~30%) [10]. Thus, there is a possibility that the ARPES measurement of $K_{0.62}Fe_{1.7}Se_2$ will detect an intrinsic electronic structure responsible for the superconductivity. In our study, we performed polarization-dependent ARPES measurements on a high quality single crystal of $K_{0.62}Fe_{1.7}Se_2$ and we succeeded to observe a hole-like band with E_F-approaching around the Γ point, indicating that a hole-like FS exists in $K_xFe_{2-y}Se_2$ [11].

Figures 1(a-f) show ARPES data along #1 in Fig. 1(k) with s-polarized (s-pol) and p-polarized (p-pol) light [for the geometrical measurement configuration, see Fig. 2(k)]. We observed α-ε bands that are found to be consistent with previous ARPES studies [5,6]. In addition, we also observed a faint intensity showing a finite dispersion (ζ) around $k = -0.5$ Å^{-1} in Fig. 2(d). From the second-derivative method in energy and momentum distribution curve (MDC) analysis, we find that the ζ band has a faster hole-like dispersion than the ε band.

In order to elucidate the near-E_F dispersion of the ζ band, we performed further ARPES measurement. Along #5 in Fig. 2(c), a fast hole-like dispersion, corresponding to the ζ band, is seen in the ARPES data. A large constant-energy surface of the ζ band can be seen in the energy contour plot at -40 meV, as indicated with a red broken circle in Fig. 2(c). Comparing the dispersion of the ζ band at #1 and #5 [Fig. 2(f)], we find that the ζ band gradually shifts to a lower-momentum region as the wave vectors move away from the Γ-M line, demonstrating the presence of a hole-like ζ band around Γ. Although the intensity of the ζ band almost vanishes in the energy contour plot at -20 meV, the MDCs of the ARPES plot along #5 [Fig. 2(e)] show a finite energy dispersion of the shoulder structure that reaches -20 meV at $k = +0.26$ Å^{-1}, suggesting that E_F crosses the ζ band. The observation of the hidden hole-like band approaching E_F suggests the presence of a hole-like FS in K_xFe_2-

$_y$Se$_2$. This result indicates that AFS can be categorized in the same group as iron arsenides with both hole- and electron-like FSs present.
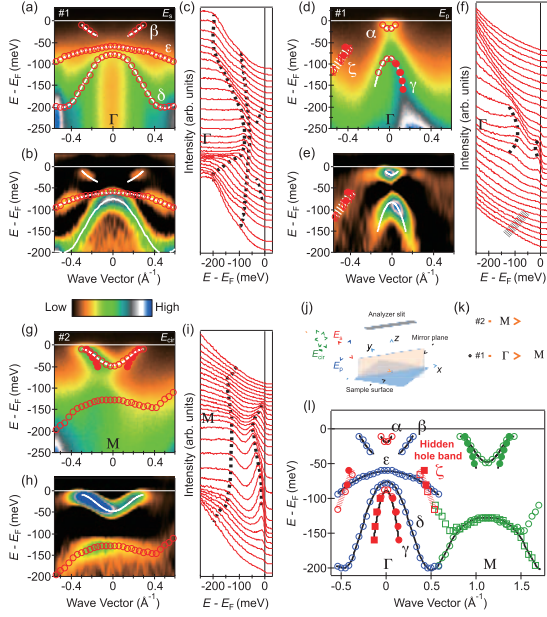

Fig. 2. (a) ARPES intensity plot taken along #1 with s-pol light. (b,c) Second derivatives with respect to energy and the EDCs of (a), respectively. (d-f) Same as (a-c) but taken along #1 with p-pol light. (g-i) Same as (a-c) but taken along #2 with c-pol light. (j) Experimental geometry for ARPES measurements. (k) Two-dimensional BZ (black line) and the measurement directions (orange arrows). (l) Summary of the experimental band structure for K$_{0.62}$Fe$_{1.7}$Se$_2$.
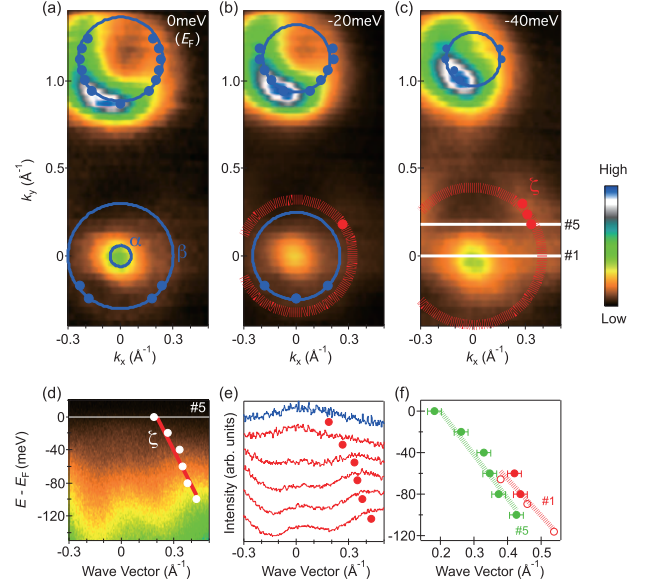

Fig. 3. (a-c) Energy contour intensity plots at E-E_F = 0, -20, and -40 meV, respectively. In (a-c), solid and broken circles indicate the FSs and the constant-energy contours deduced from the MDC peak positions (red and blue dots). (d) ARPES intensity plots taken along #5, respectively, as indicated by the white lines in (c). (e) MDCs of (d) together with the peak position (red circles). (f) Dispersion of the ζ band at #1 (red) and #5 (green).

REFERENCE

[1] I. I. Mazin *et al*., Phys. Rev. Lett. **101**, 057003 (2008).

[2] K. Kuroki *et al*., Phys. Rev. Lett. **101**, 087004 (2008).

[3] M. Xu *et al*., Phys. Rev. B **85**, 220504 (2012).

[4] D. Mou *et al*., Phys. Rev. Lett. **106**, 107001 (2011).

[5] I. I. Mazin, Phys. Rev. B **84**, 02459 (2011).

[6] M. Khodas *et al.*, Phys. Rev. Lett. **108**, 247003 (2012).

[7] A. Kreisel *et al.*, Phys. Rev. B **88**, 094522 (2013).

[8] G. Friemel *et al.,* Phys. Rev. B **85**, 140511 (2012).

[9] A. Ricci *et al.,* Phys. Rev. B **84**, 060511(R) (2011).

[10] M. Tanaka *et al*., http://arxiv.org/abs/1504.04197v1

[11] M. Sunagawa *et al.*, accepted for publication in JPJS

Replica of the Dirac cone in the epitaxial graphene due to the periodic potential of the SiC substrate

Shin-ichiro Tanaka[a]

[a] The institute of Scientific and Industrial Research, Osaka University

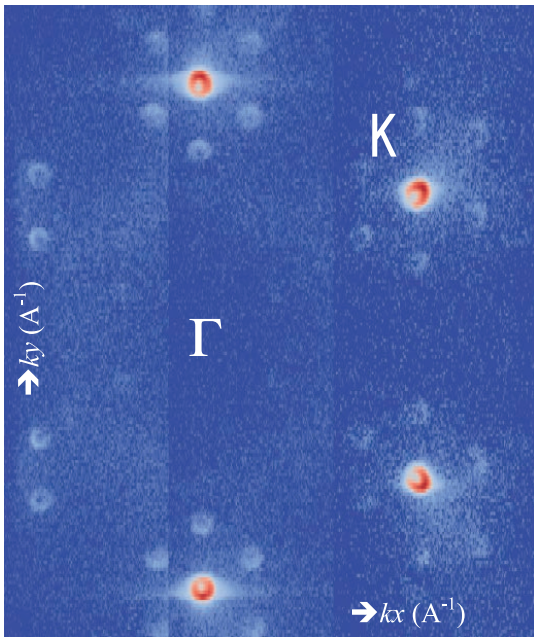**Keywords:** ARPES, graphene, SiC, diffraction, replica

Fig.1 : Intensity map (in logarithmic scale) at the Fermi level obtained by the ARPES measurement for the graphene/SiC. The photon is p-polarized and its energy is 33eV.

Graphene is one of the materials which is attracting most attention from the researchers of the wide area. Its honeycomb structure composed of two equivalent triangular carbon sublattices leads to the formation of the Dirac cone of a linear dispersion. The wavefunction of the Dirac cone is characterized essentially by the term of $\exp(i\theta_q)$, where θ_q (the angle around the K point in the reciprocal lattice space) can be regarded as the phase. Such characteristics oer exciting opportunities for the occurrence of new phenomena and the development of high performance electronic devices. Recently, the perturbation by the superlattice of the substrate on which the graphene is formed has investigated extensively[1]. The cloning of the Dirac cone due to the superperiodicity may open the band gap due to the interaction between the "original" and "replica" bands. In this report, we demonstrate the formation of replicas of the Dirac cone of in graphene due to the periodic potential of the SiC substrate by the use of the resonant angle-resolved photoelectron spectroscopy (ARPES). Surprisingly, the replicas are of the four-fold symmetry in terms of the phase, which is changed from the original six-fold symmetry.

The experiments were carried out at the HiSOR BL-9A, where the high-resolution ARPES spectra can be obtained at the photon energy region from ~6eV to ~50eV. The single-layer graphene formed on the SiC substrate was cleaned by the heating at UHV at 1000K , and measurement was done at 10K. Figure 1 shows the photoelectron intensity distribution map at the Fermi level for graphene/SiC. The photon is p-polarized, and 33eV in energy. The incidence plane is parallel to the Γ-M direction. The intensity is scaled logarithmically, and the faint replicas are clearly resolved surrounding every K point where the "original" Dirac cone is located. These replicas were reported previously [2], and it was concluded that these are not duplications of the Dirac cones in fact. Instead, they are produced by the photoelectron diffraction by the $(6\sqrt{3}\times6\sqrt{3})R30°$ periodicity of the "buffer layer" which is formed between the graphene layer and SiC substrate. The diffraction is considered to occur after the photoelectron emission from the graphene, and no interaction among bands exists. Note that the intensity distribution of the Dirac cone around the K point is a function of θ_q, i.e., $\propto \cos^2(\vartheta_q/2)$, where θ_q is the angle from the K-M direction. Thus, whole system is of the six-fold symmetry. The replicas have the same

intensity distribution to the original cone, suggesting that the phase of the Dirac cone does not change during the scattering. When the s-polarized light is used, the intensity distribution exhibits a completely opposite behavior, i.e., the intensity is propotional to $\sin^2\left(\vartheta_q/2\right)$. On the other hand, when the photon energy is near 11eV, a strong resonant enhancement is observed and the additional Dirac cones appear. Fig. 2 shows the photoelectron intensity map in the k_x-k_y plane at the Fermi level taken at hv=10.8eV. The photon was p-polarized and the incident angle is parallel to the Γ-K direction (the sample is rotated by 30° from Fig.1). The photon energy used is not high enough to emit the Dirac cone at the K-point (the distance from the Γ to K points is 1.7 A^{-1}), and the Dirac cones observed in Fig. 2 must be replicas, which are provided by the superperiodicity. A comparison of positions of these cones in the Brillouin zone to the low energy electron diffraction (LEED) pattern (not shown here) indicates that the diffraction vectors from the original cones at the K-points to the newly observed cones agrees with the diffraction spots corresponding to the the SiC crystal. The lower panel of Fig. 2 shows a schematic model in the reciplocal lattice space, where the large blue balls indicates the original K points (Γ-point is located near the center of the schetch), the blue balls in the medium size denotes the positions of the dupulicated cones transferred by the vector due to the SiC lattice indicated as an arrow, and the small red balls are transferred K-points by mulitiple diffractions including the SiC-substrate and the $(6\sqrt{3}\times6\sqrt{3})R30°$ periodicity. The agreement between the faint replicas and the red balls are not good, and another diffraction vector would be necessary to take into account for a perfect interpretation.

One may argue that these are due to the diffraction of the electron after the photoemission at the SiC substrate, similarly to the $(6\sqrt{3}\times6\sqrt{3})R30°$ replicas observed in Fig.1. However, the intensity distributions of the replicas contradict this interpretation. They form the four-fold symmetric intensity distribution around the Γ-
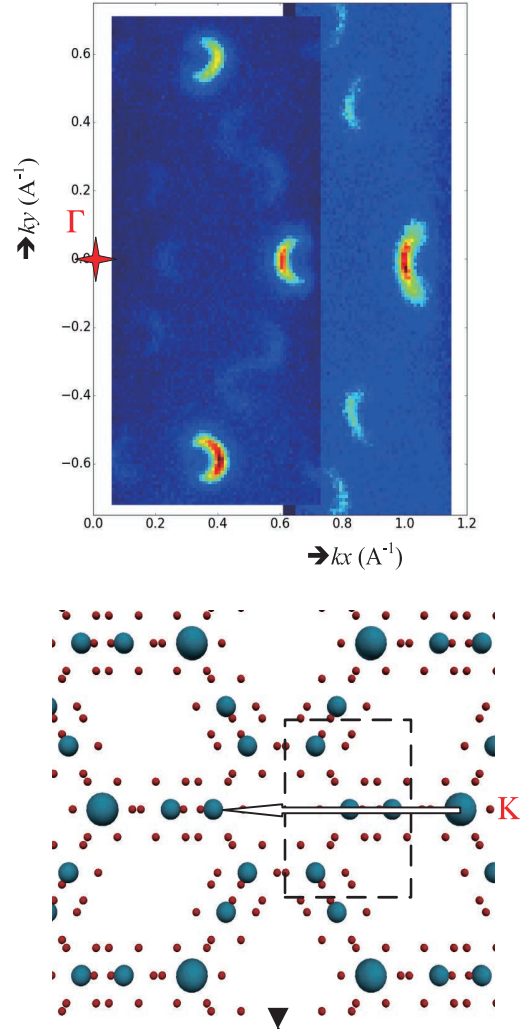

Fig.2 : Upper panel: Intensity map (in linear scale) at the Fermi edge obtained by the ARPES measurement for the graphene/SiC. The photon is p-polarized and its energy is 10.8eV.The sample azimuth is rotated by 30° with respect to Fig.1.
Lower panel: Schematic model in the reciprocal lattice. The arrow shows one of the diffraction vector. The dotted rectangular shows the area of the ARPES map.

point, which completely disagree to the six-fold symmetry of the original Dirac cones. This indicates that the phases of each replicas are shifted differently from the original Dirac cones. The diffraction after the photoemission process cannot explain at all this change in symmetry. Thus, it is considered that the formation of the replicas and the phase-shift of the Dirac cone is ascribed to the perturbation of the wavefuntions of graphene due to the superperiodicity of the SiC substrate.

Another important property of the replicas is their resonant behavior with respect to the photon energy. The photon-energy dependence of the intensity of the replica clearly showed that the replica is observed only when a specific final state is chosen for the photoelectron excitation. Thus, we have to account a possibility that the interaction of the wavefunction of the graphene and the superperiodic potential of the SiC substrate may not occur at the valence bands, but at the unoccupied bands. More work is needed to clarify the physical origin of the phase shift in the replica of the Dirac cone.

[1] L.A.Ponomarenko et al., Nature. 497, 594 (2013); I. Pletikosic et al., Phys. Rev. Lett. 102, 056808 (2009)
[2] A. Bostwick et al., Nature Phys. 3, 36 (2007).

Resonance photoelectron spectroscopy of strongly spin-orbit coupled surface states

Hendrik Bentmann, Henriette Maaß, Christoph Seibel, Friedrich Reinert

ªExperimentelle Physik 7, University Würzburg, Am Hubland, 97074 Würzburg, Germany

Keywords: Spin-orbit coupling, ARPES

Strong spin-orbit coupling lifts the spin degeneracy of electronic surface state bands in heavy-element materials by virtue of the Rashba effect. Moreover spin-orbit coupling locks the spin direction to the electron wave vector $k_{\parallel}$, giving rise to characteristic spin textures in momentum space. This spin-momentum locking results in peculiar scattering properties in electron transport which might proof useful in the context of applications in spintronics or quantum computation [1]. Here we studied the spin-orbit split surface states of Bi_2Te_3 and Pb/Ag(111) by systematic photon-energy- and polarization-dependent ARPES experiments, using s- and p-polarized light between photon energies of ca. hv = 14 eV to 32 eV.

Using p-polarized light we found strong photon-energy-dependent variations in the relative intensities of the bands in Pb/Ag(111) between energies of ca. hv = 22-26 eV, similar to our previous findings for the isostructural compound Bi/Ag(111). We therefore can conclude that these matrix-element-effects are likely related to the final state and to the unoccupied band structure of Ag(111). With s-polarized light only weaker dependences on photon energy are found in the intensities. Instead the matrix elements across the $k_{\parallel}$ momentum plane appear to be reasonably well described by considering the orbital composition in the initial states [2]. Exemplary data sets are shown in Figure 1 for hv = 24 eV. For the case of Bi_2Te_3 we have also observed rather strong variations of the photoemission intensities. Depending on photon energy and polarization the intensity across the Fermi surface shows strong threefold modulations, in accordance with the crystal symmetry, or displays a more isotropic distribution. The experimental results shall now be compared to relativistic one-step photoemission calculations performed by our collaborators [3], in order to identify the contributions of initial and final states to the observed photoemission intensity. By this we hope to gain a better understanding of the photoemission matrix element of spin-orbit coupled states, which is desirable in order to reliably address their spin and orbital character by photoemission spectroscopy in a wide range of materials.

REFERENCES

1. M. Z. Hasan and C. L. Kane, Rev. Mod. Phys. **82**, 3045 (2010).
2. L. El-Kareh *et al.*, *New J. Phys.* **16** 045017 (2014).
2. Christoph Seibel, Hendrik Bentmann, Jürgen Braun, Jan Minár, Henriette Maaß, Kazuyuki Sakamoto, Masashi Arita, Kenya Shimada, Hubert Ebert, and Friedrich Reinert, Phys. Rev. Lett. **114**, 066802 (2015).
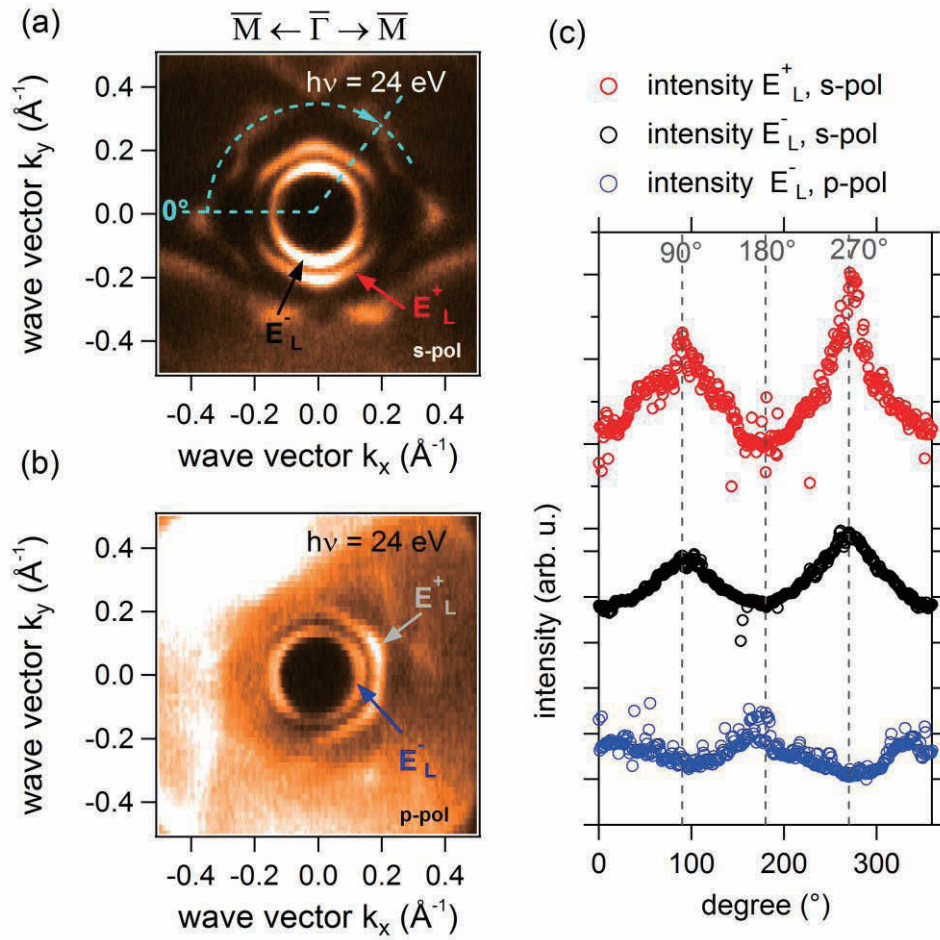
Figure 1: ARPES Fermi-surface data sets for Pb/Ag(111) obtained with hv = 24 eV and s- and p-polarized light in a) and b), respectively. In c) we show an evaluation of the photoemission intensity of the individual bands along the Fermi surface contours. We find that depending on light polarization the intensity distribution strongly differ whoich is attributed to the particular orbital composition of the states [2].

Superconducting gap and low-energy kink structure in the high-T_c cuprates La$_{2-x}$Sr$_x$CuO$_4$

D. Shimonaka[a], D. Ootsuki[a], D. Shibata[a], A. Fujimori[b], M. Arita[c], H. Namatame[c], M. Taniguchi[c], S. Komiya[d], Y. Ando[e], T. Yoshida[a]

[a]*Graduate School of Human and Environmental Studies, Kyoto University, Kyoto 606-8501, Japan*
[b]*Department of Physics, University of Tokyo, Tokyo 113-0033, Japan*
[c]*Hiroshima Synchrotron Radiation Center, Hiroshima University, Higashi-Hiroshima, 739-0046, Japan*
[d]*Central Research Institute of Electric Power Industry, Yokosuka, Kanagawa 240-0196, Japan*
[e]*Institute of Physics II, University of Cologne, Köln 50937, Germany*

The origin of the pseudogap in the high-T_c cuprates has been a controversial issue. There are roughly two interpretation of it as follows, that is, "one gap" or "two gap" scenario. In the former scenario, the pseudogap is a precursor to the superconductivity [1]. In the latter scenario, the pseudogap has a different origin from the superconducting gap and it coexists with the superconductivity in the antinodal region. In angle-resolved photoemission spectroscopy (ARPES) studies, it has been shown that the anisotropy of the energy gap does not follow a simple d-wave form [2,3]. Previous ARPES studies of the optimally doped La$_{2-x}$Sr$_x$CuO$_4$ (LSCO) have suggested anomalous enhancement of the energy gap as well as a suppression of the superconducting peak in the anti-nodal region [4,5]. On the other hand, a clear superconducting peak with a small energy kink ~20 meV has been observed in the off-nodal region [4,6]. Thus, to obtain further information of the superconducting states, we performed high-resolution ARPES measurements of optimally doped LSCO (x = 0.15) (T_c= 38K) in the off-nodal region. The measurements were carried out at HiSOR BL-9A. The excitation photon energy and the total energy resolution were set at $h\nu$ = 21 eV and ΔE = 10 meV, respectively.

Figure 1 shows ARPES spectra of LSCO (x = 0.15) taken at T = 7 K (< T_c) and 40 K (>T_c) in the off-nodal region. One can clearly see a low-energy kink ~25 meV in the energy dispersion below T_c, while the energy dispersion above T_c almost linearly crosses E_F [Fig. 1(c)]. Figure 2 shows energy distribution curves (EDCs) at k_F and symmetrized spectra at each temperature. A superconducting coherence peak is clearly observed below T_c, and the gap magnitude is estimated to be ~ 9 meV, while the gap is closed in the normal state. As indicated by arrows in Fig. 2, there is a characteristic energy scale ~ 70 meV corresponding to the nodal kink below and above T_c. Furthermore, the coherence peak in the superconducting state evolves within 20-30 meV from E_F corresponding to the low-energy kink in Fig. 1 (c). Such a low-energy electron-boson interaction may be related to the high-T_c superconductivity in LSCO. While the bosonic mode has been interpreted as a magnetic resonance [6], further studies are necessary to reveal the origin of the bosonic mode.
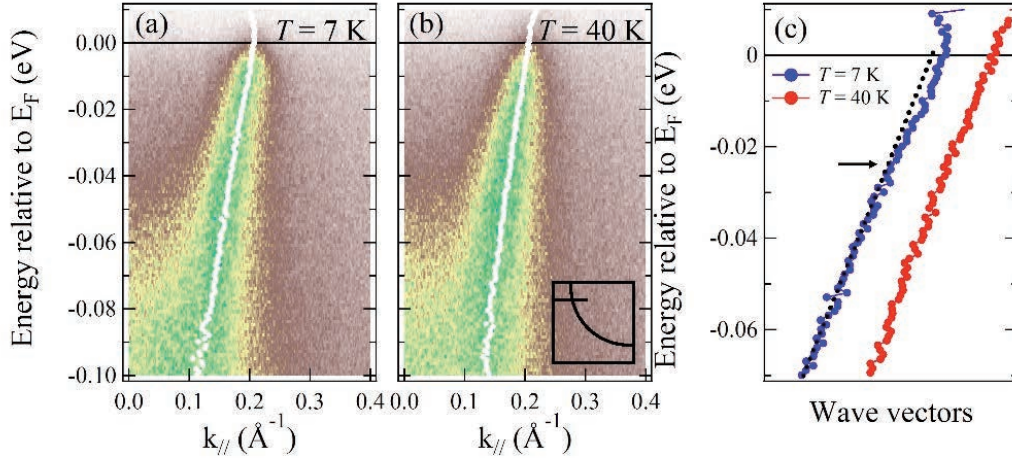
Figure 1. (a)(b): ARPES intensity plots of the off-nodal region in the superconducting state ($T=$ 7 K) [panel (a)] and in the normal state ($T=$ 40 K) [panel (b)]. White dots indicate energy dispersions determined by the peaks of MDC's. (c): Comparison of the energy dispersions for each state. Black arrow indicates the kink structure around 20-30 meV below E_F and dotted line is a guide to eyes.
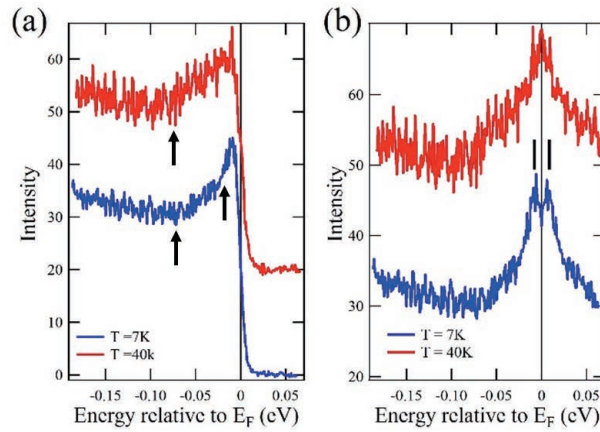

Figure 2. (a): Energy distribution curves (EDCs) at k_F taken at 7 K and 40 K. (b): Symmetrized EDCs.

REFERENCES

1.   J. Meng *et al.*, Phys. Rev. Lett. **103**, 037004 (2009).
2.   J.-H. Ma *et al.*, Phys. Rev. Lett. **101**, 207002 (2008).
3.   T. Yoshida *et al.,* PhysRevLett.**103**, 037004 (2009).
4.   K. Terashima *et al.,* Phys. Rev. Lett. **99**, 017003 (2007).
5.   T. Yoshida *et al.*, Phys. Rev. B **93**, 014513 (2016).
6.   T. Sato *et al.*, J. Phys. Soc. Jpn. **76**, 103707 (2007).

Extremely correlated Hund metal
emerging on the topmost layer of Sr₂RuO₄

T. Kondo,[a] M. Ochi,[b, c] M. Nakayama,[a] S. Akebi,[a] K. Kuroda,[a] H. Taniguchi,[d]
M. Arita,[e] S. Sakai,[b, c] H. Namatame,[e] M. Taniguchi,[e, f] Y. Maeno,[d] R. Arita,[b, c]
and S. Shin [a]

[a] ISSP, University of Tokyo, Kashiwa, Chiba 277-8581, Japan
[b] RIKEN Center for Emergent Matter Science (CEMS), Wako, Saitama 351-0198, Japan
[c] JST ERATO Isobe Degenerate -Integration Project, Advanced Institute for Materials Research (AIMR),
Tohoku University, Sendai, Miyagi 980-8577, Japan
[d] Department of Physics, Kyoto University, Kyoto 606-8502, Japan
[e] Hiroshima Synchrotron Center, Hiroshima University, Higashi-Hiroshima 739-0046, Japan
[f] Graduate School of Science, Hiroshima University, Higashi-Hiroshima 739-8526, Japan
[g] CREST, Japan Science and Technology Agency, Tokyo 102-0075, Japan

Keywords: ARPES, Strongly correlated system, Hund metal

The perovskite ruthenate superconductor Sr_2RuO_4 has a unique (001) surface layer, consisting of RuO_8 octahedrons slightly rotated by ~8° [1, 2]. It contrasts to the case of the underlying bulk system, which shows no such distortion in the crystal structure. Previously much attention was given to the bulk state to pin down the pairing mechanism, and the compound is now believed to be a spin-triplet chiral p-wave superconductor [3]. The relevant expectation currently discussed is that it cloud be a topological superconductor, which forms the topologically protected edge. Theory predicts an emergence of Majorana fermions as the edge state, and some experimental evidence for it has been reported [4,5]. The novel edge state should stay on the boundary between the crystal surface and the underlying bulk system, thus the clarifying of electronic features on the surface and its interrelation with the bulk state is crucial for a further study on this issue.

The metallic state of Sr_2RuO_4 has been interested from the view of "Hund metals", in which the correlated state is induced by Hund's coupling under a moderate interaction U [6-8]. Notably the crucial role of Hund's coupling on electronic correlations has been recognized only recently. The key property is the crossover into an incoherent state in a low temperature regime. Importantly the suppression of the quasiparticle peak is demonstrated to be due to Hund physics, not Mott physics, by dynamical mean-field theory (DMFT). The distorted Sr_2RuO_4 surface, having an enhanced hybridization of $4d$ bands, would be an excellent platform to study the features of Hund metal. Nonetheless the investigation of it has been limited so far, suffering from a contamination by the bulk state in the experimental signature [9]. Furthermore a gradual
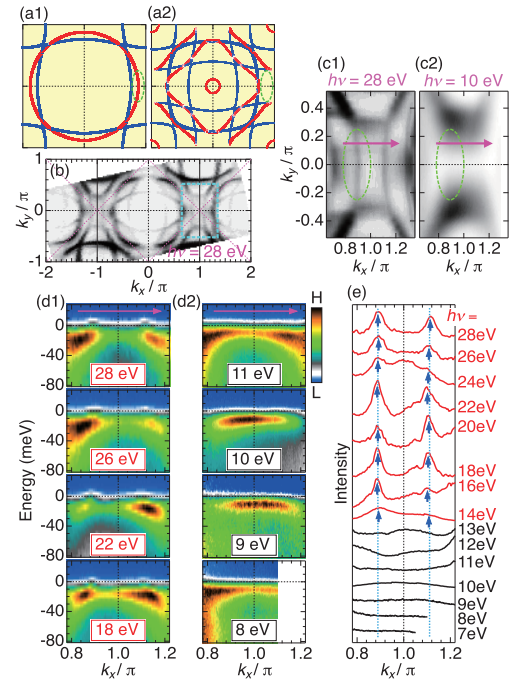

FIGURE 1. The DFT band calculations for Sr2RuO4 with no rotation (a1) and with a rotation by 8◦ (a2) for RuO8. (b) Fermi surface mapping. The magnified image around the zone edge (a light blue dashed rectangle in (b)) measured at hv =28 eV (c1) and 10 eV (c2). The green dashed ellipse marks a signature from the bulk. The ARPES dispersions along a momentum cut indicated by a magenta arrow in (c1) and (c2) are shown for a high photon energies (d1) and low photon energies (d2). (e) MDCs at the Fermi level along the same momentum cut as (d1) and (d2) measured at various photon energies. The blue arrows indicate the Fermi crossing of the bulk band.

progression of crystal distortion onto the crystal surface over the multiple RuO_8-layers is reported to cause an even more complex situation generating several splitting band [10], which thereby prevents one from fully understanding the electronic nature of the topmost layer in this compound.

In this work, we use a surface-selective angle-resolved photoemission spectroscopy (ARPES) to uncover the electronic nature on the topmost layer of Sr_2RuO_4 crystal. We find that this material has a threshold photon energy, below which only the signature of the top-most layer is selectively detected (Figure 1). Accordingly, we use ARPES with low energy photons, and reveal that the topmost-layer electrons are extremely renormalized and correlated beyond the expected rotation effect.

References

[1] R. Matzdorf et al., Science 289, 746 (2000).
[2] R. G. Moore et al., Physical Review Letters 100, 066102 (2008).
[3] A. P. Mackenzie and Y. Maeno, Reviews of Modern Physics 75, 657 (2003).
[4] L. Fu and C. L. Kane, Physical Review Letters 100, 096407 (2008).
[5] S. Kashiwaya et al., Physical Review Letters 107, 077003 (2011).
[6] K. M. Stadler, Z. P. Yin, J. von Delft, G. Kotliar, and A. Weichselbaum, Physical Review Letters 115, 136401 (2015).
[7] L. De' Medici, J. Mravlje, and A. Georges, Physical Re- view Letters 107, 256401 (2011).
[8] J. Mravlje et al., Physical Review Letters 106, 096401 (2011).
[9] A. Damascelli et al., Physical Review Letters 85, 5194 (2000).
[10] C. N. Veenstra et al., Physical Review Letters 110, 097004 (2013).

Angle resolved photoemission study of $Yb_{1-x}Tm_xB_6$

M. Arita[1], H. Sato[1], K. Shimada[1], H. Namatame[1], M. Taniguchi[1], H. Tanida[2], Y. Osanai[3], K. Hayashi[3], F. Iga[4]

[1]*Hiroshima Synchrotron Radiation Center, [2]Graduate School of Advanced Sciences of Matter,*
Hiroshima University, Kagamiyama, Higashi-Hiroshima 739-0046, Japan
[3]*Graduate School of Science and Engineering, [4]College of Science, Ibaraki University, Mito, Ibaraki, 310-8512, Japan*

Rare-earth hexaboride forms CaB_6-type cubic crystal structure. The unusual physical properties appear originated from localized $4f$ bands. Hexaboride YbB_6 has attracted researcher's interest as candidate material of topological Kondo insulator.

Recently the spin-polarized Dirac-corn-like band structure is observed by spin resolved ARPES in [001] surface for YbB_6 [1]. Although we have measured the electronic structure of YbB_6 by means of ARPES, such a band structure has not been observed yet as Yb^{2+} $4f_{7/2}$ peak is close to E_F in our samples. In this study, we have measured the electronic band structures of $Yb_{1-x}Tm_xB_6$ (x=0, 0.1, 0.2 and 0.35) by means of ARPES to clarify the band structure of the topological surface state near E_F. The whole band features for x = 0.1 and 0.2 are similar to that for x=0 and Yb^{2+} $4f_{7/2}$ and $4f_{5/2}$ peaks are observed clearly. The binding energy of the bands for x = 0.2 are ~ 100 meV higher than for x = 0. On the other hand, Yb^{2+} peaks disappear for x = 0.35 (Fig. 1). The valence transition from Yb^{2+} to Yb^{3+} occurs between x=0.2 and 0.35. Therefore, Tm-doped YbB_6 less than x = 0.2 is considered to be electron-doped YbB_6. We could measure a more detailed band structure near E_F due to the wider energy gap between E_F and Yb $4f_{7/2}$.

Figure 2 shows the obtained constant energy contours of $Yb_{0.8}Tm_{0.2}B_6$ around $\bar{\Gamma}-\bar{X}$ line with $h\nu$ = 30 eV. The Fermi surfaces are circular and the contours at E ~ −0.5eV are elliptical. Between the energies there are smaller circular contours at both $\bar{\Gamma}$ and $\bar{X}$. However, the convergence point is not found in the bands at neither of the points. According to the bulk band structure calculation for YbB_6, there are the hole- and the electron-type bands with a small overlap at X point near E_F, which are good agreement with the observed bands. It is considered that the bands are derived from the bulk states. In our results, the energy gap is not found near E_F and topological surface state is not observed in Tm-doped YbB_6 clearly.
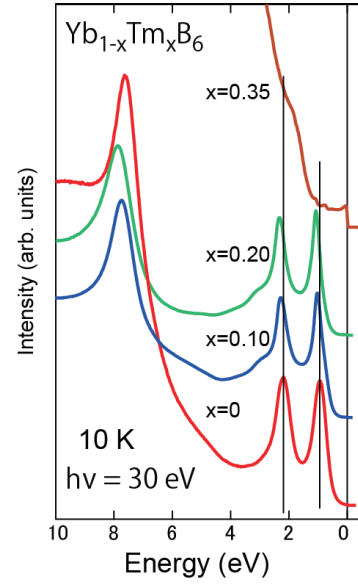

Fig.1 Photoemission spectra of $Yb_{1-x}Tm_xB_6$. Yb^{2+} peaks disappear for x=0.35.

Fig.2 Constant energy contours of $Yb_{0.8}Tm_{x0.2}B_6$.

1)   N.Xu et. al.,   arXiv:1405.0165
2)   M. Neupane et al., PRL 114, 016403 (2015)
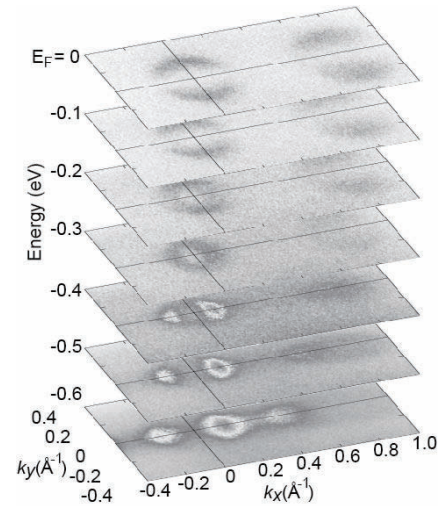
Synchrotron-Radiation Photoemission Spectroscopy of Layer-Structured Superconductor ZrP$_{2-x}$Se$_x$

Takuya Kubo[a*], Hitoshi Takita[a], Wumiti Mansuer[a], Masashi Arita[b],
Kenya Shimada[b], Hirofumi Namatame[b], Masaki Taniguchi[a,b], Sigenori Ueda[c],
Hijiri Kito[d], Shigeyuki Ishida[d], Kunihiko Oka[d], Yoshito Gotoh[d],
Hiroshi Fujihisa[d], Yoshiyuki Yoshida[d], Akira Iyo[d], Hiroshi Eisaki[d],
Kenji Kawashima[e], Yousuke Yanagi[e], and Akihiro Ino[a,b]

[a]*Department of Physical Science, Graduate School of Science, Hiroshima University,
Hiroshima 739-8526, Japan*
[b]*Hiroshima Synchrotron Radiation Center, Hiroshima University, Hiroshima 739-0046, Japan*
[c]*Advanced Materials Laboratory, National Institute for Materials Science, Tsukuba, Ibaraki 305-0044, Japan*
[d]*National Institute of Advanced Industrial Science and Technology, Tsukuba, Ibaraki 305-8568, Japan*
[e]*IMRA Material R&D Co., Ltd., Kariya, Aichi 448-0032, Japan*

In 2014, Hijiri Kito *et al.* reported a new family of layered superconducting material, $AP_{2-x}X_x$ (A = Zr, Hf; X = S, Se), made with high-pressure synthesis method [1]. The critical temperature (T_c) of $AP_{2-x}X_x$ systematically changes with chalcogen substitution x for phosphorus. The maximum T_c is about 6.3 K for ZrP$_{1.25}$Se$_{0.75}$. They crystalize in the same PbFCl-type structure as an iron-pnictide superconductor LiFeAs, as shown in Figure 1, and are mainly composed of a transition metal element A = Zr or Hf, and a light element, P. These characteristics are similar to those of high-T_c superconductors such as cuprates and iron-pnictides. Therefore, the electronic structure

FIGURE 1. Crystal structure. (a) LiFeAs. (b) ZrP$_{1.25}$Se$_{0.75}$.

of $AP_{2-x}X_x$ would provide important clues to extending our knowledge of superconductivity. However, electronic structure is uncertain because valence of phosphorus atom ranges from -3 to +5. In this study, we have investigated the electronic structure of ZrP$_{2-x}$Se$_x$ by photoemission spectroscopy.
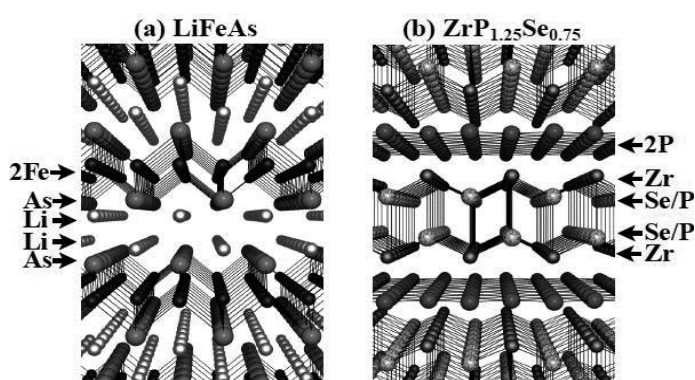
We used polycrystalline samples of ZrP$_{2-x}$Se$_x$ (x = 0.55, 0.6, 0.75 and 0.85). The sample surface was scraped *in situ* with a diamond file before the measurements. Hard X-ray photoemission spectroscopy (HAXPES) was performed at BL15XU of SPring-8, using excitation-photon energy of 5950 eV. Typical probing depth of HAXPES is the order of 100 Å, because of high kinetic energy of photoelectrons. The HAXPES spectra presented here were measured at a temperature of 20 K. High-resolution photoemission spectroscopy (HRPES) was performed at BL-9A of HiSOR in Hiroshima synchrotron radiation center, using excitation photon energies ranging from 24 to 38 eV. The HRPES spectra were measured at a temperature of about 6 K.

Figure 2 shows the HAXPES spectra of phosphorus core levels, $2p$ and $1s$, for x = 0.6 and 0.75 at T = 20 K. The spectra of P $1s$ level are plotted against the bottom axis as a function of the energy relative to Fermi level E_F. The splitting between two $1s$ peaks has been determined to be ~1.3 eV. Note that this cannot be ascribed to the

spin-orbit splitting, because the *s* orbital has no angular momentum. The spectra of P 2*p* level are plotted against the top axis as a function of energy relative to E_F. Our fitting analysis has shown that the intensity of the peak at -129.3 eV is 2 times higher than that at -130.2 eV. Thus these peaks are explained as the $p_{3/2}$ and $p_{1/2}$ states, respectively, as a result of spin-orbit splitting. In addition, another splitting of 1.3 eV similar to that of P 1*s* level has been observed also for P $2p_{3/2}$ and $2p_{1/2}$ levels. The splitting common to P 1*s*, P $2p_{3/2}$ and P $2p_{1/2}$ levels suggests the difference in the valences of the phosphorus atoms at two non-equivalent sites. As shown in Figure 1(b), the crystal structure of $ZrP_{2-x}Se_x$ has two phosphorus sites. While the in-plane (IP) phosphorus atoms constitute the two dimensional planes, the excess (EX) phosphorus atoms enter in place of selenium in the ZrSe block layers. The intensities of the peaks at -2141.7, -128.8 and -128.1 eV increase with increasing phosphorus substitution for selenium. Therefore, we ascribed these sub peaks to the EX phosphorus atoms, and the main peaks at -2143, -130.2 and -129.3 eV to the IP phosphorus atoms. The large splitting energy of 1.3 eV indicates that the valences of the in-plane and block-layer phosphorus atoms are considerably different. With reference to the energies of P 2*p* level for various metal phosphides [2], we have determined that the valences of IP and EX phosphorus atoms are about -1 and -3, respectively.

As shown in Figure 3, we observed that the spectral intensity at the Fermi level increases with increasing excitation-photon energy from $h\nu$ = 24 to 38 eV. A small structure has been recognized at 0.3 eV for the spectra taken with $h\nu$ = 38 and 5950 eV. According to the atomic calculation, the photoemission cross-section of phosphorus 3*p* states remarkably decreases as the excitation-photon energy, $h\nu$, is increased to several keV. Thus, the HAXPES intensity observed at the Fermi level is mainly ascribed to antibonding band of Zr 4*d* and Se 4*p*. Since Zr and Se are cation and anion, respectively, we ascribed the valence-band peak at 3.5 eV to Se 4*p* band, and the spectral intensity at the Fermi level to the bottom of Zr 4*d* band.

FIGURE 2. Core-level spectra of P 2*p* and 1*s*.
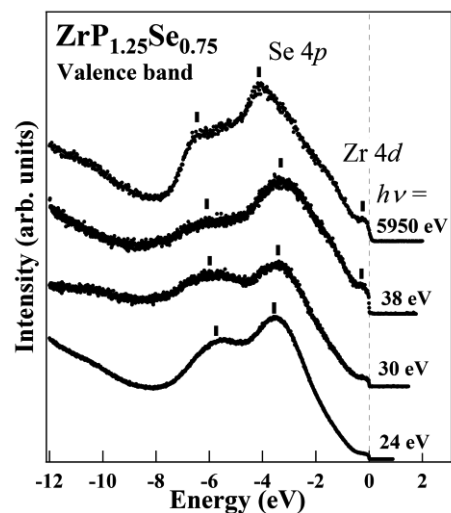
FIGURE 3. Valence-band spectra taken with $h\nu$ = 24, 30, 38, 5950 eV.

In conclusion, the electronic structure of $ZrP_{2-x}Se_x$ has been investigated by HAXPES and HRPES experiments. The energies of phosphorus core levels indicate that the roles of phosphorus atoms in two non-equivalent sites are different. The excess phosphorus substituted for selenium in block-layer plays a role of acceptors, which effectively dope holes into the valence band. In light of the valence-band spectra, we deduced that the Fermi level is located at the bottom of Zr 4*d* band. We may note some similarities between the electronic structure of $ZrP_{2-x}Se_x$ and that of another layered-pnictide superconductor β-ZrNCl (T_c = 15 K), such as the two-dimensionality, the involvement of pnictogens and the predominance of Zr 4*d* bands. In order to clarify the electronic band dispersion in $ZrP_{2-x}Se_x$, angle-resolved photoemission spectroscopy of single crystalline $ZrP_{2-x}Se_x$ is necessary.

REFERENCES

1 H. Kito, Y. Yanagi, S. Ishida, K. Oka, Y. Gotoh, H. Fujihisa, Y. Yoshida, A. Iyo, and H. Eisaki, J. Phys. Soc. Jpn. **83**, 074713 (2014).
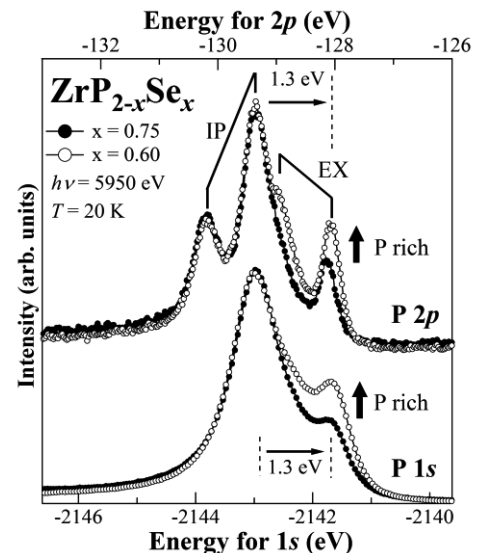2 A. P. Grosvenor, S. D. Wik, R. G. Cavell, and A. Mar, Inorg. Chem, **44** 8988 (2005).

Electronic structure studies of oxygen-concentration-controlled n-type HTSC, $(Pr,La)_{1.85}Ce_{0.15}CuO_{4-\delta}$

Dongjoon Song[a], Seungryong Park[b], Soohyun Cho[c], H. Eisaki[a] and C. Kim[d]

[a]*Electronics and Photonics Research Institute, National Institute of Advanced Industrial Science and Technology (AIST), Tsukuba 305-8568, Japan*
[b]*Department of Physics, Research Institute of Basic Sciences, Incheon National University, Incheon 22012, Korea*
[c]*Institute of Physics and Applied Physics, Yonsei University, Seoul 30722, Korea*
[d]*Center for Strongly Correlated Materials Research, Seoul National University, Seoul 08826, Korea*

Keywords: Electron doped cuprate, Annealing effect, Luttinger's sum rule.

For electron doped copper oxide superconductors (cuprates), annealing in a low oxygen atmosphere is necessary to develop superconductivity. It is believed that the heat treatment reduces the amount of impurity oxygen and allows the superconductivity to appear.[1] However, removing the oxygen impurities accompanies doping effects which need to be considered as another key ingredient in understanding the superconductivity in these systems. This is because oxygen is an anion and thus addition (removal) oxygen induces additional hole (electron) doping.[2] To access such doping effect from the annealing process, counting the total electron number though the Luttinger's sum rule is one of the most reliable methods since it directly observes the charge carrier density in the CuO_2 plane.

In this study, we performed angle resolved photoemission spectroscopy (ARPES) on an electron-doped cuprate $Pr_{1-x}LaCe_xCuO_{4\pm\delta}$ or PLCCO (x=0.15) which shows a low T_c due to over-oxygen-reduction. From the data, we observed a larger Fermi surface volume (thus, a larger carrier concentration) than that of the previously measured optimally annealed sample (see Figure 1). In addition, a rather weak pseudo gap (PG) effect is observed compared to that of the optimally annealed sample. The PG effect is considered to be a fingerprint of AF ordered state and the weak PG effect thus indicates a weakened AF order. [3] This therefore indicates that the doped electrons in the over-annealed sample weaken the AF order. From the present result, we are now establishing the electronic phase diagram of PLCCO as a function of the total electron number. Precise analysis of the electronic structure is being done. We expect that the phase diagram of electron-doped cuprates as a function of the effective doping can be constructed shortly, and it will allow us a comprehensive understanding the electronic phases.
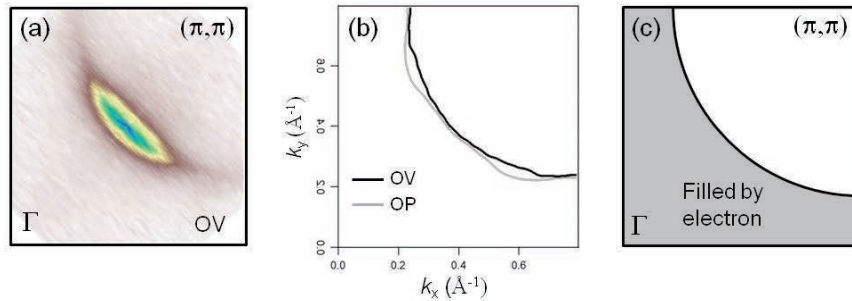

FIGURE 1. (a) Femi surface map of over-annealed (OV) PLCCO x=0.15. (b) Locus of Fermi surface for OV sample (black solid line) and optimally annealed (OP) sample (gray solid line). (c) Schematic of the Fermi surface. Shaded area is the occupied part of the Brillouin zone.

REFERENCES

1. Mishio Naito *et al.*, *Physica C* 523, (2016), pp. 28-54.
2. M. Horio *et al.*, *Nature Communications* 10567 (2016).
3. H. Matsui *et al.* Phys. Rev. B **75**, 224514 (2007)

Protected spin polarized topological surface state
on PbBi$_4$Te$_4$S$_3$

K. Sumida[a], T. Natsumeda[a], K. Shirai[a], K. Kuroda[a], S. Zhu[a], K. Miyamoto[b],
T. Okuda[b], M. Arita[b], H. Namatame[b], M. Taniguchi[b], J. Fujii[c], E. V. Chulkov[d,e],
K. A. Kokh[f,g], O. E. Tereshchenko[g,h], and A. Kimura[a]

[a]*Graduate School of Science, Hiroshima University,
1-3-1 Kagamiyama, Higashi-Hiroshima 739-8526, Japan*
[b]*Hiroshima Synchrotron Radiation Center, Hiroshima University,
2-313 Kagamiyama, Higashi-Hiroshima 739-0046, Japan*
[c]*Istituto Officina dei Materiali (IOM)-CNR, Laboratorio TASC, in Area Science Park,
S.S.14, Km 163.5, I-34149 Trieste, Italy*
[d]*Departamento de Fisca de Materiales UPV/EHU, CFM-MPC and Centro Mixto CSI-UPV/EHU,
20080 San Sebastian/Donostia, Basque Country, Spain*
[e]*Donostia International Physics Center, 20018 San Sebastian/Donostia, Basque Country, Spain*
[f]*Institute of Geology and Mineralogy, Siberian Branch, Russian Academy of Sciences,
Koptyuga pr. 3, 630090 Novosibirsk, Russia*
[g]*Novosibirsk State University, ul. Pirogova 2, 630090 Novosibirsk, Russia*
[h]*Institute of Semiconductor Physics, Siberian Branch, Russian Academy of Sciences,
pr. Akademika Lavrent'eva 13, 630090 Novosibirsk, Russia*

Keywords: Topological insulator, spin- and angle-resolved photoemission

Three-dimensional topological insulators (TIs) possess massless Dirac fermions at the surface or the interface protected by time-reversal symmetry. The spin and momentum locking, as a hallmark of TIs caused by a strong spin-orbit coupling, offers a surface or interface pure spin current. For real application, not only high spin polarization but also some physical protection of the topological surface state (TSS) is necessary because the small amount of residual gas or water easily causes the energy shift [1]. Recently, PbBi$_4$Te$_7$ has been theoretically proposed to possess the well-protected spin polarized TSS under the protecting layer [2,3], which has been verified by spin- and angle-resolved photoemission spectroscopy (SARPES) [4]. However, it can hardly be used in devices at room temperature because the bulk band gap is quite narrow (~100 meV) in PbBi$_4$Te$_7$. One solution for increasing band gap is to replace some heavy atoms with lighter isoelectronic analogs.

In this study, we focus on PbBi$_4$Te$_4$S$_3$ which has been theoretically predicted to have wide bulk band gap (~300 meV) and well-protected spin polarized TSS [5]. In order to investigate the electronic structure of this material, we performed ARPES and SARPES with synchrotron radiation at BL-9B.

Figure 1(a) shows the experimental band dispersions of PbBi$_4$Te$_4$S$_3$ taken at photon energies ($h\nu$'s) of 26, 28 and 30 eV along the $\overline{\Gamma M}$ line. At 28 eV, two Dirac cone like dispersions (DC1 and DC2) are observed within the bulk band gap [Fig. 1(a) middle panel] In contrast, there appears only outer Dirac cone (DC1) at 26 eV, while the inner one solely emerges for 30 eV [Fig. 1(a) left and right panels of Fig. 1(a), respectively]. These dispersions are very similar to the calculated TSSs if the different surface terminations are taken into account [5]. Furthermore, from ARPES data we estimated the bulk band gap to be ~220 meV, which is smaller than the calculated one but much larger than that of PbBi$_4$Te$_7$. To confirm that the observed Dirac cone like dispersions are spin polarized TSSs, we performed spin-resolved measurement. Figures 1(b) and 1(c) show the spin-resolved momentum distribution curves (MDCs) and spin polarizations taken at 26, 28 and 30 eV for the binding energies (E_B) of 0.40, 0.30 and 0.37 eV shown by white dashed lines in Fig. 1 (a). At all photon energies, the

spin polarization is reversed with respect to $\overline{\Gamma}$ point. These results strongly indicate that the both Dirac cones are TSSs.
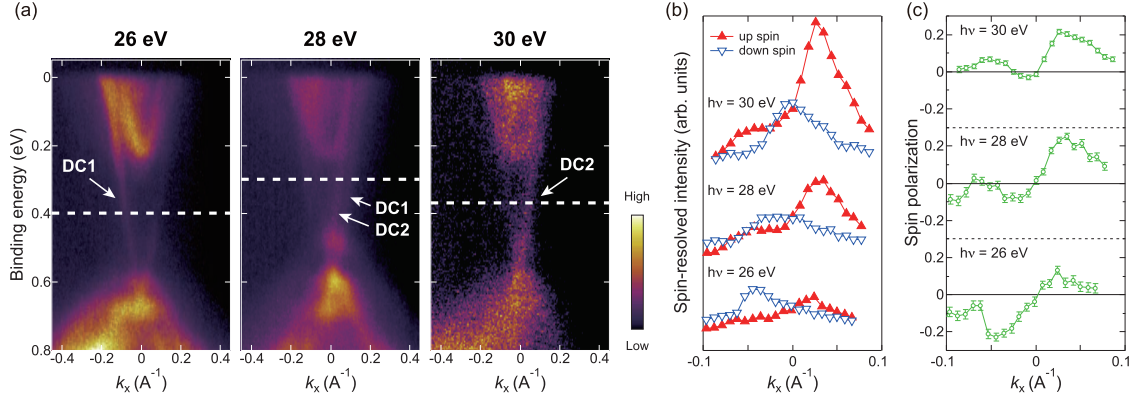

FIGURE 1. (a) Band dispersions of $PbBi_4Te_4S_3$ acquired at hv = 26, 28 and 30 eV along the $\overline{\Gamma M}$ line. (b),(c) Spin-resolved MDCs and spin polarizations obtained at hv = 26, 28 and 30 eV at E_B = 0.40, 0.30 and 0.37 eV, respectively[dashed lines in (a)].

To examine if the TSS is protected by the topmost layer or not, the crystal surface is intentionally exposed to approximately 100 Langmuir oxygen atmosphere. Figures 2(a) and 2(b) represent the pristine band dispersion taken at 28 eV and its second derivative. The white curve shown in Fig. 2(a) denotes the spin integrated MDC at E_B = 0.3 eV and we can see four prominent peaks derived from two TSSs shown by arrows. However, after oxygen exposure, the outer band disappears [Figs. 2(c) and 2(d)]. Namely, by oxygen exposure, the outer Dirac cone disappears although the inner Dirac cone survives. In addition, the Dirac point of the inner Dirac cone did not change before and after the exposure. Therefore, we conclude that $PbBi_4Te_4S_3$ has well-protected spin polarized TSS with wide bulk band gap. This finding paves a pathway for the spintronics devices operating at the real environment.
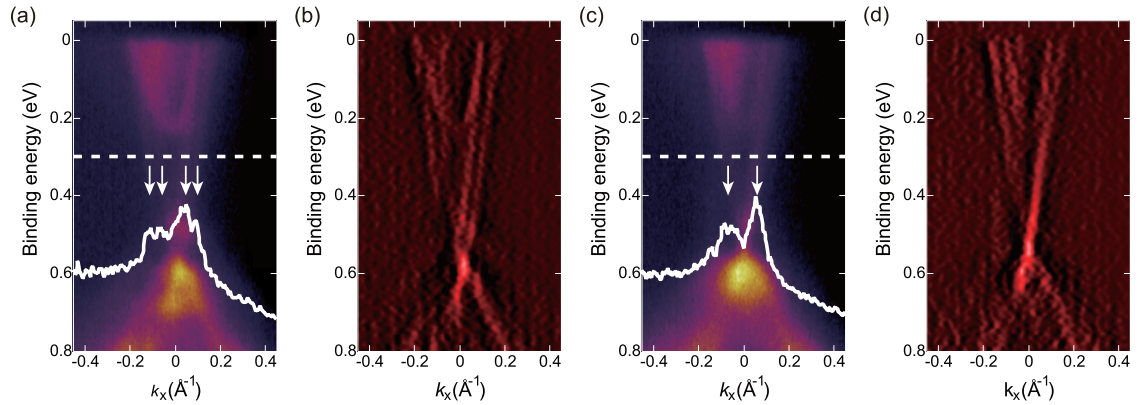

FIGURE 2. Experimental band dispersions and its second derivative acquired before (a),(b) and after oxygen exposure (c),(d). The white curves indicate the spin integrated MDCs at E_B = 0.3 eV shown by dashed lines in (a) and (c).

REFERENCES

1. H. M. Benia *et al*, Phys. Rev. Lett. **107**, 177602 (2011).
2. S. V. Eremeev, Y. M. Koroteev, and E. V. Chulkov, JETP Lett. **92**, 161 (2010).
3. S. V. Eremeev *et al.*, Nat. Commun. **3**, 635 (2012).
4. T. Okuda *et al*, Phys. Rev. Lett. **111**, 206803 (2013).
5. I. V. Silkin *et al.*, JETP Lett. **96**, 322 (2012).

Study of Spin-Polarized States in the 2D Electron System at the AlO$_x$(2Å)/SrTiO$_3$ Interface

Tobias C. Rödel[a, b], Franck Fortuna[a], Jean-Antoine Scarpaci[a], Patrick Le Fèvre[b], Yukiaki Ishida[c], Kenta Kuroda[d], Koji Minamoto[d], Kazuaki Taguchi[e], Taichi Okuda[d], Andrés F. Santander Syro[a]

[a]CSNSM, Univ. Paris-Sud, CNRS/IN2P3, Université Paris-Saclay, 91405 Orsay , France
[b]Synchrotron SOLEIL, L'Orme des Merisiers, Saint-Aubin-BP48, 91192 Gif-sur-Yvette , France
[c]The Institute for Solid State Physics, The University of Tokyo, Kashiwa, Chiba 277-8581, Japan
[d]Hiroshima Synchrotron Radiation Center, Hiroshima University, Higashihiroshima, Hiroshima 739-0046, Japan
[e]Graduate School of Science, Hiroshima University, Higashihiroshima, Hiroshima 739-8526, Japan

The 2D electron systems (2DESs) at interfaces between SrTiO$_3$ (STO) and other insulating transition-metal oxides (TMOs) are a field of current intense research [1-4]. For instance, the celebrated LaAlO$_3$/SrTiO$_3$ interface presents superconductivity below 200 mK [4, 5], superconductor-insulator transitions that can be tuned with an external voltage [2, 5], or large magnetoresistance [6]. Recently, we discovered how to create 2DESs at different surfaces of the transparent insulating oxides SrTiO$_3$ and KTaO$_3$ (KTO) [7-10]. Additionally, using spin-resolved ARPES at the Swiss Light Source, we measured a strong spin polarization of the 2DES at the bare surface of SrTiO$_3$ [11]. It is thus crucial to deepen our understanding of those results in SrTiO$_3$, and study the possible emergence of spin-polarized states in other oxides. The unmatched detection efficiency of the recently developed ESPRESSO station, combined with its unique capacities in terms of *in-situ* sample preparation, represent clear advantages to address the above issues with respect to other spin-ARPES stations in the world.

A high flux of UV photons is essential to obtain a large amount of surface oxygen vacancies, which are responsible for the formation of the 2DESs in these oxides. We found that the photon flux in HiSOR was not high enough to fabricate a 2DES with a large density of carriers at the bare (*i.e.*, cleaved or annealed *in-situ*) surface of SrTiO$_3$. To overcome such difficulty, we used a technique we recently developed to generate the 2DESs in oxides without the need of UV radiation [12]: evaporating *in-situ* one monolayer of aluminum on the oxide surface. By an efficient redox reaction, the aluminum oxidizes by pumping oxygen from the oxide surface, and creates a pristine 2DES directly observable by ARPES through the resulting thin AlO$_x$-capping layer.

Thus, we measured the 2DES at the AlO$_x$(2Å)/SrTiO$_3$ interface around the Γ_{102} point. The 3D spin-resolved ARPES data was obtained at the ESPRESSO machine (BL-9B), using 47 eV photons with linear-vertical polarization. The energy and angular resolutions in spin-resolved mode were 65 meV and 1.5 degrees, respectively. The measurement temperature was 10K.

Figure 1(a) shows the experimental geometry. Due to the rotation of the sample, the measured X component of the electron spin in the laboratory frame includes X' and Z' components in the reference frame of the sample. Thus, the measured intensities I$_a$ and I$_b$ of opposite spin direction along X correspond to approximately 75% of the component along X' in the sample's frame. The Y and Y' components of the electron spin coincide in the two reference frames. Figure 1(b) shows a schematic of the Fermi surface, and Fig. 1(c) the energy-momentum map measured using ARPES, where the two d_{xy} subbands typical of the 2DES in SrTiO$_3$ can be clearly observed. Figures 1(b,c) also show, respectively, the directions in reciprocal space and the binding energy of the spin-resolved measurements, with the experimental resolutions represented by the width of the measurement lines. We focus henceforth on the component of the spin polarization tangential to the Fermi surface, which is characteristic of a Rashba-like spin splitting. Figure 1(d) shows the spin-resolved momentum distribution curves (spin-MDCs) for electron momentum along $k_{<010>}$ (or Y') and electron spins parallel (I$_a$) and anti-parallel (I$_b$) to X, and the corresponding spin asymmetry (A), measured at the Fermi level. Fig. 1(e) shows analogous data for electron momentum along $k_{<100>}$ (or X') and electron spins parallel (I$_a$) and anti-parallel (I$_b$) to Y' = Y. Figures 1(f, g) are the same as Figs. 1(d, e) at a binding energy of 30 meV. From this data, we conclude that the 2DES at

the $AlO_x(2\text{Å})/SrTiO_3$ interface does not show any significant spin polarization, contrary to the results obtained at the Swiss Light Source on the bare $SrTiO_3$ surface. Further experiments are needed to clarify if the different results are intrinsic, *e.g.* due to dissimilar surface preparation methods (bare surface *vs* Al-capped surface), or extrinsic, due to systematic errors in one of the experimental setups.

An appealing output of our experiments is that, using the new Al-capping method [12] in conjunction with the state-of-the-art ESPRESSO machine, it becomes feasible to study by 3D spin-ARPES the possible spin-polarization of other 2DESs at the surface of other transition-metal oxides.
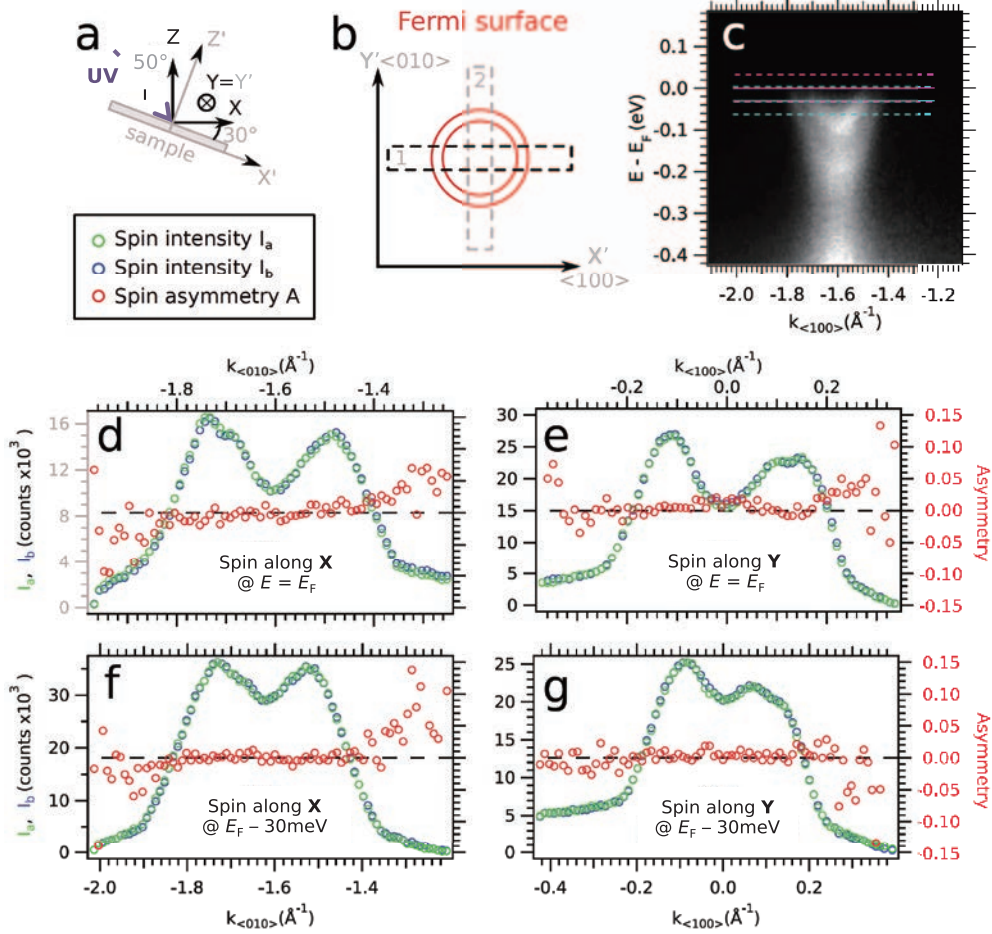

FIGURE 1. (a) Experimental geometry. (b) Schematic Fermi surface of the 2DES at the $AlO_x(2\text{Å})/SrTiO_3$ interface. (c) Energy-momentum ARPES map of the light d_{xy} subbands forming the concentric Fermi circles shown in (b). (d) Spin-MDCs along $k_{<010>}$ (or Y') for electron spins parallel (I_a) and anti-parallel (I_b) to X, and corresponding spin asymmetry (A), measured at the Fermi level. (e) Analogous to (d) for electron momentum along $k_{<100>}$ (or X') and spins (anti-)parallel to Y' = Y. (f, g) Same as (d, e) at a binding energy of 30 meV.

REFERENCES

1. A.Ohtomo and H.Y.Hwang, Nature **427**, 423 (2004).
2. S. Thiel *et al.,* Science **313**, 1942-1945 (2006).
3. K. Ueno *et al.,* Nature Mater. **7**, 855-858 (2008).
4. H. Nakamura *et al.,* J. Phys. Soc. Jpn. **78**, 083713 (2009).
5. N. Reyren *et al.*, Science **317**, 1196-1199 (2006).
6. A. Brinkman *et al.,* Nature Mater. **6**, 493-496 (2007).
7. A. F. Santander-Syro *et al.*, Nature **469**, 189-193 (2011).
8. A. F. Santander-Syro *et al.,* Phys. Rev. B **86**, 121107(R) (2012).
9. C. Bareille *et al.*, Sci. Rep. **4**, 3586 (2014).
10. T. C. Rödel *et al.*, Phys. Rev. Applied **1**, 051002 (2014).
11. A. F. Santander-Syro *et al.*, Nature Mater. **13**, 1085 (2014).
12. T. C. Rödel *et al.*, Adv. Mater **28**, 1976 (2016).

Spin and Electronic Structure of a Magnetic/Topological Insulator Ultrathin Film Heterostructure

Yuma Okuyama[a], Kazuki Sumida[b], Koji Miyamoto[c], Taichi Okuda[c], Toru Hirahara[a]

[a]*Department of Physics, Tokyo Institute of Technology, 2-12-1, Ookayama, Tokyo 152-8551, Japan*
[b]*Graduate School of Science, Hiroshima University, 1-3-1 Kagamiyama, Higashi-Hiroshima 739-8526, Japan*
[b]*Hiroshima Synchrotron Radiation Center, Hiroshima University, 1-3-1 Kagamiyama, Higashi-Hiroshima 739-8526, Japan*

Topological insulators (TI) are extensively studied recently due to its peculiar properties [1]. The Dirac-cone surface states of TI are protected by time-reversal symmetry (TRS) and backscattering among these surface states is prohibited. But when TRS is broken by application of a magnetic field or incorporating magnetic materials, a gap opening in the Dirac cone is expected and an intriguing phase called the quantum anomalous Hall state can be realized [2]. This phase is expected to show even more exotic phenomena such as the topological magnetoelectic effect. To realize such states, two types of sample fabrication techniques have been employed up to now: (1) magnetic doping while growing the single crystal or thin film of TI [3], and (2) magnetic impurity deposition on the surface of TI [4]. While method (1) was successful and showed evidence of the TRS violation, no one has succeeded using method (2), which should be a more direct way to examine the interaction between the topological surface states and magnetism.

In the present work, we have attempted an alternative approach to break the TRS in TI: making a heterostructure of TI and magnetic insulators (MI) and making use of the magnetic proximity effect at the interface. For this purpose, we have fabricated a heterostructure of MnSe (MI) and Bi_2Se_3 (TI) since the lattice mismatch between the two materials is relatively small (~6%). MnSe is a layered structure and is antiferromagnetic as a whole, but in each Mn layer, the spin is oriented in one direction (ferromagnetic within the layer and antiferromagnetic among the adjacent layers) [5]. Thus one can expect that the ferromagnetic Mn layer will break TRS of TI. Figure 1 shows the band dispersion of the surface states of the 2BL $MnSe/Bi_2Se_3$ heterostructure. (a) shows the raw data and (b) is the second derivative of (a). One can find a clear gap of ~ 60 meV at the Dirac point, meaning that it has turned into in a massive Dirac cone which was originally massless for pristine Bi_2Se_3. This result shows that our method is indeed a promising way to induce TRS breaking in TI surface states.

Figure 2 shows the result of the spin- and angle-resolved photoemission measurements at off normal emission ($\theta = \pm 1.5°$). The red (blue) curves show the spin-polarized spectra for the + (-) spin and the green curve shows the spin-polarization. The measured spin direction is tangential to the wavenumber. No spin-polarization was observed for the other spin directions. One can see that the Dirac cone is clearly spin-polarized and the spin structure is antisymmetric with respect to the Γ point ($\theta = 0°$). Further sophisticated measurements will be performed to see the direct evidence of the TRS breaking after magnetizing the sample in the in-plane and out-of-plane directions.
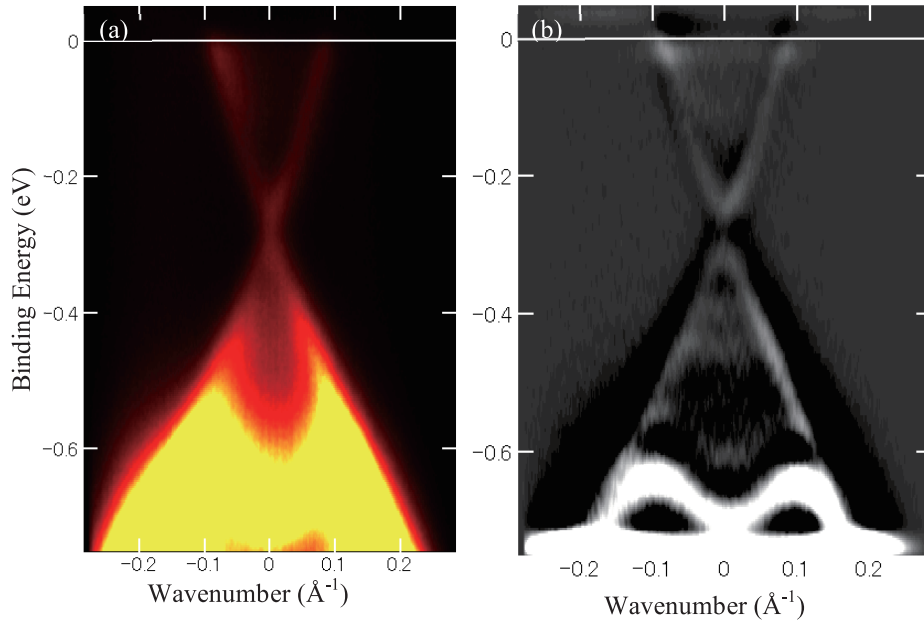
(a)

Binding Energy (eV): 0, -0.2, -0.4, -0.6

Wavenumber (Å^{-1}): -0.2, -0.1, 0, 0.1, 0.2

(b)

Wavenumber (Å^{-1}): -0.2, -0.1, 0, 0.1, 0.2

Fig. 1
Band structure of a 2BL MnSe/Bi$_2$Se$_3$ heterostructure. Raw data (a), and second derivative of (a), (b) respectively. A clear gap opening of ~60 meV is observed at the Dirac point meaning that it is a massive Dirac cone.
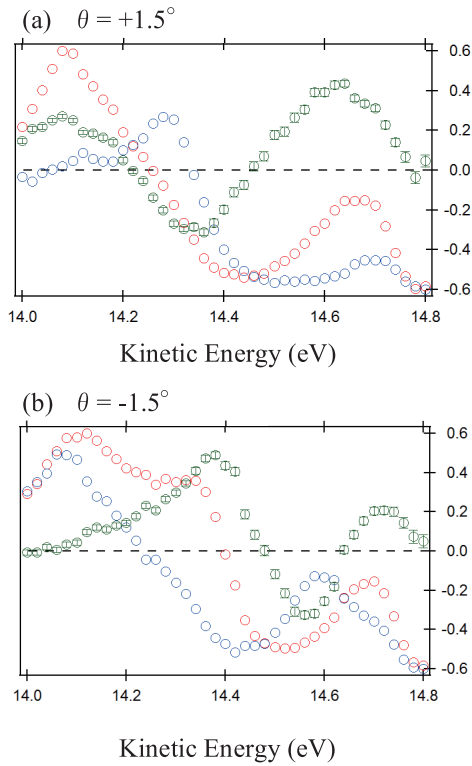

(a) $\theta = +1.5°$

Kinetic Energy (eV)

(b) $\theta = -1.5°$

Kinetic Energy (eV)

Fig. 2
The result of the spin- and angle-resolved photoemission measurements at off normal emission ($\theta = \pm 1.5°$). The red (blue) curves show the spin-polarized spectra for the + (-) spin and the green curve shows the spin-polarization. One can see that the Dirac cone is clearly spin-polarized and the spin structure is antisymmetric with respect to the Γ point ($\theta = 0°$).

REFERENCES

1. M. Hasan and C. Kane, Reviews of Modern Physics **82**, 3045 (2010).
2. X.-L. Qi and S.-C. Zhang, Reviews of Modern Physics **83**, 1057 (2011).
3. For example, C. Z. Chang *et al.,* Science **340**, 167 (2013).
4. For example, M. Ye *et al.,* Physical Review B **85**, 205317 (2012).
5. R. J. Pollard *et al.,* J. Phys. C: Solid State Phys. **16**, 345 (1983).

Exchange coupling and spin structure
in cobalt-on-chromia thin films

Takashi Komesu[a], K. Taguchi[b], T. Okuda[c], K. Miyamoto[c],
R. Choudhary[a, d], P. Sahota[d], P. Manchanda[a], R. Skomski[a],
A. Kashyap[d], and Peter A. Dowben[a]

[a]*Department of Physics and Astronomy, Nebraska Center for Materials and Nanoscience,*
Theodore Jorgensen Hall, 855 N 16th, University of Nebraska, 880299, Lincoln, NE 68588-0299, U.S.A.
[b]*Graduate School of Science, Hiroshima University, Higashi-Hiroshima, Hiroshima 739-6526*
[c]*Hiroshima Synchrotron Radiation Center, Hiroshima University,*
Higashi-Hiroshima 739-0046, Japan
[d]*Dept. of Physics, School of Basic Sciences, Indian Institute of Technology Mandi,*
Mandi, Himachal Pradesh − 175001, India

Keywords: Spin Polarized Photoemission Spectroscopy, Electronic Structure.

Chromia (Cr_2O_3) continues to attract much attention as a magneto-electric material [1-8], with a Néel temperature above room temperature [1]. One interesting feature of this antiferromagnetic (AFM) is the significant boundary spin polarization at the (0001) surface [1-3,8]. This boundary polarization can be isothermally controlled to provide perpendicular voltage controlled exchange-bias in an adjacent ferromagnet [1,4-7]. Cobalt thin films on nonmagnetic substrates tend to have a preferred magnetization direction in the plane of the film (in-plane anisotropy) [9]. Yet the magnetic coupling at the interface of $Co/Cr_2O_3(0001)$ leads to a more complexity magnetic interface [6,7,10]. There is clear evidence from X-ray magnetic dichroism that the coupling between Co and $Cr_2O_3(0001)$ is antiferromagnetic at the interface [10]. Since the magneto-crystalline c-axis anisotropy of chromia supports a perpendicular magnetization orientation, that the interface exchange can be exploited to add a perpendicular component to the Co magnetization, with antiferromagnetic coupling at the interface [4].

For the spin polarized photoemission studies, the Cr_2O_3 surface was prepared with several cycles of Ar^+ sputtering and annealing up to 900° C and subsequent annealing (450 °C) in oxygen, and the cobalt grown at lower temperatures (below room temperature), as found to be favorable in prior studies [9]. The LEED pattern, not shown here, confirmed the clear C_{3v} crystallographic structure of the Cr_2O_3 surface after annealing in O_2. The Cr_2O_3 sample was magneto-electrically field cooled in applied E and B fields through the chromia Néel temperature (307 K) and then cooled down to 160 K, as previously explained [1,4,5,9].

Figure 1 shows the spin-polarized photoemission spectra for a 10 nm thick Co overlayer deposited on top of Cr_2O_3 at 160 K, performed at HiSOR (BL-9B), using the very low energy electron diffraction (VLEED) spin detector as described elsewhere [11] and a photon energy of 60 eV. The red (blue) circles in Figure 1 indicate spin up (down) components, respectively, and the green circles indicate the spin asymmetry of the polarization. The dominant peaks at −0.4 eV arises from the cobalt 3d states, similar to prior spin polarized photoemission spectra of cobalt thin films on copper [12]. Comparison of Figure (a) and (b) reveals substantial Co spin projections both parallel and perpendicular to the film plane. This is indicative of a canted spin alignment of the cobalt adlayer, and, constrained by the E and B field cooling geometry, with the cobalt moments antiparallel with the substrate chromia at the interface. The canting is consistent with micromagnetic
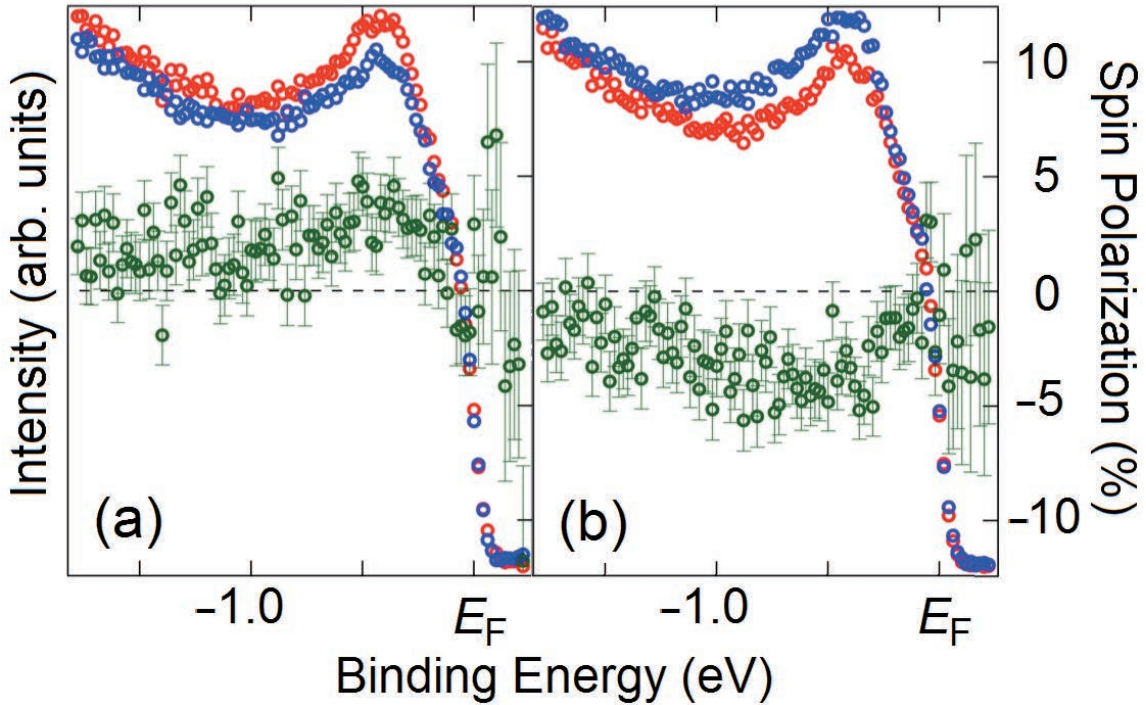
simulations and magnetic force microscopy.

Figure 1. The spin-polarized photoemission spectra for 10 nm Co on top of Cr_2O_3: (a) the measured in-plane spin polarization and (b) perpendicular (out-of-plane) spin polarization. The red (blue) circles indicate spin up (down) components, respectively, and the green circles indicate the spin asymmetry of the polarization.

References

[1] X. He, Y. Wang, N. Wu, A. N. Caruso, E. Vescovo, K. D. Belashchenko, P. A. Dowben, and C. Binek, Nat. Mater. **9**, 579 (2010).

[2] S. Cao, X. Zhang, N. Wu, A. T. N'Diaye, G. Chen, A. K. Schmid, X. Chen, W. Echtenkamp, A. Enders, Ch. Binek, P. A. Dowben, New J. Physics **16**, 073021 (2014).

[3] N. Wu, X. He, A. L. Wysocki, U. Lanke, T. Komesu, K. D. Belashchenko, C. Binek, and P. A. Dowben, Phys. Rev. Lett. **106**, 087202 (2011).

[4] W. Echtenkamp, and Ch. Binek, Phys. Rev. Lett. **111**, 187204 (2013).

[5] K. Toyoki, Y. Shiratsuchi, A. Kobane, S. Harimoto, S. Onoue, H. Nomura, and R. Nakatani, J. Appl. Phys. **117**, 17D902 (2015).

[6] T. Ashida, M. Oida, N. Shimomura, T. Nozaki, T. Shibata, and M. Sahashi, Appl. Phys. Lett. **106**, 132407 (2015).

[7] K. Toyoki, Y. Shiratsuchi, A. Kobane, C. Mitsumata, Y. Kotani, T. Nakamura, and R. Nakatani, Appl. Phys. Lett. **106**, 162404 (2015).

[8] K. D. Belashchenko, Phys. Rev. Lett. **105**, 147204 (2010).

[9] S. Cao, X. Zhang, T. Komesu, G. Chen, A. K. Schmid, L. Yue, I. Tanabe, W. Echtenkamp, Y. Wang, Ch. Binek, and P. A. Dowben, J. Phys. Conden. Matter **28**, 046002 (2016).

[10] Y. Shiratsuchi, Y. Kotani, S. Yoshida, Y. Yoshikawa, K. Toyoki, A. Kobane, R. Nakatani, and T. Nakamura, AIMS Materials Science **2**, 484-496 (2015).

[11] T. Okuda, K. Miyamoto, H. Miyahara, K. Kuroda, A. Kimura, H. Namatame, and M. Taniguchi, Rev. Sci. Instrum. **82**, 103302 (2011).

[12] E. Vescovo, C. Carbone, U. Alkemper, O. Rader, T. Kachel, W. Gudat, and W. Eberhardt, Phys. Rev. B **52**, 13497 (1995).

Spin-polarization in the electronic structure of strongly correlated surface alloys

Hendrik Bentmann, Henriette Maaß, Christoph Seibel, Friedrich Reinert

^{a}Experimentelle Physik 7, University Würzburg, Am Hubland, 97074 Würzburg, Germany

The topological insulator Bi_2Te_3 shows a surface Dirac-state whose dispersion shows a strong hexagonal warping due to the influence of the threefold crystal potential [1,2]. This influence can also be observed in the photoemission matrix element which, depending on photon energy, can show pronounced threefold modulations across the Fermi surface or a more isotropic distribution. It is therefore of interest to study also the influence of the crystal symmetry on the spin polarization of the photoelectrons in Bi_2Te_3.

Here, we have studied the photoelectron spin polarization of the Dirac-state in Bi_2Te_3 using p-polarized and circularly polarized light for photon energies between ca. hv = 22-50 eV. We observe a clear influence of the threefold crystal symmetry on the photoelectron spin polarization (PSP) (see Figure 1). In particular, we find an out-of-plane component in the PSP that becomes maximal along the $\overline{\Gamma K}$ direction, changes sign upon sample rotation by 60°, and vanishes along $\overline{\Gamma M}$, i.e. within the mirror plane. Similar to the photoemission intensity, also these observed threefold modulations of the PSP are quite strongly dependent on photon energy. We find that depending on photon energy and polarization the out-of-plane component modulates between values of ca. 0.2 and -0.2. A detailed theoretical modelling of the experimental data, based on one-step photoemission theory, shall provide additional insights into the contributions of initial and final states to the threefold modulations of the PSP.

REFERENCES

1. L. Fu, Phys. Rev. Lett. **103**, 266801 (2009).
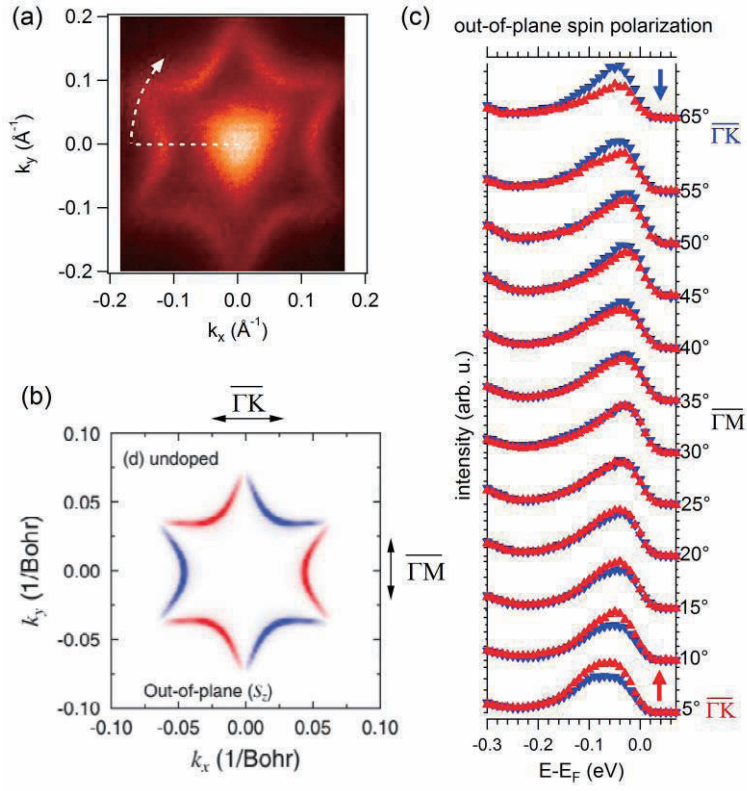2. J. Henk et al., Phys. Rev. Lett. **108**, 206801 (2012).

Figure 1: a) ARPES Fermi surface showing the topological surface state (TSS) with strong hexagonal warping (outer feature). (b) Calculated Fermi surface of the TSS with the red/blue color code referring to the out-of-plane spin polarization S_z with threefold symmetry [taken from Henk et al., PRL 108, 206801 (2012)]. (c) Spin-resolved energy distribution curves (P_z component) acquired at $-k_x$ with p-polarized light ($h\nu = 23$ eV) incident along x. Successive measurements for different azimuthal orientations of the sample confirm the threefold symmetry of P_z.

Spin-split surface bands of Si(111)5×2-Au

Kazuaki Taguchi[a] , Kazuki Sumida[a] , Koji Miyamoto[b] , Hirofumi Namatame[b] , Masaki Taniguchi[b] ,Akio Kimura[a] and Taichi Okuda[b]

[a] *Graduate School of Science, Hiroshima University,*
1-3-1 Kagamiyama, Higashi-Hiroshima, Hiroshima 739-8526, Japan
[b] *Hiroshima Synchrotron Radiation Center, Hiroshima University,*
2-313 Kagamiyama, Higashi-Hiroshima, Hiroshima 739-0049, Japan

It is well known that metal adsorption on semiconductor surface shows variety of surface reconstruction. Especially metal induced surface reconstruction on Si surface has been investigated extensively so far because Si is the most widely used semiconductor for the real electronics devices. Among the metal adsorbed Si surfaces, Au on Si(111) is one of the systems which has been most thoroughly investigated since the many reconstructed surfaces such as 5×2, α-√3×√3, β-√3×√3 and 6×6 appear as the function of the amount of Au and annealing temperature. In these reconstructions Si(111)5×2-Au surface might be the most intriguing system since the system has one-dimensional structure and can be a playground for the low-dimensional physics[1]. Despite of the extensive investigation, even the structure of the surface had long debate and thus the relation between electronic structure and the atomic structure has not been fully understood. One interest on the electronic structure of the sample is spin structure. Although similar one-dimensional Au atomic chain systems on vicinal Si(111) such as Si(557)-Au, Si(553)-Au and so on have been revealed that the systems have Rashba spin splitting surface states[2,3], the existence of similar spin-split states on the Si(111)5×2-Au has not yet been investigated so far.

In this work, we have investigated spin electronic structure of the Si(111)5×2-Au surface by spin- and angle-resolved photoemission spectroscopy (SARPES) for the first time. The measurement has been done at beamline BL-9B in Hiroshima Synchrotron Radiation Center (HiSOR) using Efficient SPin REsolveod SpectroScOpy (ESPRESSO) machine. *p*-polarized light at hν=34 eV from APPLE-II type undulator was used for the measurement.

Figure 1(a) shows the observed band structure of Si(111)5×2-Au along gold atomic chain (// k_x) taken by spin-integrated ARPES measurement (top) as well as the schematic of the observed band structure (bottom). Surface states bands are labeled in accordance with the previous study [4]. As seen in the figure, surface states labeled S_2' cross the Fermi level. It indicates the metallic character of the surface. In addition, these surface states show no significant dispersion along k_y *i.e.* perpendicular to the gold atomic chain (not shown here). Thus, the observed surface states possess one-dimensional character. In order to investigate the spin texture of the bands, we have measured the spin-resolved momentum distribution curve (spin-MDC) along gold atomic chain direction at E_B = 0.6 eV (along the red horizontal line in Fig.1 (a)). At the binding energy the S_1 states are dominant and observed as peaks in the MDC curve of total intensity (black circles) of Fig. 1(b). In the spin-resolved MDC data (in which spin

polarization along perpendicular to k_x is observed) the small shift in k is observed between spin up (red upward triangles) and spin down (blue downward triangles) states. Namely, peak positions of spin up state shift to positive wave numbers while those of spin down state shift to negative wave numbers near ZB'_{x2} and ZB_{x2} symmetry line. The direction of peak shifts is in good agreement with the typical Rashba spin split states. In addition, similar shifts between spin up and down states are also observed at the Fermi level (not shown here) and plotted the peak positions in Fig. 1(a) with upward and downward triangles. Thus, the $S_{2'}$ states are also spin splitting by Rashba effect. In Fig. 1(c), spin-resolved energy distribution curves taken at $k_x = 0.525$ and $-0.515\,\text{Å}^{-1}$(red vertical lines in Fig. 1(a)) are shown. Again at the binding energies of S_1 state, we can clearly see the energy shift between spin up and spin down states and the direction of energy shifts are opposite each other being consistent with the typical Rashba spin split states. Meanwhile the state near the Fermi level (S_2) does not show clear shift in the spin-EDC.

In summary, we have investigated the spin texture of Si(111)5×2-Au. As the results, clear evidence of Rashba spin split is obtained in the gold induced one-dimensional surface electronic structures of the surface.
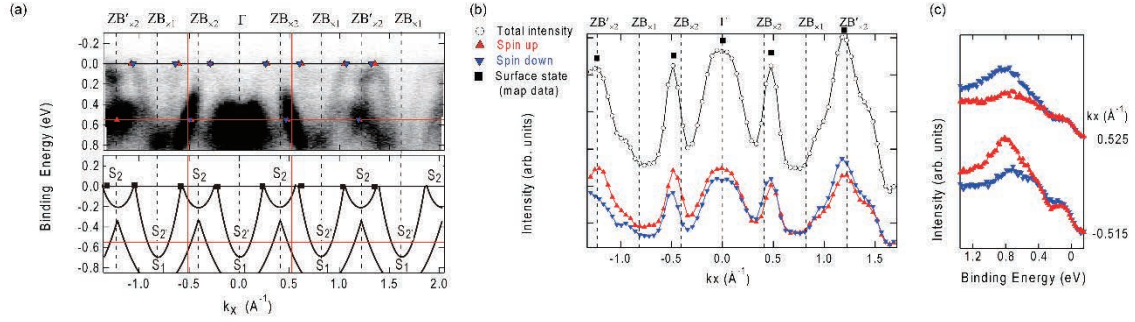

FIGURE 1. (a)Angle resolved photoemission (ARPES) spectra of Si(111)5×2-Au taken along gold atomic chain direction (top) and the schematic of the observed band structure (bottom). (b) Spin-resolved momentum distribution curve (spin-MDC) taken at $E_B = 0.6$ eV (along the red horizontal line in (a)). (c) Spin-resolved energy distribution curve (spin-EDC) at k_x=0.525 and -0.515 Å^{-1} (red vertical line in (a)).

REFERENCES

1. J. N. Crain *et al.*, *Phys. Rev. B.* **69**, 125401 (2004).

2. T. Okuda *et al*, *Phys. Rev. B.* **82**, 161410(R) (2010).,

3. H.W. Yeom *et al.*, New J. Phys. **16**, 093030 (2014).

4. J. L. McChesney *et al*, *Phys. Rev. B.* **70**, 195430 (2004).

Change of electronic structure of Ir(111) by Pb adsorption

Y. Okuda[a], K. Miyamoto[a], K. Sumida[b], K. Taguchi[b], T. Yoshikawa[b], N. Takagi[c], R. Arafune[d], and T. Okuda[a]

[a]*Hiroshima Synchrotron Radiation Center, Hiroshima University, Japan,*
[b]*Graduate School of Science, Hiroshima University, Japan,*
[c]*Department of Advanced Materials Science, The University of Tokyo, Japan,*
[d]*International Center for Materials Nanoarchitectonics (WPI-MANA), National Institute for Materials Science (NIMS), Japan*

Keywords: Rashba effect, Spin-resolved photoemission, Quantum Hall effect, Graphene

Introduction

Because of the extremely high mobility of electron in the Dirac cone and the weak spin-orbit (S-O) interaction of carbon, graphene is expected to be a good spin conserver or an ideal medium of spin transport in the future spintronic devices. On the other hand, to induce spin related phenomena by enhancing the S-O interaction in graphene is also demanded for the spintronics application.

It has been reported recently that Landau-like levels appeared without applying real magnetic field in the graphene grown on Ir(111) by Pb intercalation which is forming c(4x2) periodicity[1]. According to the report the spatial modification of S-O coupling in graphene sheet by the intercalation of heavy Pb atoms produces pseudo magnetic field and cause the Landau-like levels. However, the effect of c(4x2)-Pb formation on the electronic structure of Ir(111) substrate is not clear. Thus, we have investigated the electronic band structure of Ir(111) surface and its change by Pb adsorption.

Experimental

All the experiments have been done at the Efficient SPin REsolved SpectroScOpy (ESPRESSO) endstation[2] at beamline BL-9B of Hiroshima Synchrotron Radiation Center. At the station normal angle resolved photoelectron spectroscopy (ARPES) and spin-resolved ARPES measurements can be carried out with variable light polarization from APPLE II undulator. In addition, with the double VLEED spin detectors of ESPRESSO machine one can realize 3D spin vector analysis[3].

Ir(111) single crystal was cleaned by several cycles of Ar+ spattering at 1 keV and annealing at 1400 ℃ and following high temperature flashing at 1700 ℃. The quality of the clean surface is confirmed by low energy electron diffraction (LEED), Auger electron spectroscopy and the clear surface states by photoemission measurement. 1/4 ML Pb evaporation from knudsen-cell to the Ir(111) surface and postannealing at 430 ℃ result in the formation of Ir(111)c(4x2)-Pb surface.

Obtained spin-ARPES results are compared with the DFT calculation using VASP code with the projected augumented wave (PAW) potentials.

Results & Discussion

Figures 1 show the observed band structure of clean Ir(111) taken with the photon energy of 50 eV with *p*-polarized light along (a) $\overline{\Gamma}$-$\overline{M}$ and (b) $\overline{\Gamma}$-$\overline{K}$ direction. The parabolic band with convex upward at the $\overline{\Gamma}$ point is surface resonance band which is reported as the Rashba spin split state in the previous paper[4]. While the band split is not evident at $\overline{\Gamma_1}$ point but clear split is observed at $\overline{\Gamma_2}$ point. The direct evidence of spin splitting has been also confirmed by our spin-ARPES observation (not shown here) and in good agreement with the previous results[4]. Our 3D spin vector analysis as well as the DFT calculation reveal that the states are the trivial Rashba spin split states like the Shockley state of Au(111) having only in-plane tangential spin polarization. Besides the state the other surface state band at around $\overline{K}$ point in Fig. 1(b) and (c) shows interesting band split which is not in *k* but in energy unlike the normal Rashba spin split states. Our spin-ARPES results show that the state has almost 100 % out-of-plane spin polarization. The observed out-of-plane spin polarization is caused by the C_3

symmetry of the electronic structure of Ir(111) at $\overline{K}$ point which has been found in Si(111)1x1-Tl system[5] and also can be reproduced very well by our DFT calculation.

These surface states of pristine Ir(111) surface is strongly modified by Pb adsorption as in Fig. 2(a) and (b). The Rashba spin split band at $\overline{\Gamma}$ is shifted to higher binding energies and the photoemission intensity as well as the spin polarization are reduced. The reduction of out-of-plane spin polarization is also observed in the spin split band at $\overline{K}$ point. The results indicate that the Pb adsorption on Ir(111) does modify the spin texture of Ir(111) but not enhance the spin polarization of the system both in-plane and out-of-plane components.

(a) (b) (c)
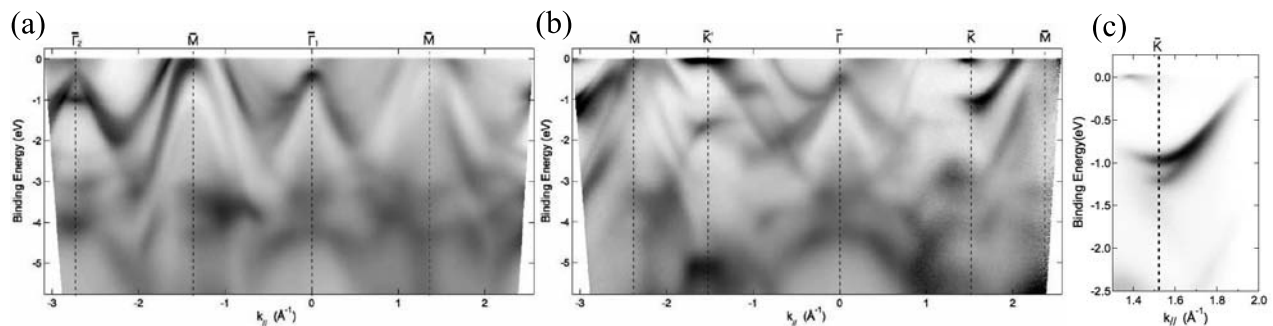
Figure 1: The band structure of Ir(111) clean surface along (a) $\overline{\Gamma}$-$\overline{M}$ and (b) $\overline{\Gamma}$-$\overline{K}$ direction. (c) Detailed band structure at $\overline{K}$.

(a) (b)
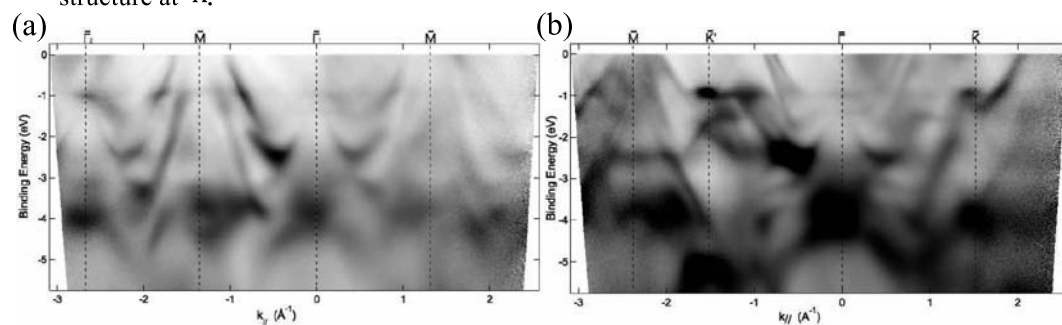
Figure 2: The band structure of Ir(111)c(4x2)-Pb along (a) $\overline{\Gamma}$-$\overline{M}$ and (b) $\overline{\Gamma}$-$\overline{K}$ direction.

REFERENCES

1. – F. Calleja et al., Nat. Phys. **11**, 43(2015).
2. – T. Okuda et al., Rev. Sci. Instrum. **82**, 103302 (2011).
3. – T. Okuda et al., J. Electron Spectros. Relat. Phenomena **201**, 23 (2014).
4. – A. Varykhalov *et al.*, Phys. Rev. Lett. **108**, 066804 (2012).
5. – K. Sakamoto *et al.*, Phys. Rev. Lett. **102**, 096805 (2009).

Identifying sulfur species in marine sediments collected from Osaka Bay using XAFS

Satoshi ASAOKA[a], Hideo OKAMURA[a], Yasuhiro USHIHARA[a]
Toru ENDO[b], Ayaka TAMURA[c] and Shinjiro HAYAKAWA[c]

[a] Research Center for Inland Seas, Kobe University (5-1-1 Fukaeminami Higashinada Kobe 658-0022 Japan)
[b] Graduate School of Engineering, Osaka City University (3-3-138 Sugimoto, Sumiyoshi-ku, Osaka 558-8585 Japan)
[c] Graduate School of Engineering, Hiroshima University (1-4-1 Kagamiyama, Higashi-Hiroshima 739-8527 Japan)

1. Introduction

Fisheries production in the Seto Inland Sea which is largest enclosed sea in Japan decreased sharply during the last 30 years. One of the reasons for the decrease is thought to be the deterioration of marine sediments. Hydrogen sulfide in eutrophic marine sediments is highly toxic to benthic organisms and may cause foul odor and blue tide. Therefore, it is very important to monitor hydrogen sulfide in sediments to maintain healthy ecosystems and support sustainable fisheries.

The hydrogen sulfide concentration in eutrophic marine sediments is controlled by sulfur species in marine sediments as well as the activities of sulfate-reducing bacteria. In previous studies, the sulfur species in marine sediment was determined using a sequential extraction. However the conventional extraction method requires complicated procedure to separate and identify each sulfur species. Therefore, it is concern that sulfur species might change to different chemical forms as a result of the complicated procedure.

The purposes of this study were to (1) determine directly the hydrogen sulfide concentration in marine sediment pore water using a detection tube and (2) identify sulfur species in marine sediment using XAFS instead of the complicated sequential extraction method.

2. Materials and Methods

Sediment core samples were collected from 14 sampling stations in Osaka Bay in April, October and November, 2014 using an undisturbed core sampler (ø11 cm, 50 cm long: HR type; Rigo) deployed from Onokoro, a training and research vessel of the Research Center for Inland Seas, Kobe University. The collected cores were cut every 5 cm depth on board. The sediment pore water was collected by installing a soil moisture sampler (DIK-305A; Daiki Rika Kogyo) to the sediments and the concentration of hydrogen sulfide in the pore water was measured by the detection tube (200SA or 200SB: Komyo Rikagaku Kougyo). Oxidation and reduction potential (Eh) and pH were measured by inserting each electrode to the sediments (RM-30P; DKK-TOA, C-62; AS ONE). The collected sediments were vacuum-dried at 45°C and ground using an agate made mortar. The homogenized sediment samples were stored in vacuum packs to prevent oxidation before XAFS analyses. Vertical profiles such as temperature, pH, dissolved oxygen (DO) concentration and salinity of the water column at each sampling station were also measured using multi electrodes.

Sulfur K edge XAFS spectra (ranges 2460–2490 eV) of the sediments were measured using the BL11 in the Hiroshima Synchrotron Research Center, HiSOR [1]. The synchrotron radiation from a bending magnet was monochromatized with a Si(111) double-crystal monochromator. The sample chamber was filled with He gas, and XAFS spectra were measured by the X-ray fluorescence yield (XFY) mode using a SDD detector (XR-100SDD; AMPTEK). The X-ray energy around K edges of sulfur was calibrated with the spectra of $CuSO_4$ obtained with the CEY mode. The K edge main peak of sulfate was set to 2481.6 eV. The sediment samples were mounted on a double stick tape (NW-K15; Nichiban) placed in the central hole (15 mm in diameter) of a copper plate. The surface of the sample was attached to that of the copper plate. The angle between the incident X-ray and the sample surface was adjusted at 20°, and the X-ray fluorescence was detected from the direction normal to the incident beam in the plane of electron orbit of the storage ring. Concentrations of each sulfur species were calculated from total sulfur concentration proportionally divided by each sulfur species composition. Total sulfur concentration was determined by ICP-AES after wet oxidative decomposition.

3. Results and Discussion

The concentrations of hydrogen sulfide in sediment pore water ranged from <0.1 to 110 mg-S L^{-1}.

Sulfur species in marine sediments collected from Osaka Bay fitted well with the combination of sulfate, sulfite, thiosulfate, sulfur, cysteine and pyrite. Examples of the liner combination fit are shown in **Fig. 1**. The major sulfur species were (1) sulfate originating from seawater or oxidation of sulfur by sulfur bacteria [2], (2) sulfur formed by oxidation of hydrogen sulfide and (3) pyrite derived from (bio) mineralization. Cysteine, thiosulfate and sulfate were also identified as minor species. Cysteine was generated through sulfate reduction by the activity of the microorganisms. Thiosulfate and sulfite were mainly formed through the oxidation of hydrogen sulfide.

Concentrations of each sulfur species in marine sediments collected from station No.4 at Osaka Bay are also shown in **Fig. 2**. In the surface layer (depth of 0-5 cm), 65% of sulfur species were oxidative species such as sulfate, sulfite and thiosulfate. However these oxidative species decreased to 49.2, 30.1 and 38.5% at depths of 5-10, 10-15 and 15-20 cm layer, respectively. Since DO concentration and DO saturation of the overlaying water were 3.5 mg L^{-1} and 49%, respectively, the DO in the overlaying water might have remained to oxidize hydrogen sulfide. Therefore, most of the hydrogen sulfide was considered to be oxidized to sulfate by chemotrophic sulfur bacteria. In contrast, composition of sulfur and reductive species such as pyrite and cysteine increased, indicating that redox condition of the sediment at a depth of more than 5 cm was in reduced condition, especially the oxidation and reduction potential (Eh) of the sediments was -119 mV and at the depth of 15-20 cm.
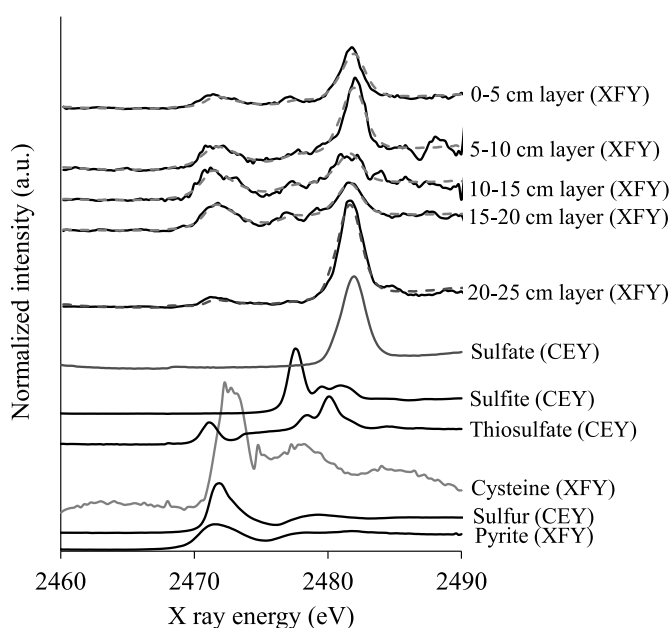

Fig. 1 Sulfur K edge XANES spectra of marine sediments collected from station No. 4 at Osaka Bay in October 2014.

Solid lines are observed spectra of standards or marine sediments. Dotted lines are liner combination fit of marine sediments by combination of standards.
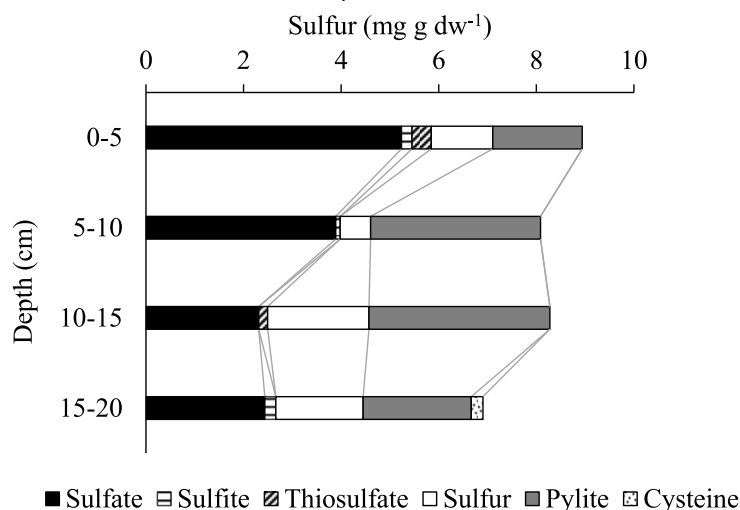

Fig. 2 Concentrations of each sulfur species in marine sediments collected from station No. 4 at Osaka Bay in October 2014.

4. Conclusion

Sulfur species in marine sediment could directly be identified using XAFS instead of the conventional sequential extraction method. Sulfur species in marine sediments collected from Osaka Bay fitted well with the combination of sulfate, sulfite, thiosulfate, sulfur, cysteine and pyrite.

References

1. Asaoka S., Hayakawa S., Kim K.H., Takeda K., Katayama M. and Yamamoto T, J. Colloid Interf. Sci. **377**, 284-290 (2012).
2. Van den Ende, F.P., Laverman, A.M. and van Gemerden, H., FEMS Microbio. Ecol. **19**, 141-151 (1996).

XAS study of hydrogenation properties of Pd-TM alloys

K. Fujii[a], N. Ishimatsu[a], S. Hayakawa[b], T. Shishidou[c], H. Maruyama[a]

[a]*Graduate School of Science , Hiroshima University, Higashihiroshima 739-8526, Japan*
[b]*Graduate School of Engineering, Hiroshima University, Higashihiroshima 739-8527, Japan*
[c]*Advanced Sciences of Matter (ADSM), Hiroshima University Higashihiroshima, 739-8530, Japan*

Keywords: X-ray absorption spectroscopy, Hydride, Pd-based alloys, Electronic structure

It is well known that hydrogenation of Pd metal occurs even at lower pressures than ambient pressure [1,2]. This property of Pd is of great interest, because the hydrogen pressure P_{H2} above 1 GPa is typically required for the hydrogenation of more than half filled $4d$ transition metals (TM) such as Ru and Rh. The excellent hydrogen absorbing property of Pd metal is modified by alloying with small amount of different transition metals. In the case of Pd-Rh alloys, P_{H2} rapidly increases with increasing Rh content [1]. On the other hand, P_{H2} of Pd-Ag alloys decreases with increasing Ag contents accompanied with a linear decrease in hydrogen content x [2].

The different trends of hydrogenation as a function of Rh or Ag content demonstrate that the hydrogenation properties are not simply interpreted as the effects of the change in the average number of $4d$ electrons. It is speculated that the hydrogen absorption property is influenced by the intrinsic hydrogen absorbing property of each constituent atom; however, it has not been fully understood how Rh and Ag atoms participate the hydrogenation of the Pd-TM alloys. In this study, we have investigated the element selective $4d$ electronic states of Pd-TM alloys (TM = Ru, Rh, and Ag) before and after hydrogenation by using x-ray absorption spectroscopy (XAS) at the TM $L_{2,3}$-edges.

Ingots of Pd-TM polycrystalline alloys were synthesized by arc melting method. The ingot was cut and formed into a disk 0.3mm in thickness by a low speed saw. The disk was hydrogenated under H_2 gas flowing at room temperature. X-ray diffraction measurement was performed in-situ to monitor a volume expansion during the hydrogenation process. The hydrogen content in the alloy was evaluated by using the linear relationship with the lattice constant [3].

XAS measurements were performed on BL-11 at HiSOR. In this study, the absorption spectra at both L_2 and L_3 edges were measured. The XAS spectra at the Pd $L_{2,3}$-edges were recorded using the conversion electron yield method. For the Rh and Ru $L_{2,3}$-edges and the Ag L_2-edge, X-ray partial fluorescence yield method was employed. The absorbance was measured under He gas flowing or 95%He+5%H$_2$ mixture gas flowing. We confirmed that the sample maintained more than 90% of the initial hydrogen content after the XAS measurements.

Figure 1 shows normalized X-ray absorption near edge structure (XANES) profiles at the $L_{2,3}$ edges of the Pd-TM alloys and the spectra after hydrogenation. The suppression of whiteline (peak A) and appearance of a new peak (peak B) were observed in each spectra of the hydrogenated alloys at the Pd, Ru and Rh L_3-edges. Same changes are observed at the TM L_2-edges. Because the intensity of whiteline is proportional to the number of $4d$ hole, the suppression of whiteline indicates that DOS of $4d$ band near the Fermi energy is additionally occupied after hydrogenation [4]. The peak B is attributed to the $4d$ orbital component in the anti-bonding state with the hydrogen atom. Accordingly, Pd, Ru and Rh atoms bonds to hydrogen atom in the Pd-M alloy, which is in contrast to the fact the hydrogen pressure P_{H2} above 1 GPa is required for the hydrogenation of Ru and Rh metals. As shown in Fig. 1, spectral differences between L_2- and L_3-edges are not large, so that the splitting at the $4d$ states due to the spin-orbit interaction is probably weak.

We observed shifts of the absorption edge E_0 due to hydrogenation. E_0 was estimated from the first inflection point of the XANES profile. E_0 of Pd moves to higher energy, whereas E_0 of Rh and Ru is

unchanged or moves slightly to the lower energy. Compared with the simulation of XANES spectra by first principles calculation, we found that the shift of E_0 is associated with the reconstruction of DOS after hydrogenation. In the case of Rh and Ru metals, high DOS above the E_F is reserved after hydrogenation, resulting in the steep raising edge near the whiteline of the Rh and Ru $L_{2,3}$-edges. On the other hand, because the E_F of Pd moves above the $4d$ DOS after hydrogenation, the low and uniform DOS above the E_F leads to the moderate slope of the rising edge of the Pd $L_{2,3}$ edges. This results gives rise to the remarkable shift of E_0. Our study has revealed that Rh-H and Ru-H bonds exist as well as the Pd-H bonds, whereas Ag-H bond is absent in the Pd-based hydrogenated alloy. The hydrogenation property of the Pd-based alloy is determined by reconstruction of the electronic states due to formation of each TM-H bonds.
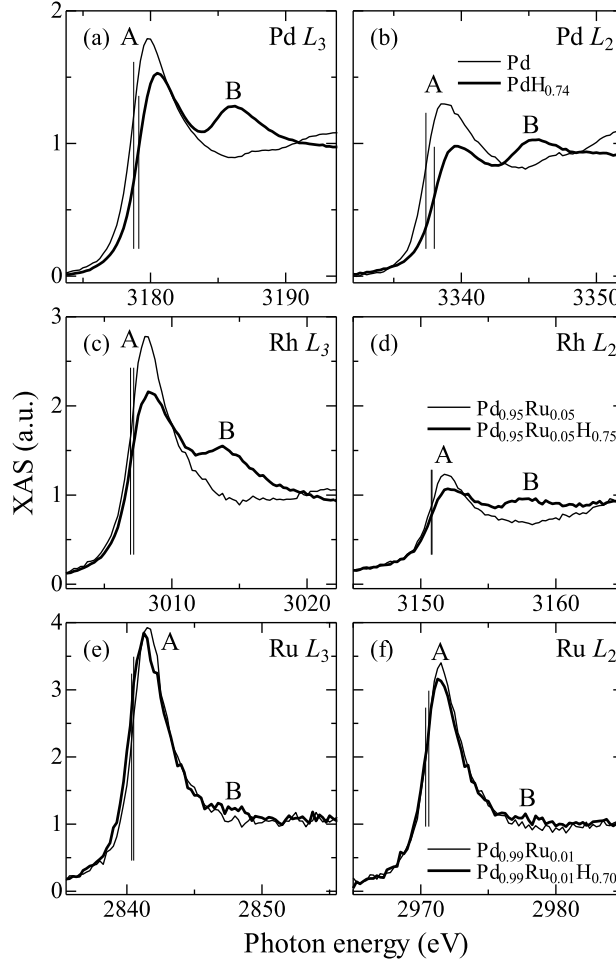
FIGURE 1: XANES profiles of Pd-M (M = Ru, Rh) alloy (thin lines) and the profiles after hydrogenation (thick lines) at the L_2 and L_3 edges. Vertical lines indicate position of the absorption edge E_0 of each spectrum.

REFERENCES

[1] S. Thiebaut *et al.*, J. Alloys Comp. **231**, 440 (1995).
[2] T. B. Flanagan, D. Wang, and S. Luo, J. Phys. Chem. B **111**, 10723 (2007).
[3] Y. Wang, *et al.*, Phys. Rev. B **53**, 1 (1996).
[4] D.A. Papaconstantopoulos *et al.*, Phys. Rev. B, **17**, 141 (1978).

An XAFS study on the local structural changes around titanium in the lithium secondary battery during the charge and discharge processes

Takuya Mori[a], Susumu Mineoi[b], Hirosuke Sumida[b], Yoji Yamada[b], Alvaro Munoz-Noval[a], Ayaka Tamua[a], Hirofumi Namatame[c] and Shinjiro Hayakawa[a]

[a] Department of Applied Chemistry, Graduate School of Engineering, Hiroshima University, Hiroshima, Japan
[b] Technical Research Center, Mazda Motor Co., Hiroshima, Japan
[c] Hiroshima Synchrotron Radiation Center, Hiroshima University, Hiroshima, Japan

Keywords: lithium titanium oxide, XAFS, Ti K-edge, FEFF

Introduction

Lithium titanium oxide (LTO), Li [$Li_{1/3}Ti_{5/3}$] O_2 , is an attractive anode material for lithium secondary battery (LSB). LTO has a defect spinel-framework structure (Fd-3m ; a = 0.836 nm), and the unit cell size was fixed during the following charge/discharge cycle [1].

$$Li[Li_{1/3}Ti_{5/3}]O_4 + Li^+ + e \leftrightarrow Li_2[Li_{1/3}Ti_{5/3}]O_4$$
8(a) 16(d) 32(e)   16(c) 16(d) 32(e)
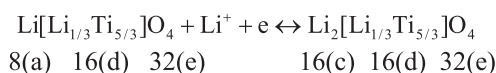
We have carried out *in-situ* Ti K-edge XAFS spectroscopy of LSB, and significant changes of Ti XANES spectra were observed during charge/discharge process [2]. Considering the fixed unit cell size spectral changes were attributed to the freedom of the oxygen position in 32(e) site. Utilizing the reported crystal structure [1] the spectral changes were simulated with FEFF8 code.

Experimental

XAFS measurements were performed on the BL-11 using a He filled chamber. The beamline was equipped with a Si(111) double crystal monochromator. A silicon drift detector (SDD) was placed in the orbit plane and the SDD was placed normal to the incident beam.

LSBs with fresh and depleted active materials were assembled into the *in-situ* cell reported previously [2], and the cell was placed inside the chamber. The charge/discharge was carried out with the commercial potentio-galvano-stat (Hokuto Denko, HAL3001) through the feed-through of the chamber. Ti K-edge XAFS spectra were successively measured during the charge/discharge process.

Results and Discussion

It was found the endurance test was not so sensitive to Ti XAFS spectra, and the similar spectral changes shown in Fig. 1 were observed during the charge/discharge process. According to the crystal models[1] oxygen position parameters (u) of 0.265 or 0.265 were used for crystal structures of before and after charge. The interpretations of the spectral changes will be discussed.
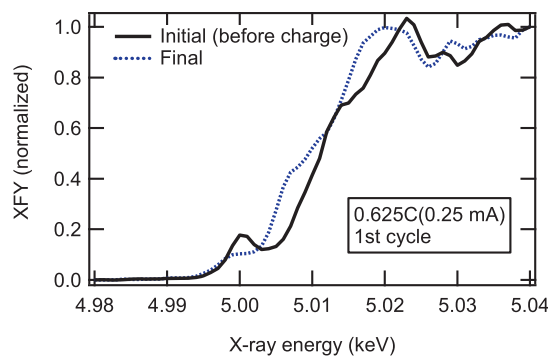

Fig.2. Ti K-edge XAFS spectra from LTO electrode during 0.65C charge.

References

1) T. Ohzuku, A. Ueda, N. Yamamoto, J. Electrochem. Soc., 142, 1431 (1995).

2) S. Hayakawa et al., HiSOR Activity report (2013).

Electrochemical formation of copper sulfide thin films and their characterizations

**Maki Yanase[a), Yusuke Hayasaka[a), Alvaro Munoz Noval[a), Ayaka Tamura[a),
Hirofumi Namatame[b) and Shinjiro Hayakawa[a)**

[a) *Department of Applied Chemistry, Graduates School of Engineering, Hiroshima University, Hiroshima, Japan*

[b) *Hiroshima Synchrotron Radiation Center, Hiroshima University, Hiroshima, Japan*

Keywords : copper sulfide, XAFS, sulfur K-edge, electrochemical formation

1. Introduction

Copper sulfide (Cu_xS) thin films have an appropriate optical band gap for solar cell, and the various attempts were made to control the optical properties of Cu_xS by the selective formation of the sulfide of desired composition selectively.

It was found the deposition of Cu_2S thin films could be controlled by applying an appropriate potential to the copper plate in the thiosulfate bath under the neutral condition [1]. We characterized the deposited thin films by XAFS, RBS (Rutherford back scattering) and LSV (Linear sweep voltammetry) [2], and the feasibilities of the electrochemical formation and the method of the characterization were evaluated.

2. Experimental

Copper sulfide thin films were deposited onto the copper plate in the thiosulfate baths. One was the solutions of 0.1 M $Na_2S_2O_3$ and 0.2 M $LiClO_4$, and the other contained additional 0.01 M $CuSO_4$ for the copper source. The pH of the solutions was adjusted to 5.2 with 0.2 M HCl solution. Electrochemical reaction was took place with the commercial potentiogalvanostat using a standard three electrode system. The reference electrode (RE) was Ag/AgCl and a counter electrode (CE) was a Pt plate. A copper plate of 1 $\times 1.5 cm^2$ was used as a working electrode (WE). The deposited samples were rinsed with the 1.0 M HCl solution and ultrapure water.

XAFS experiments were performed on the BL-11[3]. The beamline was equipped with a Si(111) double crystal monochromator. X-ray fluorescence yield (XFY) was monitored with a silicon drift detector (SDD).

LSV measurements were performed with the same potentiogalvanostat, but the samples were placed in the high alkaline solutions (6.0M KOH and 1.0M LiOH) according to the reported procedure [2].

3. Results and Discussion

Fig.1 a) shows a typical change of current during the deposition of a copper sulfide film in the thiosulfate bath. The applied potential to the WE was +4.6 mV. It was found that the current showed plateau until 100 s of reaction time, and it decreased gradually to zero. Samples were prepared with the reaction times of 60 s, 120 s and 600 s marked in Fig.1a), and S K-edge XAFS spectra were measured with the XFY mode (Fig.2).

Reference spectrum was obtained from powders of Cu_2S (P21/c). The initial spectrum showed less features, and the spectra gradually became similar to that of Cu_2S as the reaction time increased. The thickness of samples was determined by comparing XFY at 2.490keV with that of the reference sample. The thickness of the reference sample was determined to be 3.58nm by RBS. The thickness was 6.28 nm, 16.8 nm, and 15.4 nm for reaction times of 60s, 120s and 600s, respectively. It was found that the film was deposited during the period where the current showed plateau, and that the film was transformed into Cu_2S phase.

To control the film thickness of sulfide thin film, Cu^{2+} ions (0.01M $CuSO_4$) were added into the thiosulfate bath. The same potential (+4.6mV) was applied to the WE for 600 s, and the resultant change of the current was shown in Fig.1 b). The current remained longer than that in the simple thiosulfate bath, and the determined film thickness (17.9 nm) was greater than those obtained with the former conditions. The XAFS spectrum shown in Fig. 2d) was identical to those of Cu_2S phase, and the possibilities of controlling the film thickness and the composition of the sulfide[4] film may be indicated by changing the concentration of Cu^{2+} ions in the thiosulfate bath.
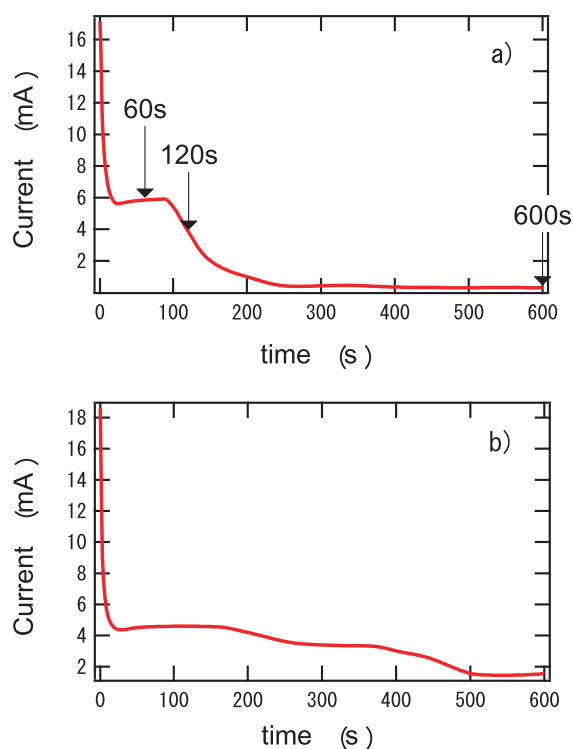
Fig.1. Change of current during the application of the potential of +4.6 mV.   a) in thiosulfate bath, and b) in thiosulfate bath including 0.01M $CuSO_4$.
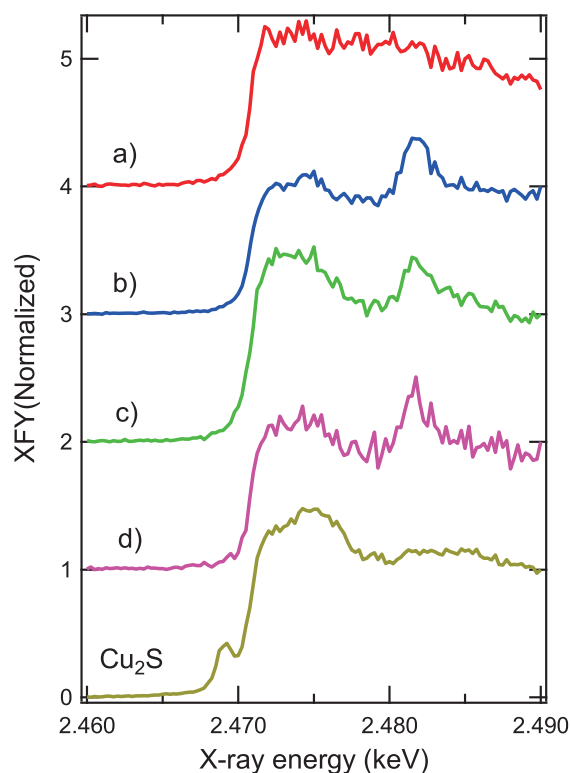
Fig.2. S K-edge XAFS spectra of deposited sulfide films. The reaction time was a) 60s, b) 120s, and c) 600s. d) is spectrum of the sample synthesized in the thiosulfate bath including 0.01M $CuSO_4$..

References

[1] S. Hayakawa et al., HiSOR Activity report 2015.

[2] S. Nakayama et al., Zairyo to Kankyo, 57, 327(2008)

[3] S. Hayakawa et al., Anal. Sci., 24, 835-837 (2008).

[4] Ivan Grozdanov, J. Solid State Chem., 114, 469-475(1995).

Qualitative and quantitative X-ray fluorescence analysis of light elements and trace fluorine using soft X-ray

Misa Kondo[a], Ayaka Tamura[a], Alvaro Munoz Noval[a],
Hirofumi Namatame[b] and Shinjiro Hayakawa[a]

a Department of Applied Chemistry, Graduate School of Engineering, Hiroshima University, Hiroshima, Japan
b Hiroshima Synchrotron Radiation Center, Hiroshima University, Hiroshima, Japan

Keywords : XRF, SDD with Si_3N_4 thin film window, light elements, fluorine

Introduction

X-ray emission analysis is an important tool for the determination of the elemental composition without the sample decomposition. Analysis of light elements has been widely carried out with the soft X-ray spectrometer attached to the electron microscope, and the energy dispersive detector equipped with an ultra-thin window was utilized under the vacuum condition. Recently commercial X-ray detectors with the ultra-thin window are available, and they can be utilized under the atmospheric pressure. We have introduced a new SDD (Silicon Drift Detector) to the end station of BL11 of the HiSOR. The detector has a 90 nm thick Si_3N_4 window, and the applicable elemental range may be expanded to light elements of C, N and O. The performance of X-ray fluorescence (XRF) analysis with the new SDD was investigated, and the qualitative and quantitative XRF analysis of light elements will be reported.

Experimental

Experiments were performed on the BL-11. The beamline was equipped with a Si(111) double crystal monochromator, and monochromatized X-rays from 2,1 to 5.9 keV were available. A sample was placed in a He filled chamber, and X-ray fluorescence from the sample was monitored with a SDD. Intensities of the incident beam were monitored with the air filled ionization chamber, and the XRF intensities were normalized with the beam intensities. The new SDD (FAST SDD, Amptek) was equipped with the 90 nm thick Si_3N_4 (C1) window, and the catalogued transmittance for O Kα (0.525 keV) was 29.4 %. The performance of the new detector was compared with the former SDD that has the same dimension of the effective area and equipped with the thin Be window of 13 μm.

A Kapton film of 12.5μm in thickness and a disk of quartz (SiO_2) were utilized as the reference materials of infinite thickness for the qualitative and quantitative analysis of C, N and O. A disk of calcium fluoride (CaF_2) and a series of polytetrafluoroethylene (PTFE) films deposited onto Ti or Cu substrates were utilized for the quantitative analysis of fluorine. A commercial canned spray (FC-107, Fine Chemical Japan Co., LTD) was utilized for the deposition of the PTFE films, and a unit thickness of the film was deposited by spraying chemicals 80 cm or 100 cm apart from the substrate for a period of 5 s or 2 s. The thickness of the film was varied by repeating the process from 1 to 5 times, and the sprayed films were fixed by heating at 473 K for 20 min in the oven.

Quantitative analysis was carried out by utilizing the theoretical equation of primary XRF, and fundamental parameters such as mass absorption coefficients and fluorescence yield were cited from the database.

Results and Discussion

Figure 1 shows the comparison of XRF spectra measured by two SDDs. The weight fraction of C, N and O in the Kapton film was expected to be 70, 7 and 20 wt. % respectively. It was clear that the signals from N and O were improved drastically with the new SDD.

Table 1 shows the comparison of the ratio of the XRF intensities in the sample between the theoritical and the experimental values. XRF intensities were calculated from the theoretical equation, and the geometrical factors were canceled by taking the ratio of intensities between the light element and the major composition. Theoretical intensities of O and F showed fairly good agreement with the theoretical values,

and the quantification of light elements might be carried out without the standard materials.

Figure 2 shows XRF spectra of PTFE films (100 cm series) deposited onto the Ti substrate. The background (Ti substrate) was subtracted for these spectra. Figure 3 shows a calibration curve of fluorine from a series of PTFE films. The calibration curve was linear within the range of the 100 cm series, and the absorption effects inside the film were negligible. The areal densities ($W_F \rho t$) of the unit coat of a 80 cm series and a 100 cm series were determined to be 9.2 μg/cm^2 and 1.0 μg/cm^2 by comparing the fluorine intensities with that from the CaF$_2$ disk. The detection limits (DL) of fluorine was derived from the single coat of 100 cm series. The DL of fluorine was 33 ng/cm^2, and the value was equivalent to the thickness of 0.20 nm if the film had the density of 2.2 g/cm^3.
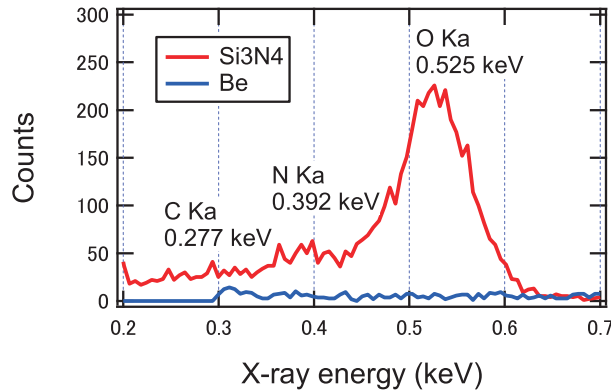
FIGURE 1 XRF spectra of a Kapton film obtained by the SDDs with the 13 μm Be window and the 90 nm Si$_3$N$_4$ window. The incident X-ray energy was 2.9 keV, and the data acquisition time was 1000 s.

TABLE 1. A comparison of ratios between X-ray fluorescence intensities from a sample between theoretical and experimental values. The data acquisition time was 1000 s.

Sample	Excitation energy (keV)	X-ray lines (A/B)	Theoretical ratio (I_A/I_B)	Experimental ratio (I_A/I_B)
SiO$_2$	2.9	O Kα / Si Kα+Kβ	0.6 %	0.5 %
CaF$_2$	4.1	F Kα / Ca Kα	0.2 %	0.1 %
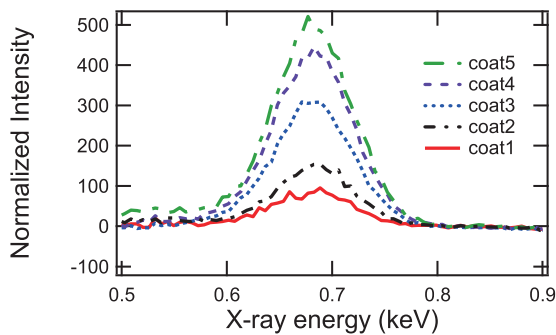
FIGURE 2. XRF spectra of PTFE films (100 cm series). The excitation X-ray was 2.9 keV, and the data acquisition time was 300 s.
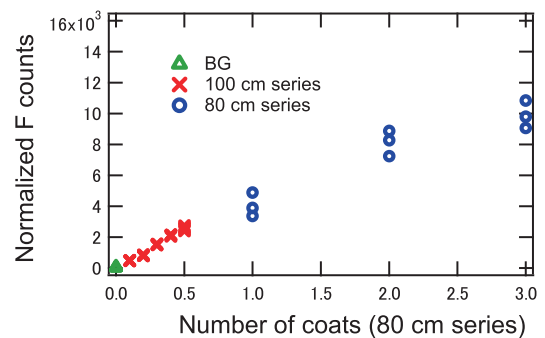

FIGURE 3. A calibration curve of fluorine in the PTFE films. The data acquisition time was 300 s.

Vacuum-Ultraviolet Circular-Dichroism Spectra of Polysaccharides and Cyclic Oligosaccharides

Koichi Matsuo, Hirofumi Namatame, and Masaki Taniguchi

Hiroshima Synchrotron Radiation Center, Hiroshima University, 2-313 Kagamiyama, Higashi-Hiroshima 739-0046, Japan

Vacuum-ultraviolet circular-dichroism (VUVCD) spectroscopy is a powerful technique for analyzing the structures of saccharides in aqueous solution because the saccharides contain hydroxy groups and acetal bonds whose high-energy $n-\sigma^*$ transitions are detectable only in the VUV region below 190 nm [1]. Previously, we measured the VUVCD spectra of linear oligosaccharides of maltose [2], isomaltose, and laminaribiose [3] which, respectively, have α-(1→4), α-(1→6), and β-(1→3) glycosidic linkages between glucose molecules, and we found that the CD of the oligosaccharides of maltose and laminaribiose are dependent on their chain lengths (or the degree of polymerizations). In the present study, to further investigate the contributions of chain length to CD, we measured the VUVCD spectra of α- and γ-cyclodextrin which are α-(1→4) linked cyclic oligosaccharides composed of six and eight glucose molecules, respectively, and dextran (Mw 4,400) and laminarin (Mw 7,700) [4] which are α-(1→6) and β-(1→3) linked polysaccharides, respectively, of glucose molecules.

Figure 1 shows the VUVCD spectra of α- and γ-cyclodextrin from 210 to 170 nm at 25°C in aqueous solutions. The spectra of linear oligosaccharides of six glucose molecules (maltopentaose) and of eight glucose molecules (maltooctaose) are depicted in this figure for comparison. The spectra of α- and γ-cyclodextrin exhibited positive CD at 170 nm, showing the large intensity in α-cyclodextrin compared to that in γ-cyclodextrin. On the other hand, maltopentaose and maltooctaose showed negative CD around 185 nm and positive CD at 170 nm, and the CD intensity in maltooctaose was lower than that of maltopentaose. These results mean that the contributions of chain length to the CD are very similar in the linear and cyclic oligosaccharides.
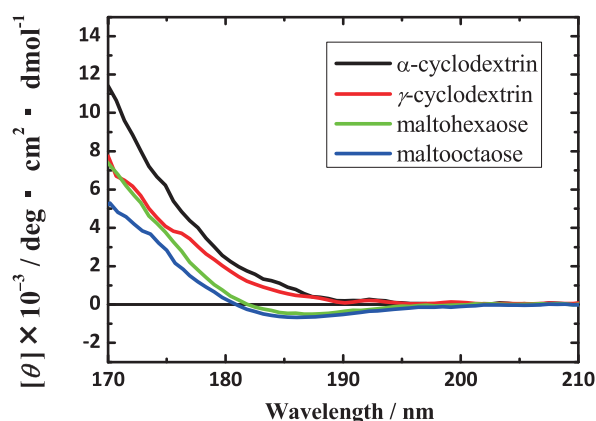

FIGURE 1. VUVCD spectra of two cyclic oligosaccharides and two linear oligosaccharides with α-(1→4) glycosidic linkages at 25°C in aqueous solution.

Figure 2 shows the VUVCD spectra of dextran and laminarin from 210 to 170 nm at 25ºC in aqueous solutions. The spectra of isomaltoheptaose and laminariheptaose which are α-(1→6) and β-(1→3) linked oligo-saccharides, respectively, with seven glucose molecules are also described in this figure for comparison. As shown in Figure 2, dextran and isomaltoheptaose showed similar CD spectra with positive intensity in the VUV region. Laminarin exhibited negative CD peak around 174 nm but the peak position was red-shifted to 177 nm and the peak intensity decreased in laminariheptaose. These chain-length dependence would be important for analyzing the conformation differences between polysaccharides and oligosaccharides in aqueous solution.
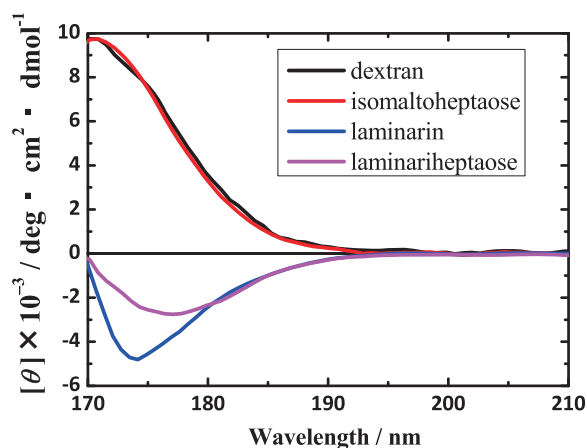
FIGURE 2. VUVCD spectra of two polysaccharides and two oligosaccharides with α-(1→6) and β-(1→3) glycosidic linkages at 25ºC in aqueous solution.

References

1. K. Matsuo and K. Gekko, *Carbohydr. Res*. 339, 591–597 (2004).
2. K. Matsuo, H. Namatame, and M. Taniguchi, *HiSOR Activity Report* **2011**, 163–164 (2011).
3. K. Matsuo, H. Namatame, and M. Taniguchi, *HiSOR Activity Report* **2013**, 127 (2013).
4. A. Mueller, J. Raptis, P. J. Rice, J. H. Kalbfleisch, R. D. Stout, H. E. Ensley, W. Browder, D. Williams, *Glycobiology* **10**, 339–346 (2000).

Effects of liposome surface charges on membrane-induced conformations of α_1-acid glycoprotein characterized by vacuum-ultraviolet circular-dichroism spectroscopy

Koichi Matsuo, Hirofumi Namatame, and Masaki Taniguchi

Hiroshima Synchrotron Radiation Center, Hiroshima University, Japan

α_1-Acid glycoprotein (AGP) exhibits some characteristic abilities to bind to numerous basic, acidic, and neutral drugs. However, the binding capacity of AGP for neutral drugs decreases due to its interaction with biomembranes, inducing a conformational change from a β-strand rich to an α-helix-rich structure (1, 2). Therefore, this conformational change of AGP coupled with the release of drugs into the membrane or cell is considered as a protein-mediated uptake mechanism of drugs.

It is known that the protein-membrane interaction is mainly caused by the electrostatic interactions between the negatively charged head groups of lipid molecules and the positively charged residues of the protein, and by the insertion of some hydrophobic groups of the protein into the membrane (2). In this study, to clarify the role of electrostatic interaction between AGP and membrane, the vacuum-ultraviolet circular-dichroism spectra of AGP were measured in the presence of the dimyristoyl phosphatidylglycerol (DMPG), dimyristoyl phosphatidic acid (DMPA), and dimyristoyl phosphatidylcholine (DMPC) liposomes at pH 4.5.
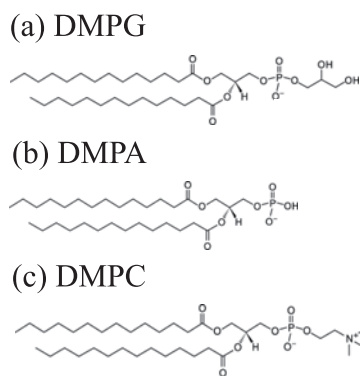
(a) DMPG

(b) DMPA

(c) DMPC

Figure 1 Chemical structures of three lipid molecules used in this study.
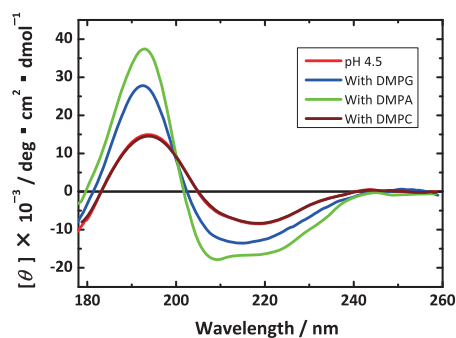

Figure 2. VUVCD spectra of AGP at pH 4.5 and in the presence of DMPG, DMPA, and DMPC liposomes.

Figure 1 shows the chemical structures of three lipid molecules (DMPG, DMPA, and DMPC). We can see that these head groups have neutral glycerol in PG and positively charged choline in PC, in addition to the negatively charged phosphate acid. Figure 2 shows the VUVCD spectra of AGP at pH 4.5 and in the presence of DMPG, DMPA, and DMPC liposomes. AGP at pH 4.5 without liposome and with DMPC showed similar VUVCD spectra, suggesting there are no structural change due to the interaction with DMPC whose head group charge is neutral (Figure 1(c)). However, DMPA-bound states of AGP exhibited large spectral change and further the AGP interacted with DMPG (a glycerol is added to the head group of DMPA) liposome transformed to the α-helix rich spectrum. These results indicate that the negatively charged head group is necessary for the membrane interaction of AGP.

References

1. K. Nishi, T. Maruyama, H. B. Halsall, T. Handa, M. Otagiri, *Biochemistry* **2004**, 43, 10513.
2. K. Matsuo, H. Namatame, M. Taniguchi, K. Gekko, *Biochemistry*, **2009**, 48, 9103.

Synergistic Gelation of Xanthan and Locust Bean Gum Studied by Vacuum-Ultraviolet Circular Dichroism

Yasuyuki Maki[a], Kazushi Toriba[a], Kazuya Ishizaka[a], and Koichi Matsuo[b]

[a]Division of Molecular Science, Graduate School of Science and Technology, Gunma University, Kiryu 376-8515
[b]Hiroshima Synchrotron Radiation Center, Hiroshima University, Higashi-Hiroshia 739-8526

Keywords: synergistic effect, mixed gel, polysaccharides, vacuum ultraviolet circular dichroism

A range of proteins, polysaccharides and their mixtures are employed as gelling agents by the food industry. In many cases, gelation of these food macromolecules is accompanied by conformational transition of macromolecules, which is induced by temperature, pressure, pH, etc. Vacuum-ultraviolet circular dichroism (VUVCD) is an effective tool for assignment of structures and conformational change of polysaccharides and proteins [1]. Gels used in foodstuffs are usually multi-component systems such as mixtures of proteins and polysaccharides. In some cases, the mixed gels show a synergistic effect, that is, enhanced rheological properties at a certain mixing ratio holding the total polymer concentration constant or gelation at concentrations below the gelation concentration of pure components. The synergistic effect is applied to gelling agents used in food industries.

Xanthan is the extracellular polysaccharide secreted by the bacterium *Xanthomonas campestris*. The primary structure of xanthan has been shown to consist of a cellulosic backbone substituted at C-3 on alternate glucose residues with a trisaccharide sidechain. The non-carbohydrate subchains include O-acetate on the inner mannose residue and pyruvate on the terminal mannose residue. Xanthan forms a five-fold double helical structure and is soluble in water. Aqueous solutions of xanthan are thixotropic, but do not form hard gels [2]. Galactomannans are extracted from the endosperms of legume seeds and are composed of a (1→4) linked β-D-mannan backbone partially substituted at C-6 with α-D-galactosyl residues. Galactomannans are water-soluble and do not form gels [2]. It has been known a mixture of xanthan and galactomannan forms a thermoreversible gel at concentrations where each pure component does not form a gel (synergistic effect). The observation that experimental conditions favoring denaturation of the xanthan helix promote the synergistic gelation has supported a concept of an intermolecular binding between the disordered xanthan backbone and the galactomannan, but the structure of the junction zones has not been clarified [2]. This study is aimed at clarifying the conformation of two polysaccharides in a mixed solution of xanthan and galactomannan before and after the gelation by use of VUVCD spectroscopy.

Xanthan was provided by CP Kelco Japan ApS. Locust bean gum provided by CP Kelco Japan ApS ($M_v \sim 1 \times 10^6$) was used as a galactomannan sample. Xanthan and galactomannan were dissolved in 10 mM NaF solution at the concentration of 1.0 wt% and a mixed solution was obtained by mixing of the two solutions at the ratio of 1:1. The VUVCD spectra of the mixture were measured from 245 nm to 186 nm under a nitrogen atmosphere by use of the VUVCD spectrophotometer constructed at Hiroshima Synchrotron Radiation Center (BL-12) and an assembled-type optical cell. The path length of the cell was adjusted with a Teflon spacer to 100 μm [1, 3].

The mixture of xanthan and galactomannan was thixotropic liquid at 25 °C, but after the thermal treatment at 80 °C for 15 min, it forms a hard gel at 25 °C, which indicated that the synergistic gelation is promoted by the denaturation of the xanthan helix.

Figure 1 shows the VUVCD spectra of the mixture obtained at 25 °C before the thermal treatment, at 80 °C during the thermal treatment, and at 25 °C after the thermal treatment. The spectrum at 25 °C before heating showed a strong positive peak and a weak negative peak at ~ 200 nm and at ~ 220 nm, respectively, indicating the double helix formation of xanthan [4]. Because the VUVCD spectrum of a galactomannan solution measured in previous studies had a positive peak at 179 nm and had no peak at > 185 nm [5,6], the effect of galactomannan on the spectrum may not be clear in the present wavelength range. In the spectrum at 80 °C during heating, the positive peak at ~ 200 nm became much weaker, indicating the denaturation of the xanthan helix. The spectrum at 25 °C after heating was almost the same with that before heating as if the renaturation of

the xanthan helix occurred and no new peaks for the intermolecular binding between xanthan and galactomannan were observed, although the mixture gelled after the thermal treatment. This result suggested that xanthan forms a heterotypical double helix with galactomannan [7] in which the secondary structure of xanthan is almost the same with that in the native double helix of xanthan and the hard gel formation is induced by this heterotypical double helices as junction zones of the synergistic gel.
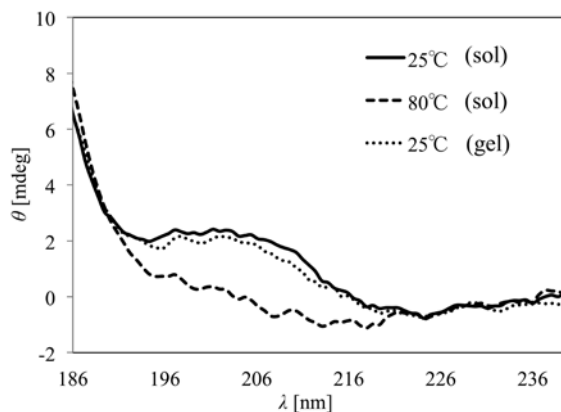
FIGURE 1. VUVCD spectra of the mixture of xanthan and galactomannan obtained at 25 ^{o}C before the thermal treatment (solid line), at 80 ^{o}C during the thermal treatment (dashed line), and at 25 ^{o}C after the thermal treatment (dotted line).

REFERENCES

1. N. Ojima, K. Sakai, K. Matsuo, T. Matsui, T. Fukazawa, H. Namatame, M. Taniguchi and K. Gekko, Chem. Lett. 30, 522 (2001).
2. V. J. Morris, "Gelation of Polysaccharides" in Functional Properties of Food Macromolecules, 2nd edition, edited by S. E. Hill, D. A. Ledward and J. R. Mitchell, Gaithersburg: Aspen Publishers, Inc., 1998.
3. K. Matsuo, K. Sakai, Y. Matsushima, T. Fukuyama and K. Gekko, Anal. Sci. 19, 129 (2003).
4. Y. Matsuda, Y. Biyajima and T. Sato, Polym. J. 41, 526 (2009).
5. Y. Maki, S. Yasuraoka, K. Toriba and K. Matsuo, HiSOR Activity Report 2013.
6. Y. Maki, K. Toriba, K. Ishizaka, H. Yoshida, S. Yasuraoka and K. Matsuo, HiSOR Activity Report 2014.
7. T. M. B. Bresolin, M. Milas, M. Rinaudo and J. L. M. S. Ganter, Int. J. Biol. Macromol. 23, 263 (1998).

VUV-CD Measurements of Proteins Relating to DNA Repair

Yudai Izumi[a], Kentaro Fujii[a], Satoshi Yamamoto[b], Koichi Matsuo[c], Akinari Yokoya[a,b]

[a]*Quantum Beam Science Center, Japan Atomic Energy Agency (JAEA), Ibaraki 319-1195, Japan*
[b]*Graduate School of Science and Engineering, Ibaraki University, Ibaraki 310-0056, Japan*
cHiroshima Synchrotron Radiation Center, Hiroshima University, Hiroshima 739-0046, Japan

Keywords: histone, post-translational modification, DNA damage responses

DNA wraps around core histone proteins composed of several subunits, named as H2A, H2B, H3, and H4, in eukaryotic nuclei. DNA damage may cause alterations of the genetic codes. Living organisms have evolved the system to detect and repair DNA damage. It is known that the chemical modifications of histone proteins play important roles in DNA repair processes [1]. However, the dynamics of histone during DNA damage repair processes are not explained completely. Recently, we observed relative increment of α-helix structure of histone H2A-H2B induced by X-ray irradiation to human cells using circular dichroism (CD) spectroscopy [2]. In an attempt to examine secondary structural change of histone H3-H4, we measured vacuum ultraviolet CD (VUV-CD) spectra of H3-H4 extracted from X-irradiated and unirradiated human cells.

HeLa.S-FUCCI cells were cultured in several culture dishes (*ca.* 1×10^7 cells/dish). The cells in culture dishes were irradiated with 40 Gy X-rays. After irradiation, the cells were incubated at 37°C in a humidified atmosphere of 5% CO_2 and 95% air for 30 minutes to progress DNA repair pathway. Histone H3-H4 was extracted from X-irradiated or unirradiated cells using Histone Purification Kit (Active Motif) and dissolved with 10 mM Tris-HCl buffer (pH = 8.0) and 250 mM NaF. VUV-CD measurements were carried out at BL-12 of HiSOR [3]. The samples were kept at room temperature during the VUV-CDmeasurements.

Figure 1 shows VUV-CD spectra of irradiated and unirradiated samples. Both spectra show three CD peaks at around 190, 208, and 222 nm. Those peaks are characteristic CD peaks of α-helix structure. It shows that the main structure of H3-H4 is α-helix. Apparent decrement of CD intensity was observed at around 190 nm. This result suggests that decrement of α-helix structure component was induced by X-ray irradiation to human cells. This is an opposite of structural change observed in H2A-H2B [2]. To date, the precise mechanism of histone structural alteration in response to X-ray irradiation has not been identified yet. A possible mechanism could be via post-translational modifications which are known to occur in histones during DNA damage repair processes [1]. Cyclopedic VUV-CD spectroscopy of specific modified-histones to understand the alteration mechanism of histone structures and its contribution to DNA repair processes is warranted for future studies.
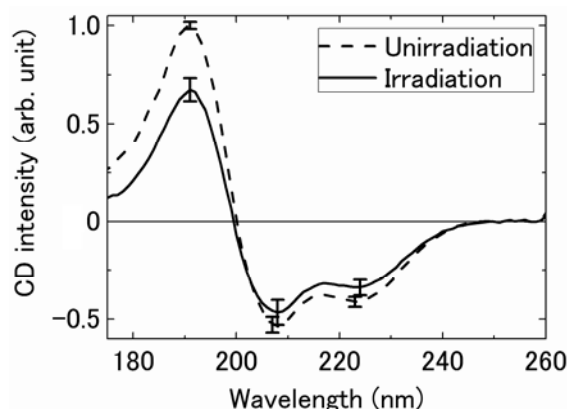

FIGURE 1. VUV-CD spectra of histone H3-H4 extracted from unirradiated and X-irradiated cells with partial error bars.

REFERENCES

[1] C. R. Hunt *et al.*, *Radiat. Res.* **179**, 383-392 (2013). [2] Y. Izumi *et al.*, *Radiat. Res.* **184**, 554-558 (2015).
[3] M. Sawada *et al.*, *J. Phys : Conf. Ser.* **425**, 162010 (2013).

Contributions of Aromatic Side Chains to the Vacuum-Ultraviolet Circular Dichroism Spectra of *Escherichia coli* Dihydrofolate Reductase

Suguru Tanaka[a], Eiji Ohmae[a], Yurina Miyashita[a], Koichi Matsuo[b], and Katsuo Katayanagi[a]

[a]*Department of Mathematical and Life Sciences, Graduate School of Science, Hiroshima University, 1-3-1, Kagamiyama, Higashi-Hiroshima 739-8526, JAPAN*
[b]*Hiroshima Synchrotron Radiation Center, Hiroshima University, 2-313, Kagamiyama, Higashi-Hiroshima, 739-0046 JAPAN*

Vacuum-ultraviolet (VUV) circular dichroism (CD) spectroscopy using a synchrotron radiation can predict the secondary structure contents of proteins more accurately than conventional CD spectroscopy and hence is becoming more important in protein structural biology [1]. The CD spectra of proteins are influenced by aromatic side chains, but there are only limited information on their contributions to the CD spectra in the VUV region. In the present study, we measured VUV CD spectra of *Escherichia coli* dihydrofolate reductase (DHFR, Fig. 1) mutants relevant to six phenylalanine, four tyrosine, and five tryptophan residues down to 175 nm to elucidate the contributions of these side chains to the high energy transitions of peptide bonds.

Figure 2 shows VUV CD spectra of the wild-type and several mutant DHFRs. The VUV CD spectrum of DHFR was obviously affected by single amino acid substitution from phenylalanine, tyrosine, and tryptophan to leucine. The VUV CD spectra of the other mutant DHFRs were also affected by the mutation. These results clearly indicated that the aromatic side chains contributed to the CD spectrum of DHFR in the far-UV and VUV regions.
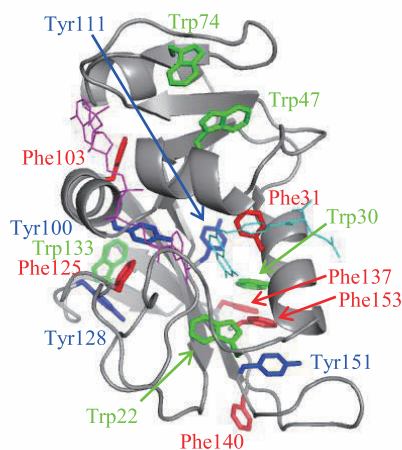

FIGURE 1. Backbone cartoon drawing of the DHFR-NADP$^+$-folate ternary complex (PDB code: 1rx2) [2]. NADP$^+$ (magenta) and folate (cyan) are shown as line models. The six phenylalanine, four tyrosine, and five tryptophan side chains are drawn as stick models with labels and are colored red, blue, and green, respectively. This figure was drawn using the program Pymol (http://www.pymol.org/).
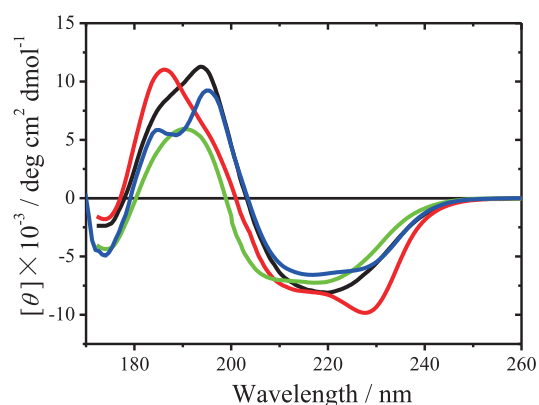
FIGURE 2. VUV CD spectra of the wild-type (black), F103L (red), Y100L (blue) and W47L (green) DHFRs at 25 °C. The buffer used was 20 mM Tris-HCl (pH 8.0) except for the measurement of W47L mutant, in which 10 mM potassium phosphate (pH 7.0) was used. Both buffers contained 0.1 mM EDTA and 0.1 mM dithiothreitol. Protein concentration was 350-400 μM.

Particularly, F103L mutant showed significantly different CD spectrum from other mutants, both the positive and negative peaks were 8 nm blue- and red-shifted, respectively, from those of the wild-type DHFR. This characteristic spectrum is ascribed to modifications of exciton coupling between the Trp47 and Trp74 side chains [3] because similar far-UV CD spectra were observed previously for Met42 DHFR mutants in which exciton coupling was modified [4]. Since it was known that the CD spectrum of M42I DHFR returned to the shape like the wild-type DHFR, we measured the folate and NADP$^+$ concentration-dependences of the far-UV CD spectrum of the F103L mutant. The negative peak intensity of the spectrum at 228 nm had clearly decreased and the intensities around 218 nm were increased in the opposite direction by the addition of folate or NADP$^+$. The calculated dissociation constants, K_d, from the molar ellipticity change at 230 nm for folate and NADP$^+$ were 23 ± 3 and 30 ± 3 μM, respectively (Fig. 3). These results clearly indicate that exciton coupling of Trp47 and Trp74 side chains was modified by the F103L mutation and the addition of folate or NADP$^+$ enabled these tryptophan side chains to adopt an orientation that is similar to that of the wild-type protein.

A matter of concern is whether the ligand concentration-dependent spectral change is observed in the VUV region of the CD spectrum of the F103L mutant. To clarify this point, we measured the VUV CD spectra of the F103L-folate and F103L-NADP$^+$ binary complexes. As shown in Fig. 4A, the VUV region of the CD spectrum of the F103L mutant clearly changed after the addition of folate. The positive peak at 186 nm decreased in intensity and the ellipticities around 195 nm, which match the positive peak of wild-type DHFR, increased as the concentration of folate increased with an isoelliptic point at 192 nm. Similar results were also observed for the F103L-NADP$^+$ complex, with the isoelliptic point shifted to approximately 190 nm (Fig. 4B). The inset of Fig. 4 shows the VUV CD difference spectra of the F103L mutant with or without ligands. The molar ellipticity changes for the positive and negative peaks at 199 and 184 nm in the difference spectrum were similar and proportional to the population of the F103L-ligand binary complexes calculated from the K_d values, indicating that the spectral change reflect the contribution of the exciton coupling.

The results of this study clearly demonstrate that the aromatic side chains and the exciton coupling of two tryptophan side chains have significant contributions to the CD spectrum of DHFR in the VUV region.
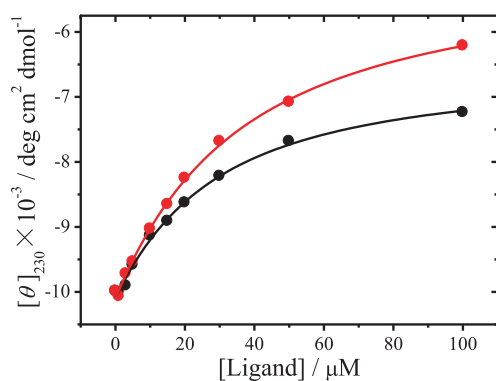

FIGURE 3. Ligand concentration-dependencies of molar ellipticity at 230 nm of the F103L mutant DHFR at 25 °C and pH 8.0. The black and red circles indicate folate and NADP$^+$, respectively. The lines indicate the least-squares fits to the equation derived from the one-to-one binding model.
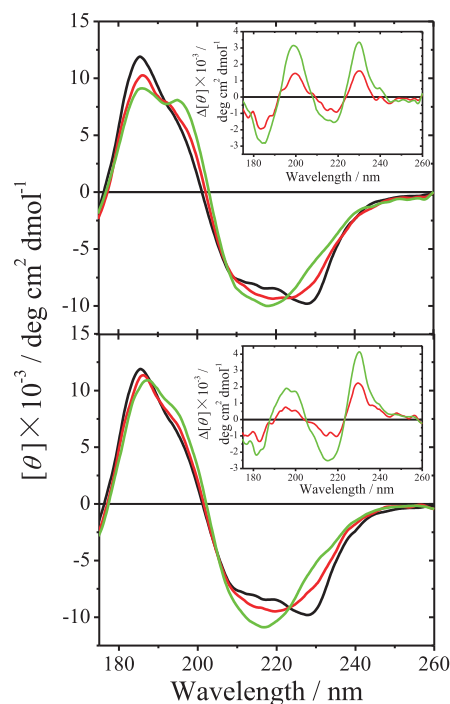

FIGURE 4. Folate (A) and NADP$^+$ (B) concentration-dependencies of the VUV CD spectrum of F103L mutant DHFR at 25 °C and pH 8.0. The protein concentration was 770 μM. Ligand concentrations were 0 (black), 400 (red), and 880 (green) μM. Insets show VUV CD difference spectra with or without folate (A) or NADP$^+$ (B).

REFERENCES

1. K. Matsuo, R. Yonehara, and K. Gekko, *J. Biochem*. **138**, 79-88 (2005).
2. M. R. Sawaya and J. Kraut, *Biochemistry* **36**, 586-603 (1997).
3. K. Kuwajima, E. P. Garvey, B. E. Finn, C. R. Mathews, and S. Sugai, *Biochemistry* **30**, 7693-7703 (1991).
4. E. Ohmae, Y. Fukumizu, M. Iwakura, and K. Gekko, *J. Biochem.***137**, 643-652 (2005).

Characterization of green fluorescent protein monolayers utilizing controllable self-assembled monolayers

Shin-ichi Wada[a,b], Jumpei Kajikawa[a], Hironori Hayashita[a], Ryosuke Koga[a], and Atsunari Hiraya[a,b]

[a] *Department of Physical Science, Hiroshima University, Higashi-Hiroshima 739-8526, Japan*
[b] *Hiroshima Synchrotron Radiation Center, Hiroshima University, Higashi-Hiroshima 739-0046, Japan*

It is important to understand the function and interaction of proteins immobilized onto surfaces in order to not only conveniently investigate characteristics of proteins but also realize ideal protein monolayers for applications like biosensors, biotips, immunosensors and molecular electronic devices. In introducing proteins onto surfaces, however, they often lose their original functions by means of conventional methods. Immobilization of proteins without any damage is quite important issue on this fields.

Self-assembled monolayers (SAMs) have attractive potential as one of promising candidate surfaces on which proteins can be introduced as they are. Because it is expected that one can introduce proteins onto surfaces nondestructively by inserting the soft organic monolayers between hard metal substrates and soft proteins. Moreover, if SAMs with functional groups which can specifically interact with proteins are used, we can easily immobilize proteins on surfaces. By contrast, if non-specific functional groups are utilized, we can control the amount of adsorption of proteins on the surfaces. In this study, protein layers formed on SAMs were evaluated using green fluorescent protein (GFP) by means of optical emission, x-ray photoelectron spectroscopy (XPS) and near edge x-ray absorption fine structure (NEXAFS) measurements.

Optical emission measurements were carried out by using a photoluminescence spectrometer of Natural Science Center for Basic Research and Development in Hiroshima University. From the optical emission measurements, we could easily check the function of GFP and evaluate the amount of adsorption. Orientation of GFP on SAMs was examined by NEXAFS spectroscopy. The NEXAFS and XPS measurements were performed at BL13 of HiSOR. SAMs were prepared by immersing gold coated substrates to 1mM ethanol solutions of SAM forming thiols, and GFP monolayers were prepared by dropping GFP aqueous solutions on the SAMs.

Figure 1 shows N and O K-edges NEXAFS spectra of the GFP monolayer on COOH SAM $(Au/S(CH_2)_{10}COOH)$ measured at the incident angles of 20 and 90 degrees from the surface. The only first sharp peaks at the both K-edges, which correspond to the N/O(peptide) 1s to the π^* transitions, show clear incident angle dependence [1-3]. This incident angle dependence describes that GFP forms oriented monolayer on the SAM. The analytical formula of the angular dependence of NEXAFS resonances in molecular adsorption systems is described in Ref. 4. By using a natural structure of GFP, in which about 60% of 237 peptides exist on β sheets surrounding the protein molecule, and the relationship between incident angle and resonant intensity, the axis of a GFP can be estimated to 73 degrees tilting from the surface normal as shown in Figure 2(a). It is quite important that incident angle dependence appears and the orientation was evaluated even for huge molecular system like GFP. GFP molecule can also adsorb and orient on ethylene glycol (EG) containing thiol SAMs (EG6-COOH SAM; $Au/S(CH_2)_{11}(EG)_6OCH_2COOH$). Although oligo-EG has a characteristics to prevent non-specific adsorption of proteins, like hydrophobic interaction and hydrogen bonding, GFP on EG6-COOH SAM also indicate oriented adsorption with a similar orientation angle of 79 degrees (Figure 2(b)). Both COOH SAMs were activated by NHS reagent to form peptide bonding in preparing GFP monolayers on SAMs. Figure 3 shows typical population maps of amino group-containing amino acids like lysine, arginine, and histidine,

indicating major population on β barrel, and it is reasonable that COOH-SAMs can make peptide bonds with such amino-acid residue(s) and forms almost flat lying conformation with tilting angle of about 75 degree.

REFERENCES

1. Y. Bai, X. Liu, P. Cook, N.L. Abbott, and F.J. Himpsel, Langmuir 26 (2010) 6464-6470.
2 M.L. Gordon, G. Cooper, C. Morin, T. Araki, C.C. Turci, K. Kaznatcheev, and A.P. Hitchcock, J. Phys. Chem. A 107 (2003) 6144-6159.
3 Y. Bai, X. Liu, P. Cook, N.L. Abbott, and F.J. Himpsel, Langmuir 22 (2006) 7719-7725.
4 J. Stöhr, NEXAFS Spectroscopy, Springer-Verlag: New York, 1992.
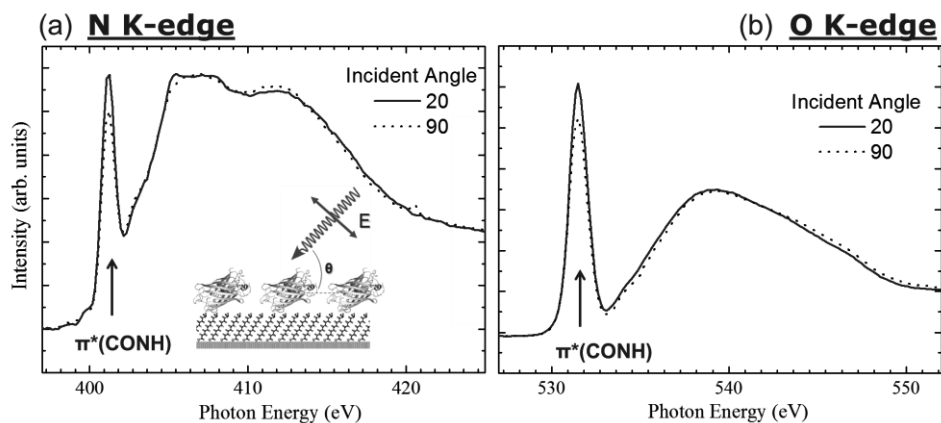
FIGURE 1. Typical NEXAFS spectra for GFP monolayers immobilized on COOH SAM measured in (a) the nitrogen and (b) oxygen K edges.
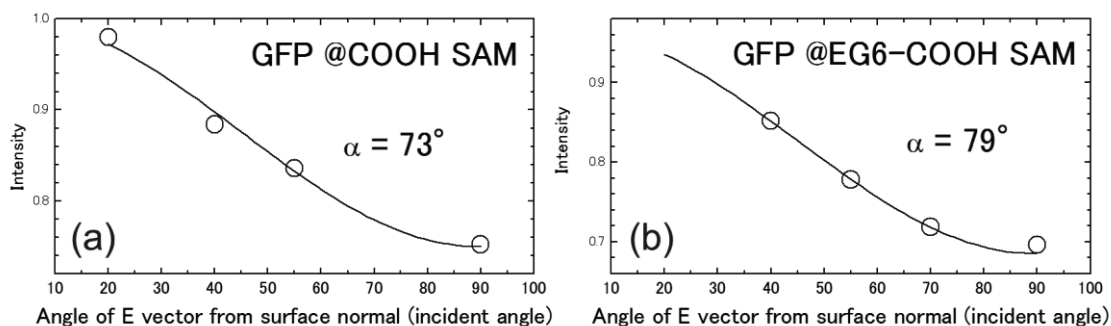
FIGURE 2. Polarization dependence of GFP immobilized on (a) COOH SAM and (b) EG6-COOH SAM. The dependence was derived from first π* peaks of O K-edge NEXAFS spectra.
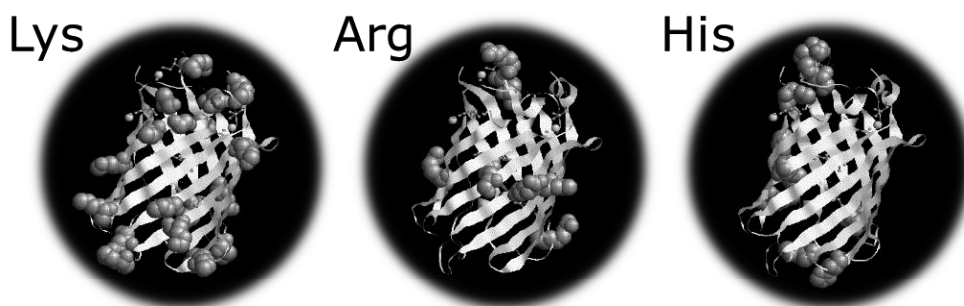

FIGURE 3. Population of amino-acid residues of GFP, lysine, arginine, and histidine.

Non-contact evaluation of molecular conductivity of organic molecules utilizing core-excitation dynamics measurements

Shin-ichi Wada[a,b], Mai Ogawa[a], Syunki Hosoda[a],
Ryosuke Koga[a], and Atsunari Hiraya[a,b]

[a] *Department of Physical Science, Hiroshima University,*
Higashi-Hiroshima 739-8526, Japan
[b] *Hiroshima Synchrotron Radiation Center, Hiroshima University,*
Higashi-Hiroshima 739-0046, Japan

Charge transfer dynamics at organic interfaces has attractive potential for future applications based on organic molecular devices. We consider that such dynamics can be evaluated by "site-selective ion desorption" characterized by resonant core-excitations. Site-selective ion desorption is a quite unique reaction after resonant core-electron excitation [1]. It is generally understood that selective ion desorption is promoted by the Coulomb repulsion between two holes at local bonding orbital(s) and the suppression of bonding power due to one electron at an anti-bonding orbital (so-called spectator Auger final state). This reaction can be obviously observed on solid surfaces, particularly well-ordered monolayers, like self-assembled monolayers (SAMs). This indicates the importance of the interaction between functional group at outermost surface (reaction center) and substrate [1]. In this study, we investigated the relationship between site-selective ion desorption and charge transfer dynamics.

We applied near edge x-ray absorption fine structure (NEXAFS) spectroscopy and time-of-flight mass spectroscopy (TOF-MS) to investigate ion desorption, and core-hole-clock (CHC) method to investigate ultrafast charge transfer processes. CHC is powerful technique to measure ultrafast charge transfer. Generally, resonant Auger decay only occur after a resonant core excitation. But normal Auger electron can be also observed in solid surfaces. This is caused by fast dissipation of the excited electron to conductive band of the substrate before core-hole decay. So, we can get information about charge transfer dynamics from branching ratio between resonant Auger yield and normal Auger yield in comparison with the core-hole lifetime [2,3].

NEXAFS and resonant Auger electron spectrum (RAES) measurements were performed at the beamline BL-13 of HiSOR. During measurements, the experimental chamber had a base pressure of 2×10^{-9} Torr. NEXAFS around the C and O K edges was recorded in total electron yield (TEY) mode by measuring a sample drain current. RAES were measured using a concentric hemispherical analyzer (Omicron EA125U5) by changing photon energy of irradiation light in the O1s region. Partial ion yield (PIY) measurements were carried out at the beamline BL7A of PF during single-bunch operation. PIY spectra were measured by detecting selected ions using a TOF mass spectrometer. SAMs were prepared by immersing Au substrates into 1.0 mM ethanol solutions of MHDA ($HS(CH_2)_{15}COOCH_3$), MP0 ($HSPhCOOCH_3$), MP1 ($HSCH_2PhCOOCH_3$) and M2P ($HSPhPhCOOCH_3$). Fig. 1 shows schematic drawings for SAMs used in this experiments. All samples have $-COOCH_3$ at their head groups, connected by phenyl ring(s) with conductivity for MP0, MP1 and M2P SAMs, while MHDA has not conductivity due to insulating aliphatic methylene chain.

Fig. 2 shows O1s NEXAFS and Auger electron yield spectra. Total Auger yields are proportional to NEXAFS spectra. On the other hand, resonant (spectator) Auger components are strongly reduced after 534 eV. It indicates that ultrafast charge transfer occurs in this energy region. The resonant Auger yield of MP0 is more reduced than that of M2P. This result shows that the charge transfer at MP0 is about two times faster than M2P.
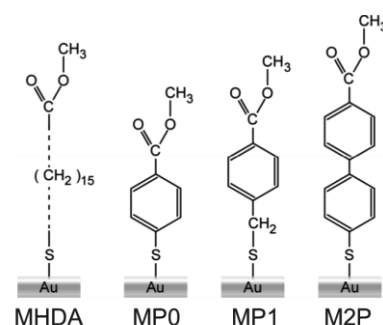

FIGURE 1. Molecular structure of SAMs used in this study, MHDA (insulating), MP0, MP1, and M2P (conductive).

Site-selective ion desorption takes place for both methyl-ester SAMs as a specific desorption of CH_n^+ (n=0-3) ions at C1s → σ*(O-CH₃) excitation, but accompanying with different branching ratio of CH_n^+. That is to say, CH_3^+ ion in desorbing causes higher fragmentation for MP0 than that for M2P, and it is considered that non-selective ion desorption for MP0 is strongly reduced by fast charge transfer process [1]. Form these results, there is the critical relationship between site-selective ion desorption and ultrafast charge transfer dynamics. So, site-selective ion desorption measurement is a useful candidate to evaluate molecular conductivity.

In order to understand the reaction dynamics of site-selective bond breaking accompanied by such fragmentation, ion yield ratio was reproduced under statistical considerations using only one parameter, an available energy E_{avail} (see Fig. 3). In this situation, only quantum state-counting is required since the statistical expectation is to populate every energetically allowed product states with a probability proportional to the number of such states, which are permitted by energy conservation. Using this definition of the statistical distribution, the problem is reduced to calculate the density of states for each energetically accessible electronic and vibrational levels of product CH_n^+.

Ion yield ratio (branching ratio) of photoproducts CH_n^+ measured for conductive and insulating SAMs can be reproduced for the site-selective σ*(O-CH₃) and non-selective σ*(C-C) excitations as direct and indirect components, and the ratio of its indirect components are plotted in Fig. 4 for molecular conductance (Ω^{-1}) in the literature [4-6]. Linear relation in the figure is qualitatively good, indicating that non-contact evaluation of molecular conductivity of organic molecules can be achievable by utilizing core-excitation dynamics measurements.
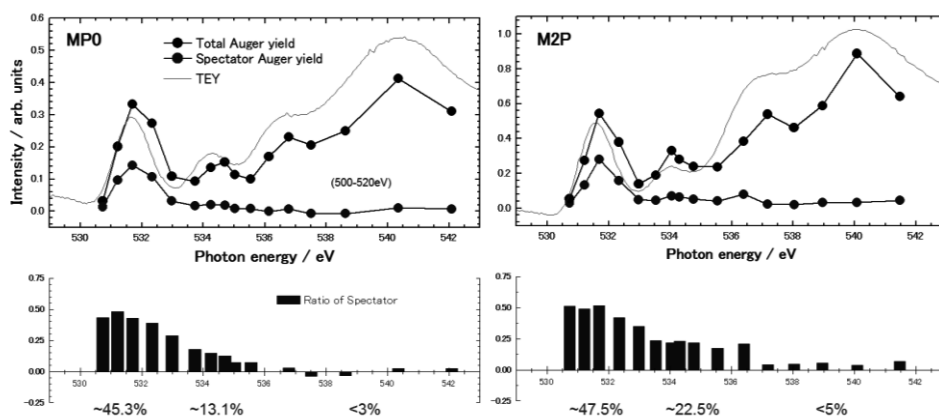

FIGURE 2. NEXAFS and Auger electron yield spectra measured for (a) MP0 and (b) M2P conductive SAMs.
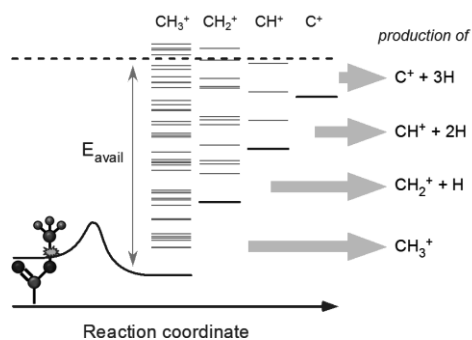

FIGURE 3. Schematic model of statistical consideration to reproduce branching ratio of energetic photodesorbing CH_3^+ ion.
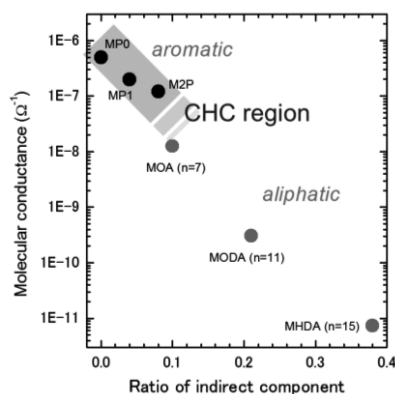
FIGURE 4. Plot of indirect component of selective CH_n^+ desorption vs. molecular conductance for conductive and insulating SAMs.

REFERENCES

1. S. Wada, H. Kizaki, Y. Matsumoto, R. Sumii and K. Tanaka, J. Phys.: Condens. Matter 18, S1629-S1653 (2006).
2. J. Schnadt, P. A. Bruhwiler, L. Patthey, J. N. O'Sea, S. Sodergren, M. Odelius, R. Ahuja, O. Karis, M. Bassler, P. Persson, H. Siegbahn, S. Lunell, and N. Martensson, Nature 418, 620-623 (2002).
3. A. Fohlische, P. Feulner, F. Hennies, A. Fink, D. Menzel, D. Sanchez-Portal, P.M. Echenique, and W. Wurth, Nature 436, 373-376 (2005).
4. D.M. Adams, L. Brus, C.E.D. Chidsey, S. Creager, X. Zhu et al., J. Phys. Chem. B 107, 6668-6697 (2003).
5. L. Venkataraman, J.E. Klare, C. Nuckolls, M.S. Hybertsen, and M.L. Steigerwald, Nature 442, 904-907 (2006).
6. P. Kao, S. Neppl, P. Feulner, D.L. Allara, and M. Zharnikov, J. Phys. Chem. C 114, 13766-13773 (2010).

Magnetic properties of Fe ultrathin films in h-BN/Fe/Ni(111) and Fe/h-BN/Ni(111)

Wataru Tadano[a], Masahiro Sawada[b], Hirofumi Namatame[b], and Masaki Taniguchi[b]

[a]*Department of Physical Science, Graduate School of Science, Hiroshima University, 1-3-1 Kagamiyama, Higashi-Hiroshima, 739-8526, Japan*
[b]*Hiroshima Synchrotron Radiation Center, Hiroshima University, 2-313 Kagamiyama, Higashi-Hiroshima, 739-0046, Japan*

Monolayer (ML) hexagonal boron nitride (h-BN) with graphene-like honeycomb structure attracts attention as a material for insulating barrier layers in tunnel magnetoresistance (TMR) device. Magnetism at interfaces between the h-BN layer and ferromagnetic metals is essential for design of the TMR devices. Ultrathin film of h-BN/Fe/Ni(111) is one of best samples to investigate the magnetic interfaces in atomic layer scale. So far, only phonon dispersion of lattice vibration in the h-BN/Fe/Ni(111) has been investigated [1]. No information has been revealed on magnetism in h-BN/Fe/Ni(111) system. In this study, we have investigated Fe-thickness dependence of magnetic state in Fe/h-BN/Ni(111) and h-BN/Fe/Ni(111) structures, by means of soft X-ray magnetic circular dichroism (XMCD).

High-quality h-BN can be grown on Ni(111) surface by cracking of vaporized borazine ($B_3N_3H_6$) [2]. As-grown samples of Fe/h-BN/Ni(111) are obtained by molecular beam evaporation of Fe. Post-annealing procedure promotes intercalation of Fe underneath the h-BN layer, leading to inert effect of the Fe film which is protected by h-BN as passivation layer [3]. We fabricated Fe/h-BN/Ni(111) and h-BN/Fe/Ni(111) films for the thickness dependence measurements of XMCD spectra, where the Fe ultrathin films had wedge-type structures. The XMCD experiments were performed just after the sample preparations *in-situ* at HiSOR-BL14 in Hiroshima Synchrotron Radiation Center (HSRC) [4, 5].

Figure 1(a) shows *M-H* curves for h-BN/3.2 ML-Fe/Ni(111) measured at room temperature, which is obtained from magnetic field dependence of the XMCD signal at Fe L_3 absorption edge. In the measurements, normal and grazing incidence geometry was applied to detect the out-of-plane and in-plane magnetization, respectively. In all the thickness range, in-plane magnetic anisotropy of the Fe film was clearly observed as well as shape magnetic anisotropy of the Ni substrate with in-plane easy axis. It has been revealed that spin magnetic moments of Fe and Ni are ferromagnetically coupled and saturated in relatively small external magnetic field. Figure 1(b) shows *M-H* curves for the case of 3.0 ML-Fe/h-BN/Ni(111) without intercalation. In the grazing incidence measurement, opposite magnetization direction in the Fe film is probed to the direction of external field and Ni spin in the substrate. This indicates antiferromagnetic coupling between Fe and Ni through the h-BN monolayer. The antiferromagnetic behavior is found in the normal incidence measurement as well, whose behavior is changed into ferromagnetic one above 4ML.

Figure 2 shows thickness dependence of XMCD spectra for h-BN/Fe/Ni(111) measured at Fe $L_{2,3}$ absorption edges. These spectra were measured at room temperature in normal incidence geometry with external magnetic field of 1.1 T. The XMCD spectra have been observed for saturated magnetization, whose spectral amplitudes are normalized by X-ray absorption spectral intensities. The saturated spin magnetic moment of Fe atomic site is clearly depending on the Fe layer thickness, and the maximum value is found around 3ML. The reduction of Fe spin in thicker layers implies transition from pseudomorphic fcc(111) structure to bcc(110) phase [6, 7].
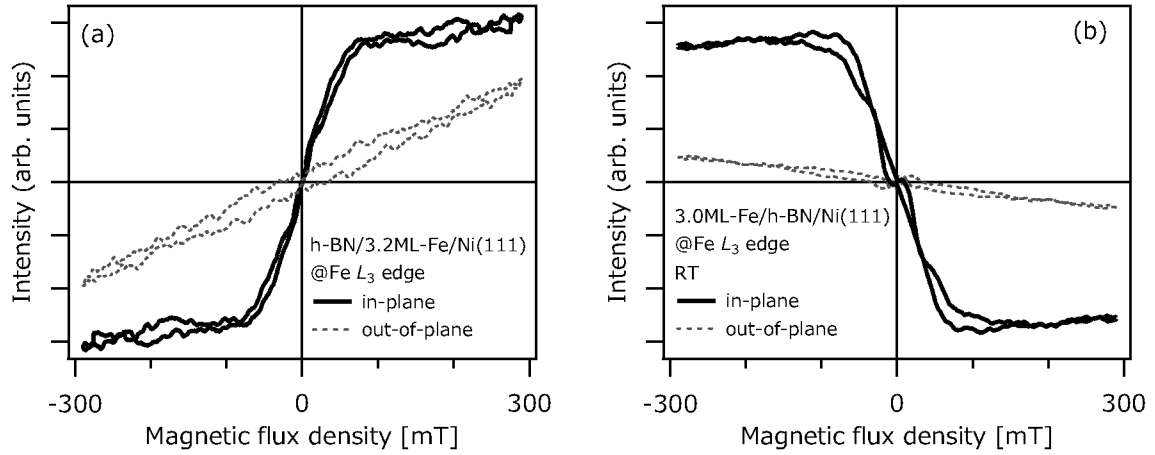
FIGURE 1. *M-H* curves for (a) h-BN/3.2 ML-Fe/Ni(111) and (b) 3.0 ML-Fe/h-BN/Ni(111) measured at Fe L_3 edge.
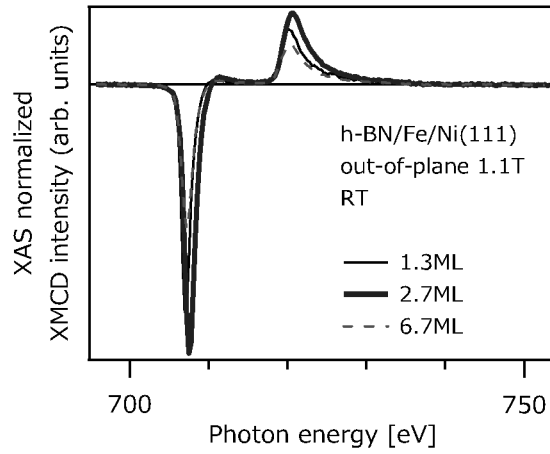

FIGURE 2. The XMCD spectra for h-BN/Fe/Ni(111) measured at Fe $L_{2,3}$ edges.

REFERENCES

1. T. Tanaka, A. Tajima, R. Koriizumi, C. Oshima, Y. Tsunoda, M. Seto, S. Kitao, T. Mitsui, J. Phys. Soc. Jpn. **74**, 1762 (2005).
2. C. Oshima and A. Nagashima, J. Phys.: Condens. Matter **9**, 1 (1997).
3. Yu. S. Dedkov, M. Fonin, U.Rüdigger, and C. Laubschat, Appl. Phys. Lett. **93**, 022509 (2008).
4. M. Sawada, K. Yaji, M. Nagira, A. Kimura, H. Namatame, M. Taniguchi, AIP Conf. Proc. **879**, 551 (2007).
5. M. Sawada, T. Ueno, T. Tagashira, H. Namatame, M. Taniguchi, AIP Conf. Proc. **1234**, 939 (2010).
6. G. C. Gazzadi, F. Bruno, R. Capelli, L. Pasquali, S. Nannarone, Phys. Rev. B 65, 205417 (2002).
7. B. An, L. Zhang, S. Fukuyama, K. Yokogawa, Phys. Rev. B **79**, 085406 (2009).

XMCD Study of Magnetic Proximity Effect in Co / $Y_3Fe_5O_{12}$ Heterostructures

V. V. Fedorov[a], A. M. Korovin[a], S. M. Suturin[a], M. Sawada[b] and N. S.Sokolov[a]

[a]*Ioffe Physical-Technical Institute, 26 Polytechnicheskaya str., St. Petersburg 194021, Russia*
[b]*Synchrotron Radiation Center, Hiroshima University, Kagamiyama, Higashi-Hiroshima, Japan*

The magnetic proximity effect [1,2] usually refers to the phenomena that take place in heterostructures with magnetically ordered layers, which allow the control of the magnetic properties of one of the magnetic layers due to the presence of the other one. As was demonstrated in ferromagnet / antiferromagnet systems [1,3], magnetic properties, such as magnetization reversal mechanism or even magnetic anisotropy of two different magnetic materials in contact can be significantly altered due to proximity effects. Thus proximity effects, such as interlayer coupling in heterostructures open a new way to tailor the magnetic properties of materials [4,5].

Yttrium Iron Garnet (YIG, $Y_3Fe_5O_{12}$) is the well-known ferrimagnet (T_c=560K) because of its unique properties. YIG has the narrowest ferromagnetic resonance (FMR) linewidth and the longest spin-wave relaxation time. Recently it has been predicted [6] that in case of nanometer thick films a substantial reduction of spin wave damping constant can be expected, that is of considerable interest for the magnonics: a new research area in spintronics and spin wave electronics [7]. To incorporate a YIG film in a device, magnetic biasing of YIG film is usually required; so presence of d.c. biasing magnetic field from is necessary, which is poorly compatible with modern planar technology [8]. In this work, we explore the possibility of magnetic biasing of ultrathin YIG films by proximity effect with ultrathin ferromagnetic layer, such as Co. It is well known [9] that FMR properties are extremely influenced by magnetic domain structure, which in turn can also be tailored by magnetic proximity effect.

YIG single crystal epitaxial films were grown on (111) gadolinium gallium garnet (GGG) substrates in layer-by-layer mode using laser molecular beam epitaxy (Laser-MBE by Surface GmbH) at Ioffe Institute. In our previous work [10] it have been shown that thinnest layers of YIG with precise control of stoichiometry and strain engineering can be obtained by Laser-MBE. (111) film orientation was chosen to compensate magnetocrystalline anisotropy. Film thickness was estimated from RHEED intensity oscillations during deposition and was about 10 nm. To study the interlayer coupling the X-Ray Magnetic Circular Dichroism (XMCD) technique - a unique magnetic probe with an element-specificity is used. The XMCD experiments were performed at HiSOR-BL14 beamline (Synchrotron Radiation Center, Hiroshima University).

X-Ray absorption spectra (XAS) were measured using total electron yield (TEY) technique. XMCD signal was obtained as a difference between the absorption of circularly-polarized light for a two opposite directions of the external magnetic field with maximum value of ±3 kOe, applied by an electrical magnet. The measurements were conducted at the room temperature (300K). Element selective magnetization curves M(H) were measured for as XMCD signal at Co and Fe absorption edges as a function of applied magnetic field. Thus XMCD study allowed us to separately probe the magnetization of ferromagnetic and ferrimagnetic layers.

UHV-connected preparation and analytical XMCD-chambers enabled the experiments *in-situ*: ferromagnetic layers of Co with coverage ranging between 2 and 6 nm were grown from an e-beam bombardment cell in UHV conditions at 100 °C on YIG/GGG structures already grown by Laser-MBE. RHEED patterns taken during the growth showed that the Co film is polycrystalline. AFM showed that 6 nm thick Co layer is formed by interconnected islands with diameters smaller than 10 nm (limited by the AFM resolution). The height variation is under 0.6 nm with a surface rms-roughness of about 0.2 nm.

According to the MOKE (Magnetic-Optic Kerr Effect) measurements the magnetization of thin (10 nm) garnet films lies in the plane and shows in-plane uniaxial magnetic anisotropy. Maximum value of the coercive field is along the easy axis and is about 0.2 Oe, but after the deposition of 4 nm thick Co layer values of coercive field increased by two orders of magnitude. Although the Co layer is polycrystalline, significant uniaxial in-plane

anisotropy can be seen; furthermore, the easy axis direction coincides with the YIG easy axis before Co deposition.

XAS and XMCD experiments performed *in-situ* allows us to separately probe the magnetization of both layers of heterostructure and avoid any air oxidation of cobalt layer. Line shape of the XAS and XMCD spectra is strongly dependent on the crystal-field splitting under the specific local coordination of atom. Magnetic structure of YIG consists of two magnetic sublattices with different crystal-field value and symmetry. For this reason, in XAS and XMCD spectra, as it was shown for γ-Fe_2O_3 [11], one can see a superposition of spectra for Fe^{3+} ions both in tetrahedral and octahedral sites. It can be seen by comparing the experimental XMCD data for two different YIG films - with and without 6 nm thick Co overlayer grown on top, that XMCD lineshape at Fe L-edge is varied after Co deposition (see Fig. 1). This can be attributed to distortion of Fe sublattices due to exchange coupling of iron sublattices with Co magnetic moments or other hybridization effects.
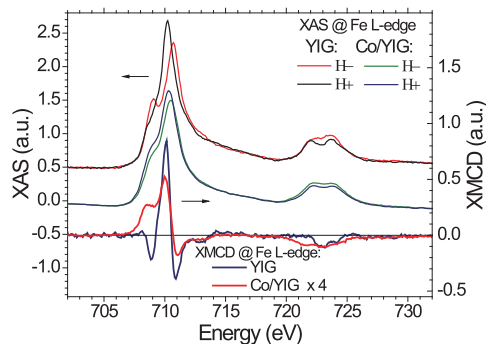

FIGURE 1. Normalized XAS (shifted vertically for clarity) and XMCD spectra at the $L_{2,3}$ edges taken in the magnetic field of ± 0.3 T
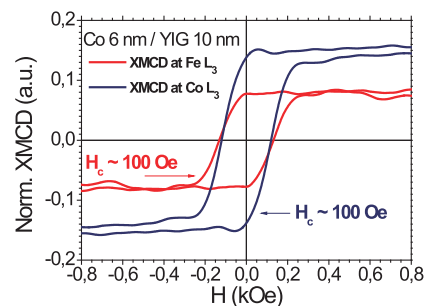
FIGURE 2. Element-specific hysteresis loops for 6 nm Co / 10 nm YIG / GGG(111) heterostructure.

The element specific magnetization curves for both ferro- and ferrimagnetic layer of heterostructure measured at L_3 absorption edge of Fe and Co are presented in Fig. 2. It can be seen that the YIG magnetization curve exhibits the same shape and width as those of Co, one can conclude that magnetic moments of ferro- and ferrimagnetic layers are coupled parallel to each other and their magnetization reversal occurs simultaneously. The value of the coercive field (H_C) for both layers exceeds the H_C for bare YIG film before Co deposition by two orders of magnitude.

In conclusion, it was shown in this work that magnetic properties of 10 nm thick YIG epitaxial film drastically changed due to interlayer exchange coupling with polycrystalline Co overlayer grown on top of the ferrite film. YIG layer coercivity is increased by more than two orders in magnitude (120 Oe vs. 0.2 Oe), while whole structure demonstrate uniaxial in-plane magnetic anisotropy inherited from the garnet underlayer. Further ferromagnetic resonance measurements will be performed to estimate the value of magnetic anisotropy in the heterostructure. Thus heterostructures built on exchange coupled ferromagnetic and ferrimagnetic layers can act as a new functional material with tailored magnetic properties determined by interlayer exchange coupling.

REFERENCES

1. P. K. Manna and S. M. Yusuf, *Phys. Rep.* **535**, 61–99 (2014).
2. I. P. Krug, Magnetic Proximity Effects in Highly-ordered Transition Metal Oxide Heterosystems - A Study by Soft-X-Ray Photoemission Microscopy. Forschungszentrum Julich, 2008.
3. F. Radu, H. Zabel, Magnetic Heterostructures / ed. H. Zabel, S. D. Bader, Springer, 2008. Vol. 227. P. 97–184.
4. I. Vobornik et al, *Nano Lett.* **11,** 4079–4082 (2011).
5. M. Lang et al, *Nano Lett.* **14,** 3459–3465 (2014).
6. L. V. Lutsev, *Phys. Rev.* **B 85**, 214413 (2012).
7. S. A. Nikitov et al, *Physics-Uspekhi* **58**, 1002–1028 (2015).
8. D. D. Stancil, *Microw. Opt. Technol. Lett.* **2**, 81–85 (1989).
9. S. A. Manuilov, A. M. Grishin, M. Munakata, *J. Appl. Phys.* **109**, 083926 (2011).
10. S. Brice-Profeta et al, Phys. Scr. **T 115**. 626–628 (2005).
11. N. S. Sokolov et al, *J. Appl. Phys.* **119**, 023903 (2016).

XAS and XMCD study of Pd(100) and Fe/Pd(100) ultrathin films

S. Sakuragi[1], M. Sawada[2], S. Nakahara[1], and T. Sato[1]

[1] Department of Applied Physics and Physico-Informatics, Keio University, Japan
[2] Hiroshima Synchrotron Radiation Center, Hiroshima University, Japan

Keywords: Pd, ultrathin film, quantum-well states

Pd(100) ultrathin film on $SrTiO_3$ substrate shows ferromagnetism depending on film thickness with a period of ~6 monolayers [1]. This is explained in terms of the increase of $D(\varepsilon_F)$, which originates from quantum-well states in Stoner's criterion $ID(\varepsilon_F) > 1$ for ferromagnetism in metal, where I is the exchange integral, and $D(\varepsilon_F)$ is the density of states at Fermi energy. Theoretical calculation indicated that the modulation of quantum-well states using an electric field induced the nonmagnetic-ferromagnetic switching in Pd(100) ultrathin films [2, 3]. This will contribute to the development of the novel application of giant magnetoresistance by incorporated to magnetic multilayer system. In this study, we performed the X-ray absorption spectroscopy (XAS) and X-ray magnetic circular dichroism (XMCD) measurement of Pd(100) ultrathin films and Fe covered Pd(100) ultrathin films to investigate the relationship between the magnetic property and electronic states of magnetic multilayer system containing quantum-well of Pd.

We performed in-situ XAS and XMCD measurement with a fixed polarization direction of the circularly polarized light using total electron yield method at room temperature using HiSOR beamline BL-14. To prevent charged up, Cu(100) single crystal was used as a substrate. Cu(100) was prepared by 1 keV Ar^+ sputtering and subsequent annealing at ~873 K in the ultra-high vacuum chamber, and Pd grew epitaxially on this substrate. In order to perform the thickness dependence of XAS and XMCD, a wedge-shaped Pd film was prepared. After the XAS and XMCD measurement of Pd/Cu(100) system, ~1 MLs Fe was deposited on this sample, and subsequent measurement of XAS and XMCD of Fe/Pd/Cu(100) system were performed. Fig. 1 shows low-energy electron scattering (LEED) images of annealed Cu(100), Pd/Cu(100), and Fe/Pd/Cu(100). The sharp spots were observed in Cu(100) surface, and the spots changed to the streak patterns by the deposition of Pd. This indicates that Pd grew epitaxially on Cu(100) surface but Pd had a lot of domains because of the island grows. On the other hand, four-fold patterns of LEED were observed after the deposition of Fe on Pd(100). This indicates that the fcc Fe grew on Pd(100) surfaces.

Figure 2 (a) shows the Pd thickness dependence of the peak value of XAS obtained from the Pd M_3 edge in Pd/Cu(100) and Fe/Pd/Cu(100) systems. The oscillatory manners of the XAS intensity dependent on film thickness with the period of ~3 monolayers were observed in both systems. This period of oscillation is
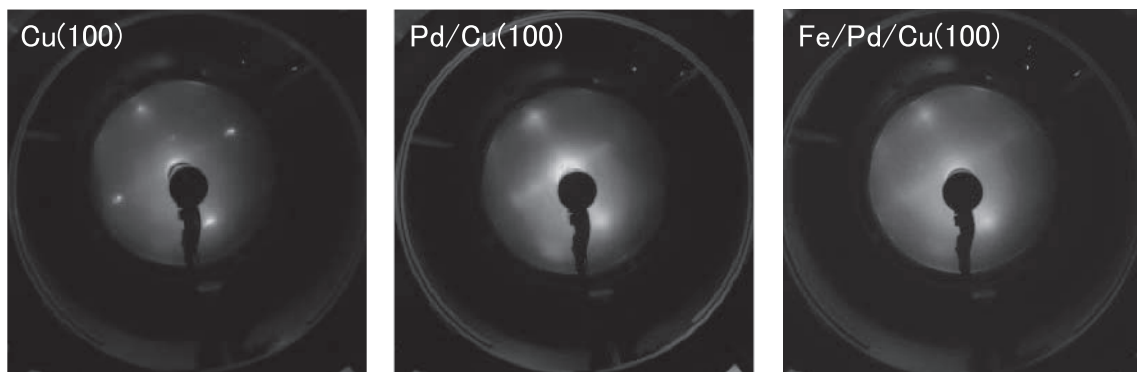

FIGURE 1. LEED images of Cu(100), Pd/Cu(100), and Fe/Pd/Cu(100). The sharp spots were observed in Cu(100), and these spots changed to streaky spots by the deposition of Pd. This indicates Pd grows epitaxially, although Pd has a lot of grains. Fe/Pd/Cu(100) shows the four-fold spots, and it was indicated that fcc Fe was grown on Pd/Cu(100).

different from that of the appearance of ferromagnetism in the Pd/SrTiO$_3$ system, which is consistent with the theoretical prediction based on QWs [4]. This indicates that our present samples have a different quantum confinement with QWs. Our present samples had a lot of grains of Pd island (Fig. 1), thus the dimension of quantum confinement is different from that of the Pd/SrTiO$_3$ system. To explain the mechanism of this phenomenon clearly, analysis of the surface morphology of our present sample is necessary.

The thickness at which the peak appears in Pd XAS of Fe/Pd/Cu(100) was slightly different from that in Pd/Cu(100) system. This is explained by the change in the scattering phase shift of quantum confinement [1, 5]. By the deposition of Fe on Pd, the potential energy at the interface of Pd changed, and the modulation of phase shift of the electron scattering occurred at the interface. This affected the change in electronic states of the confined electrons, and shifted the peak thickness in the XAS intensity.

We attempted to observe XMCD of Pd M edges in Pd/Cu(100) and Fe/Pd/Cu(100), although we could not observe clear signal of XMCD because of the small absorbed intensity of Pd M edges. On the other hand, we observed clear XMCD signal of Fe L edges in Fe/Pd/Cu(100) system. Fig. 2 (b) shows the Pd thickness dependence of the peak amplitude of Fe L_3 edge XMCD in Fe/Pd/Cu(100) system. The intensity of XMCD of Fe is subjected to modulation dependent on the film thickness of Pd layer to show the positive correlation between the changes in the intensity of Fe XMCD and Pd XAS. This indicates that the value of magnetic moment of Fe overlayer are modulated by the quantum confinement of Pd underlayer because the intensity of XMCD corresponds to the value of magnetic moment.

The strength of white line of XAS is proportional to the number of unoccupied states. Therefore, Fig. 2(a) indicates that the change in the film thickness of Pd induces a change in the number of unoccupied $4d$ states of Pd. This can affect to the electron density of Fe/Pd interface [6, 7]. Thus, the magnetic moment of Fe/Pd interface should change [8], in a manner similar to the strength of Fe XMCD. The detail will be clarified based on the detailed XMCD measurement of this system.

In conclusion, we performed XAS and XMCD measurements of the films of Pd/Cu(100) and Fe/Pd/Cu(100), and clarified that the magnetic property of Fe overlayer was modulated by the quantum confinement of Pd underlayer. Hence, we have plan to perform detailed XMCD measurement of these systems, and clarify the influence of quantum confinement to the magnetic properties of magnetic multilayer systems.
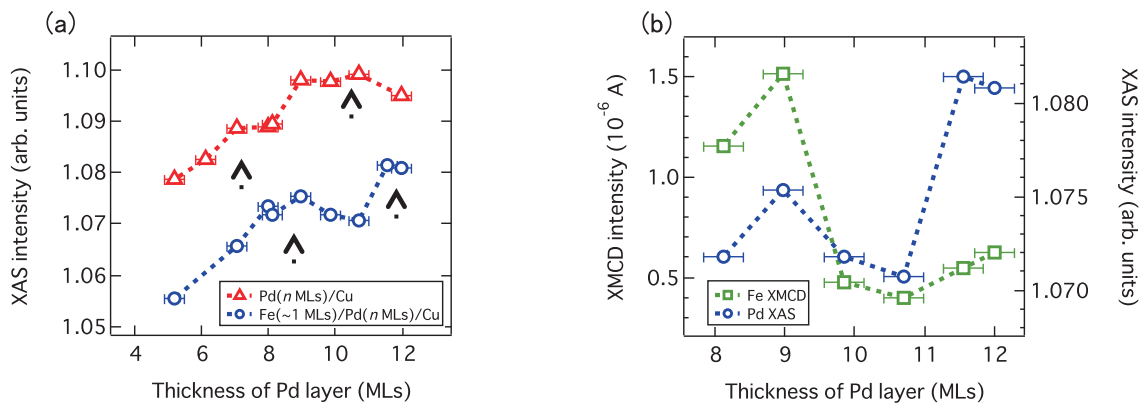

FIGURE 2. (a) Thickness dependence of XAS of Pd M_3 edge in Pd/Cu and Fe/Pd/Cu(100). The oscillatory manners were observed. (b) Thickness dependence of XMCD of Fe L_3 edge and XAS of Pd M_3 edge. There was the positive correlation between the XMCD of Fe and XAS of Pd.

REFERENCES

1. S. Sakuragi, T. Sakai, S. Urata, S. Aihara, A. Shinto, H. Kageshima, M. Sawada, H. Namatame, M. Taniguchi, and T. Sato, Phys. Rev. B **90**, 054411 (2014).
2. Y. Sun, J. D. Burton, and E. Y. Tsymbal, Phys. Rev. B **81**, 064413 (2010).
3. S. Aihara, H. Kageshima, T. Sakai, and T. Sato, J. Appl. Phys. **112**, 073910 (2012).
4. S. C. Hong, J. I. Lee, and R. Wu, Phys. Rev. B **75**, 172402 (2007).
5. T.-C. Chiang, Surf. Sci. Rep. **39**, 181 (2000).
6. W. Weber, A. Bischof, R. Allenspach, Ch. Würsch, C. H. Back, and D. Pescia, Phys. Rev. Lett. **76**, 3424 (1996).
7. S. Manna, P. L. Gastelois, M. Dabrowski, P. Kuswik, M. Cina, M. Przybylski, and J. Kirschner, Phys. Rev. B **87**, 134401 (2013).
8. H. Shima K. Oikawa, A. Fujita, K. Fukamichi, K. Ishida, and A. Sakuma, Phys. Rev. B **70**, 224408(2004).

Temperature evolution of the density of states near the Fermi level of $Ce_3Pd_{20}Si_6$ and $Ce_3Pd_{20}Ge_6$

H. Yamaoka[a], E. F. Schwier[b], Y. Yamamoto[c], N. Tsujii[d],
H. Kitazawa[d], H. Iwasawa[b], K. Shimada[b], and J. Mizuki[c]

[a]*RIKEN SPring-8 Center, Sayo, Hyogo 679-5148, Japan*
[b]*Hiroshima Synchrotron Radiation Center, Hiroshima University, Higashi-Hiroshima, Hiroshima 739-0046, Japan*
[c]*Graduate School of Science and Technology, Kwansei Gakuin University, Sanda, Hyogo 669-1337, Japan*
[d]*Quantum Beam Center, National Institute for Materials Science, 1-2-1 Sengen, Tsukuba 305-0047, Japan*

The caged compound $Ce_3Pd_{20}Si_6$ is known to be one of the heaviest electron Kondo systems with a low-temperature electronic specific heat coefficient of $\gamma = 8$ J/molK^2[1]. Such large γ values are normally attributed to strong electron correlations and a large density of states (DOS) at the Fermi level (E_F). On the other hand, the isostructural germanide compound $Ce_3Pd_{20}Ge_6$ is a heavy-electron system[2]. The electronic specific heat coefficient of $\gamma \sim 0.7$ J/molK^2 is smaller by one order of magnitude compared to that of $Ce_3Pd_{20}Si_6$ and the effective moment is nearly equal to that of free trivalent Ce^{3+}.

The electronic structure of $Ce_3Pd_{20}X_6$ (X = Si, Ge) has been studied using detailed density functional theory (DFT) calculations and high-resolution photoelectron spectroscopy (PES) measurements[3]. The orbital decomposition of the electronic structure by DFT calculations indicated that the Ce atoms in the (8c) site surrounded by 16 Pd atoms had a tendency to be magnetic. Ce atoms in the (4a) site surrounded by 12 Pd and 6 X atoms, on the other hand, were more localized and paramagnetic. The $4d$-$4f$ resonance PES measurements of the polycrystalline $Ce_3Pd_{20}X_6$ (X = Si, Ge) have clearly indicated the Ce $4f$ contribution in the valence band in these compounds. The spectral weight of Ce $4f^0$ was stronger than that of Ce $4f^1$, indicating the localized nature of Ce $4f$ electrons. Near the Fermi level, the Ce $4f^1$ weight of $Ce_3Pd_{20}Si_6$ was stronger than that of $Ce_3Pd_{20}Ge_6$, suggesting stronger c-f hybridization in the former.

Here we report on our Laser PES study of single crystalline $Ce_3Pd_{20}Si_6$ and $Ce_3Pd_{20}Ge_6$. We measured the temperature dependent evolution of the DOS near E_F with high-resolution Laser PES. In the previous study with using synchrotron radiation at Ce $4d$-$4f$ resonance of 122 eV the valence band spectra did not show temperature dependence clearly, where the total energy resolution (ΔE) was 50 meV at 10 K. On the other hand, in the Laser PES experiment, the contribution to the resolution broadening from the Laser and the analyzer were set to 1 meV.

During the temperature dependent measurements, the laser intensity was slightly fluctuating. To account for this effect, each spectrum was normalized on the DOS at binding energies higher than 80 meV. Then the total spectral weight in a window of 40 meV around E_F was integrated and is plotted in Fig. 1. The results indicate that $Ce_3Pd_{20}Si_6$ compound has a transition between 17-27 K and the $Ce_3Pd_{20}Ge_6$ compound from 21-30 K. If we assume that the change in DOS is related to the Kondo regime we may speculate that the upper temperature onset is related to the Kondo temperatures of the systems.

The temperature dependence of the resistivity of $Ce_3Pd_{20}Si_6$ and $Ce_3Pd_{20}Ge_6$ showed T^2 dependence below 0.3 K (Ref. 1) and 0.7 K (Ref. 2), respectively, indicating the Kondo-lattice formation in these temperature ranges. Normally the Kondo temperature is one order magnitude larger than the temperature of the Kondo lattice formation and thus the Kondo temperature of these two systems may be on the order of a few to 10 K. The transition temperatures from the PES results roughly agree with the order of the Kondo temperature and the Kondo temperature of both compounds are the same order. This result agrees with the previous PES result in that the sp-state-derived DOS at E_F does not show a significant difference to explain the large difference of γ between two compounds while the Ce $4f^1$ weight of $Ce_3Pd_{20}Si_6$ was stronger than that of $Ce_3Pd_{20}Ge_6$ slightly as described above [3]. Our results suggest an importance of the electron correlations.

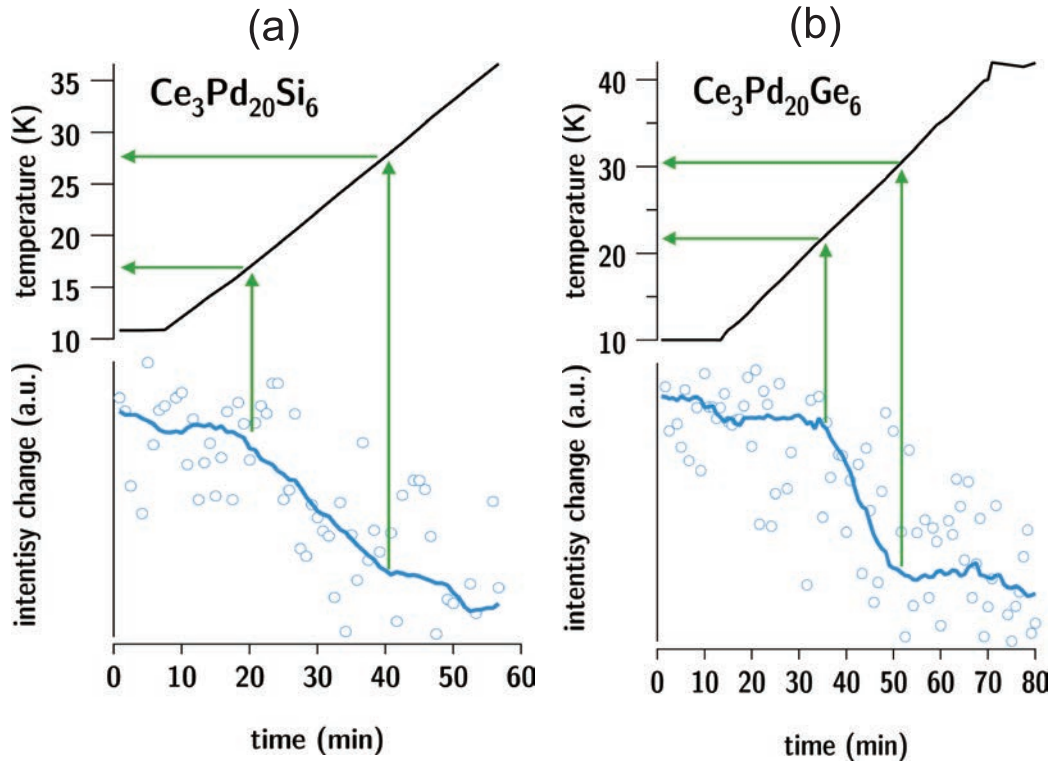**FIGURE 1.** Temperature evolution of the density of states near the Fermi edge of (a) $Ce_3Pd_{20}Si_6$ and (b) $Ce_3Pd_{20}Ge_6$.

References

1. N. Takeda, J. Kitagawa, and M. Ishikawa, J. Phys. Soc. Jpn. **64**, 387 (1995).
2. J. Kitagawa, N. Takeda, and M. Ishikawa, Phys. Rev. B **53**, 5101 (1996).
3. H. Yamaoka, E. F. Schwier, M. Arita, K. Shimada, N. Tsujii, I. Jarrige, J. Jiang, H. Hayashi, H. Iwasawa, H. Namatame, M. Taniguchi, and H. Kitazawa, Phys. Rev. B **91**, 115139 (2015).

Laser μ Angle-Resolved Photoelectron Spectroscopy on CeT_2Al$_{10}$ (T = Ru, Os)

Kensei Terashima[a], Takanobu Nagayama[b], Hideaki Iwasawa[c], Eike F. Schwier[c], Jo Kawabata[d], Yoshihiro Yamada[d], Toshiro Takabatake[d], Yuji Muraoka[a,b], and Takayoshi Yokoya[a,b]

[a]*Research Institute for Interdisciplinary Science, Okayama University*
[b]*Graduate School of Natural Science and Technology, Okayama University*
[c]*Hiroshima Synchrotron Radiation Center, Hiroshima University*
[d]*Graduate School of Advanced Sciences of Matter, Hiroshima University*

Keywords: μ-ARPES, 1-2-10 system

CeT_2Al$_{10}$ (T = Ru, Os) are Kondo semiconductors that exhibit antiferromagnetic order as high as $T \sim 30$ K [1]. This transition temperature is much higher than that of expected value from de Gennes scaling, thus it cannot be understood in the framework of so-called RKKY interactions. Although the mechanism for this antiferromagnetic ordering has not been clarified yet, it has been discussed that the magnetic order is closely related with electronic states in this series of compound. Namely, angle-integrated photoelectron spectroscopy [2] reported that an energy gap is formed in the vicinity of Fermi level below the phase transition temperature. In addition, optical conductivity measurement [3] showed that the energy gap is highly anisotropic, suggesting that the magnetic order can be related with the formation of a density wave. However, theoretical calculations does not predict Fermi surface whose shape shows good nesting condition [4]. Therefore, experimental observation of the band dispersion has been highly anticipated. CeT_2Al$_{10}$ does not tend to give a flat cleaved surface, and no successful angle-resolved photoelectron spectroscopy (ARPES) have been reported so far.

In this study, we took advantage of Laser μ ARPES which has been newly built in off-line section. Thanks to its extremely small spot size, laser μ ARPES could shed light on small flat area obtained by cleaving. We performed the experiment at 40 K, slightly above the magnetic transition temperature. Figure 1 shows ARPES intensity plot of CeOs$_2$Al$_{10}$ taken along b-axis where optical conductivity [3] reported an energy gap. We have observed a signature of band dispersion in the vicinity of Fermi level, although angle-integrated background is still too high to discuss the precise positions of bands. Further trials with multiple cleaving of samples should be made in order to find a suitable flat part of the sample surface and determine the topology of Fermi surface.
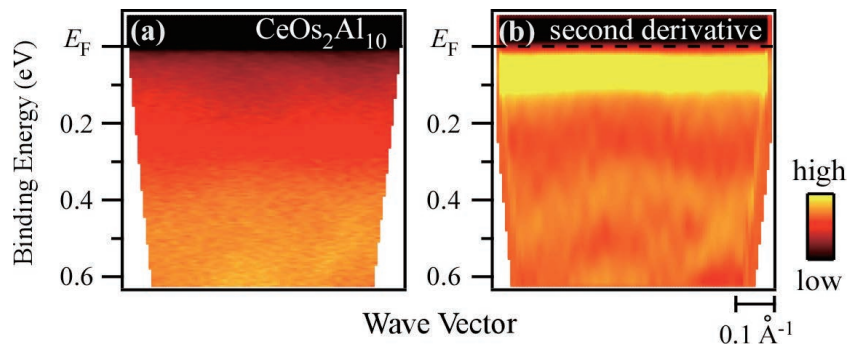

FIGURE 1. (a) μ-ARPES intensity plot of CeOs$_2$Al$_{10}$ taken along b-axis at T = 40 K. (b) Second derivative of (a) with respect to energy with the opposite color scale.

REFERENCES

1. T. Nishioka *et al.*, *J. Phys. Soc. Jpn.*, **78**, 123705 (2009). 2. T. Ishiga *et al.*, J. Phys. Soc. Jpn., **83**, 094717 (2014).
3. S. Kimura *et al.*, Phys. Rev. Lett. **106**, 056404 (2011). 4. M. Samsel-Czekala *et al.*, J. Alloy Compd. **554**, 438 (2013).